KfK 3861
Dezember 1984

Two-Phase Flow Through Small Branches in a Horizontal Pipe with Stratified Flow

C. Smoglie
Institut für Reaktorbauelemente

Kernforschungszentrum Karlsruhe

KERNFORSCHUNGSZENTRUM KARLSRUHE
Institut für Reaktorbauelemente

KfK 3861

Two-Phase Flow Through Small Branches in a Horizontal Pipe with Stratified Flow

Cecilia Smoglie

This report is a translation of a dissertation presented to the Faculty of Mechanical Engineering at the University of Karlsruhe
December 1984

Kernforschungszentrum Karlsruhe GmbH, Karlsruhe

Als Manuskript vervielfältigt
Für diesen Bericht behalten wir uns alle Rechte vor

Kernforschungszentrum Karlsruhe GmbH
ISSN 0303-4003

SUMMARY

In the field of nuclear reactor safety the occurrence of a small break in a horizontal coolant pipe is of great importance. This report presents the description and results of experiments designed to determine the mass flow rate and quality through a small break at the bottom, the top or the side of a main pipe with stratified gas-liquid flow. The break was simulated by circular branches with diameters of 6, 8, 12 or 20 mm, perpendicular to the main pipe with a diameter of 206 mm. The experiments were performed with air-water flows at ambient temperature and a maximal pressure of 0.5 MPa.

If the interface level is far below (above) the branch, only single-phase gas (liquid) flow enters the branch. For smaller distances the interface is locally deformed because of the pressure decrease due to the fluid acceleration near the branch inlet (Bernoulli effect) and liquid (gas) can be entrained.

This report contains photographs illustrating the flow phenomena as well as a general correlation to determine the beginning of entrainment. Results are presented on the branch mass flow rate and quality as a function of a normalized distance between the interface and the branch inlet.

A model was developed which enables to predict the branch quality and mass flux. Results from air-water flow through horizontal branches, were extrapolated for steam water flow at high pressure with critical branch mass flux.

Zweiphasenströmungen durch kleine Abzweige in einem horizontalen Rohr mit geschichteter Gas-Flüssigkeits-Strömung

Zusammenfassung

Im Bereich der Reaktorsicherheit ist der Kühlmittelverlustunfall, verursacht durch kleine Lecks in der horizontalen Hauptkühlmittelleitung, von großer Bedeutung. Dieser Bericht enthält die Beschreibung und die Ergebnisse von Experimenten zur Bestimmung des Massenstroms und des Dampfgehalts durch ein kleines Leck, das sich oben, unten oder an der Seite einer waagerechten Hauptkühlmittelleitung befindet, in der eine geschichtete Gas-Flüssigkeitsströmung vorhanden ist. Das Leck wurde durch kreisförmige Rohrabzweige mit Durchmessern von 6, 8, 12 oder 20 mm simuliert, die senkrecht zur Achse des Hauptrohres angebracht wurden. Die Experimente wurden mit Luft-Wasser Strömung bei Umgebungstemperatur und einem maximalen Druck von 0,5 MPa durchgeführt.

Wenn sich der Wasserspiegel weit unterhalb (oberhalb) des Rohrabzweigs befindet, gelangt nur Gas (Flüssigkeit) in den Abzweig. Bei kleineren Abständen zwischen Abzweig und Wasserspiegel wird die Wasseroberfläche lokal verformt und Flüssigkeit (Gas) kann mitgerissen werden. Die Verformung wird durch den Druckabfall bewirkt, der durch die starke Beschleunigung des Fluids in der Nähe des Abzweigs verursacht wird (Bernoulli Effekt).

Dieser Bericht enthält Fotos, die die Strömungsphänomene veranschaulichen, sowie eine allgemein gültige Korrelation, um den Beginn des Mitrisses zu bestimmen. Außerdem werden experimentelle Ergebnisse über Massenstromdichte und Dampfgehalt im Abzweig als Funktion eines normalisierten Abstandes gezeigt und die Abhängigkeit dieser Größen in empirischen Beziehungen beschrieben. Die Ergebnisse für horizontale Abzweige wurden übertragen auf Dampf-Wasser-Strömungen bei hohen Drücken und kritischem Massenstrom im Abzweig.

Contents

		Page
	Nomenclature	3
1	Introduction	7
2	Experimental Setup	11
3	Description of the Experiments	17
3.1	General Characteristics	17
3.1.1	Experimental Method	17
3.1.2	Measurements Accuracy	18
3.2	Experiments with Downward Branches	19
3.3	Experiments with Upward Branches	20
3.4	Experiments with Horizontal Branches	21
4	Flow Phenomena	22
4.1	Downward Branch	22
4.2	Upward Branch	24
4.3	Horizontal Branch	32
4.4	Transition from Stratified to Slug Flow	34
5	Beginning of Gas and Liquid Entrainment	39
5.1	Dimensional Analysis	39
5.2	A General Correlation for the Beginning of Entrainment	41
5.3	Theoretical Considerations for the Beginning of Entrainment in Upward Branches	42
5.3.1	Flow Field Generated by the Break	42
5.3.2	Determination of the Beginning of Entrainment	44
5.3.3	Influence of Superimposed Velocities	46
5.4	Results	48
6	Branch Quality and Mass Flux	60
6.1	Single Phase Flow	60
6.2	Two Phase Flow	64
6.2.1	Generalized Representation of Data	64
6.2.2	Experimental Results	64

		Page
6.2.2.1	Downward Branch	64
6.2.2.2	Upward Branch	66
6.2.2.3	Horizontal Branch	67
6.2.3	Correlations for the Branch Quality	71
6.2.3.1	Horizontal Branch	71
6.2.3.2	Downward Branch	75
6.2.3.3	Upward Branch	75
6.2.4	Correlations for the Branch Mass Flux	79
7	Critical Branch Mass Flux	86
7.1	The Homogeneous Equilibrium Model (HEM)	86
7.2	Quality and Critical Mass Flux in Horizontal Branches	88
7.3	Applications of the Model	88
7.4	Comparison with other Models	90
8	Summary	94
9	Literature	97
10	Appendixes	101
	A1 Method Used to Calculate Propagated Errors	101
	A2 Theoretical Research on the Flow of Non-homogeneous Fluids (from A. Craya /12/)	105
	A3 The Homogeneous Equilibrium Model (HEM) (from Moody /35/)	107
	A4 RELAP 5 Model for Horizontal Branch Quality (from Ransom et al. /39/)	109
	A5 Tables of Experimental Data	111

Nomenclature

A	flow area
c	calibration coefficient for orifices; sonic velocity
c_a	coefficient for air density
C, C_1	correction factors
d	diameter of the branch
D	diameter of the main pipe
f	friction coefficient
F_g	gravitational force
F_P	pressure force
g	acceleration of gravity
G	mass flux
h	distance from the branch entrance (branch axis) to the interface; specific enthalpy
h_g	gap of gas above the liquid
h_1	liquid level measured from the bottom of the main pipe
Δh	height of locally raised liquid above the horizontal interface
Δh_1	increment of liquid level
K	constant
K_c	contraction coefficient
l	length
M	measured magnitude
ΔM	absolute error in M
P	static pressure
$P_{31...35}$	static pressure at the positions 1,...,5 in the branch flow
P_B	static pressure at B
P_C	static pressure at C
ΔP	static pressure difference
ΔP_o	pressure drop at the orifices
ΔP_{1-3}	difference between P_1 and the static pressure in the branch
$\Delta P_{1-31...34}$	difference between P_1 and $P_{31...34}$
ΔP_{h1}	hydrostatic pressure difference between the interface and the bottom of the main pipe
q	volume flow through a sink
r	cylindrical coordinate
s	specific entropy
Δt	time interval

T	absolute temperature
u	radial component of the fluid velocity in the sink flow; phase velocity at the entrance of horizontal branches
$\vec{U}$	velocity of a uniform flow superposed to a sink flow
v	phase velocity; specific volume
v_{gL}	limit gas velocity defined in the RELAP 5 code
v_{sg}	superficial velocity of gas
v_{sl}	superficial velocity of liquid
$\vec{V}$	velocity vector in the flow field generated by a punctual sink
W	mass flow rate
x	quality
x_o	quality in the horizontal branch for h=0

Greek Symbols

α	angle between branch and vortex axis; void fraction
γ	isentropic coefficient for gases
δ	relative error
ε	expansion coefficient for gases
ζ	single phase flow coefficient
λ	wavelength
ρ	fluid density
ρ_b	density of the continuous phase at beginning of entrainment
$\Delta\rho$	difference between fluid densities
σ	standard deviation
ϕ	velocity potential

Subscripts

o	upstream of an orifice; stagnation value
1	upstream of the branch in the main pipe
2	downstream of the branch in the main pipe
3	in the branch
acc	acceleration
b	at beginning of entrainment
crit	critical
g	gas
ge	gas entrainment

H	homogeneous model
irrev	irreversible
l	liquid
le	liquid entrainment
lg	value for gas minus value for liquid
m	mixture
pr	predicted
rev	reversible
sat	saturation

Abbreviations

b.e.	beginning of entrainment
b.g.e.	beginning of gas entrainment
b.l.e.	beginning of liquid entrainment
g.e.	gas entrainment
l.e.	liquid entrainment

1. Introduction

The knowledge of two-phase flow in pipe junctions is in general very limited although there are many technical applications. This is due to the complex influence of the phase and velocity distributions and geometrical parameters on the mass and quality redistribution.

Several articles were published in which methods are attempted to determine how two-phase flows split in branching conduits:
Walley and Azzopardi /1/ and Henry /2/ investigated the case of air-water annular flow in horizontal or vertical T-junctions. Honan and Lahey /3/ and Zetzmann /4/ performed air-water experiments with different flow regimes in vertical pipes with branches at different angles. Saba and Lahey /5/ performed air-water experiments with the same test section as used in /3/ but a horizontal main pipe. Reimann et al. /6, 7/ and Seeger /8/ made experiments with different air-water and steam-water flow regimes to investigate the phase redistribution in horizontal T-junctions with different branch orientations. In the articles referred to above no stratified flow was investigated and the diameter ratio at the T-junction was always $\geq$ 0.2.

The special case of branches with a much smaller diameter than the diameter of the horizontal main pipe in which stratified flow prevails will be discussed in the following paragraphs. This situation is of interest in nuclear reactor safety with regard to Loss of Coolant Accidents (LOCAs) caused by small breaks. Here the break mass and enthalpy fluxes determine the behavior of such accidents; these quantities are strongly dependent on the position of the break. If it is located above the horizontal interface, either only vapor will flow out or also liquid will be entrained due to the pressure drop produced by vapor acceleration in the vicinity of the break (hereinafter called the Bernoulli effect). Similarly, with a break located below the interface, vapor may reach the break because of vortex formation or may be pulled-through in a vortex-free flow.

In connection with this problem, liquid removal from large reservoirs through downward, upward or sideward orientated outlets was previously investigated. However, the publications on this subject concentrate on the beginning of entrainment and give no results for the amount of entrainment when the pressure difference through the break is further enlarged or the distance between

break and interface level is further decreased.

Dagget and Keulegan /9/, for instance, presented data and correlations for predicting incipient vapor entrainment due to a vortex reaching the drain at the bottom of a vessel. The flow entered the test section horizontally, however, a set of vanes at specific angles was used to provide the desired circulation. Lubin and Hurwitz /10/ studied the formation of a dip on the surface of an initially stationary liquid draining through a circular orifice at the bottom of a cylindrical tank. Rouse et al. /11/ investigated the onset of a water spout formed below the intake of a vertical pipe at a certain distance above a horizontal interface between two fluids of different densities. Craya /12/ derived analytically and Gariel /13/ verified experimentally incipient liquid entrainment through side orifices in case of two-layer systems with a horizontal intake above the interface between two incompressible fluids.

The results from these publications were discussed by Zuber /14/ who pointed out that they do not correspond to nuclear reactor conditions. Fig. 1 (from /14/) illustrates the flow mechanisms of interest in nuclear reactors. These arrangements differ significantly from the situations mentioned above mainly due to:

- a flow geometry without rotational symmetry
- the existence of a remaining flow downstream of the break, which will be referred to as a "superimposed velocity" to indicate that there is a net fluid velocity perpendicular to the break flow.

Zuber indicated that currently used thermal hydraulic computer codes cannot predict satisfactorily either the amount of liquid or gas entrainment or the beginning of entrainment. Houdayer et al. /15/ also pointed out the necessity of performing experiments for typical PWR geometries, to be incorporated in the CATHARE code for calculating small or large break LOCA.

Stimulated by Zuber's statements, some investigations were initiated where besides the beginning of entrainment, also the quality and mass-flux through the break were studied:
Crowley and Rothe /16/ performed a few air-water experiments at a system pressure of 0.3 MPa with a horizontal 66.6 mm I.D. pipe and a 6.3 mm ID side orifice. The afflux was symmetrical from both ends of the pipe.

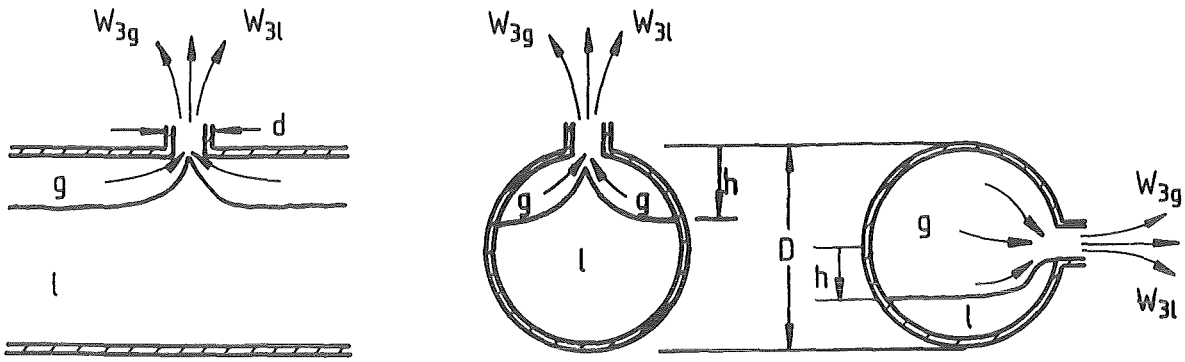

Liquid entrainment due to Bernoulli effect.

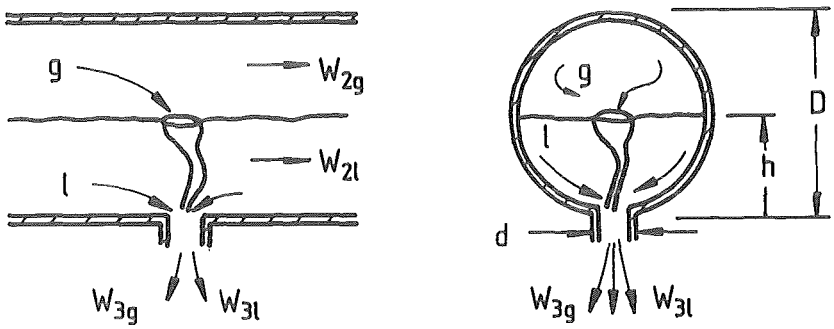

Gas entrainment due to vortex formation.

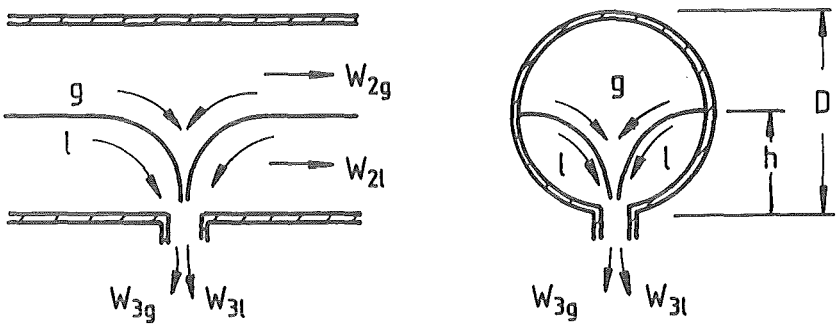

Gas entrainment in vortex free flow.

Fig. 1: Illustration of mechanisms of liquid and gas entrainment in small breaks (from Zuber /14/).

Reimann and Khan /17, 18/ simulated the breaks with T-junctions having a ratio of branch to main pipe diameter $d/D \ll 1$. The authors investigated the air-water flow through a downward orientated branch (d = 6,12 and 20 mm) for different flow conditions in a horizontal pipe with D = 206 mm.

The present work was carried out as a continuation of the investigation initiated by Reiman and Khan: using the same experimental facilities, additional measurements were made with downward branches and further experiments were performed with upward and sideward branches. This report contains:

- The description of the experiments and flow phenomena.
- A general correlation for the beginning of gas and liquid entrainment.
- A model to predict the branch quality and mass flux.
- Extrapolated results for steam-water flows at high pressures.

2. Experimental Setup

The test facility was the same as used in the previous experiments /17, 18/; Fig. 2 shows a scheme of the air-water loop; details are presented in /19/. The air is supplied to the loop by a system consisting of four piston compressors followed by an air cooler, an air filter, a spring tube manometer and a mercury thermometer. Cold water is supplied from a reservoir with a circulating pump equipped with a speed controlled D.C. motor. The water temperature and absolute pressure can be measured at the exit of the pump. For steady-state conditions at a maximum system pressure of 11 bar, the air-compressors and water-pump provide maximum mass flow rates of 1 kg/s and 30 kg/s respectively. As shown by the digram in Fig. 2, two measurement sections of NW 100 and NW 50, respectively, exist for each phase. The gas and liquid mass flow rates can be determined with one orifice in the NW 100 sections and three exchangeable orifices with different mass flow rates but the same ΔP range in the NW 50 sections. The pressure upstream of the orifices is measured with spring tube manometers and the pressure drop through the orifices is determined with 0-1400 mm mercury-U-manometers. Downstream of the test section the air-water mixture is carried into a cyclon and, subsequently, the separated air is released to the outside and the water is transferred into the reservoir which feeds the pump.

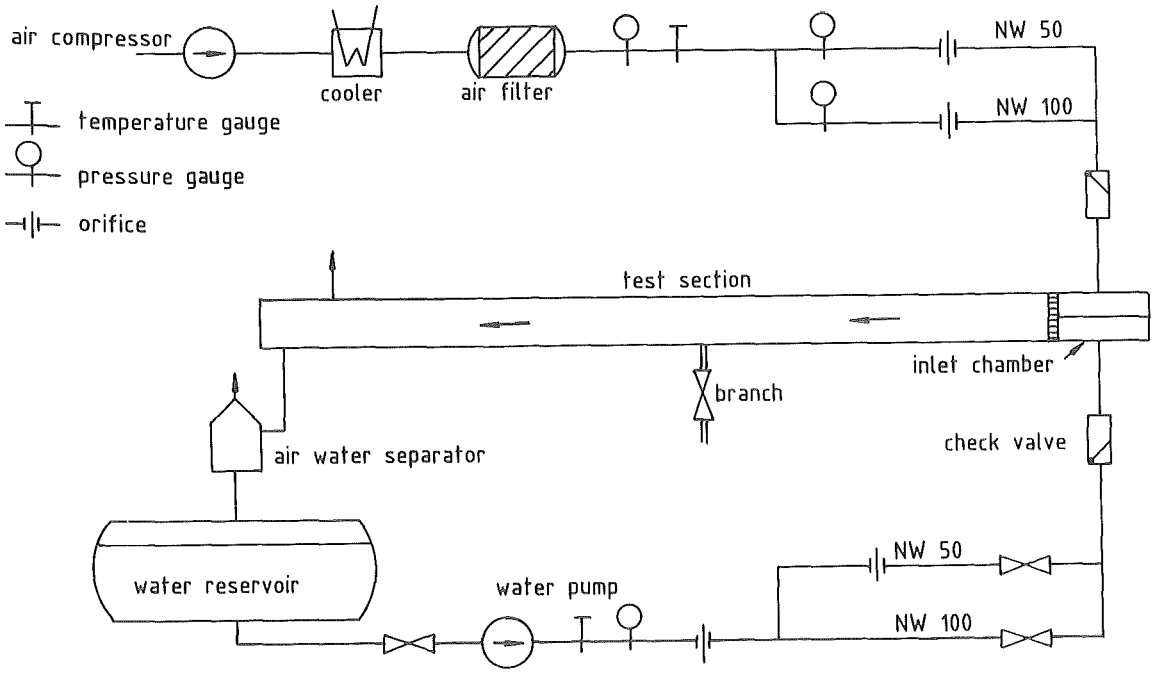

Fig. 2: Two-phase flow air-water loop.

Fig. 3 shows schematically the test section; the inlet, run and branch variables are characterized by the indices 1, 2 and 3 respectively. Metered air and water flows (W_{1g}, W_{1l}) enter the horizontal pipe of 206 mm ID and a total length of about 6 m. The inlet is provided with a chamber specially designed to favor stratified flow (see photograph in Fig. 4a).

A short transparent section of the pipe, made of plexiglass and located about 4.5 m downstream of the inlet, can be connected to branches with different diameters and orientations. Downstream of the branch a 50 mm ID pipe with a throttle valve (V3) leads to a separator or directly to a water tank for weight measurements to determine the branch liquid mass flow rate W_{3l}. The branch gas mass flow rate W_{3g} can be measured at the exit of the separator with the orifice preceding the valve V3g.

About 1 m downstream of the plexiglass section a movable weir is used to change the liquid level in the test section independently of the rate of liquid flow entering the horizontal pipe. The end of the test section can be removed (Section A-A in Fig. 3) to observe the flow field in the direction of the pipe axis, through a window provided in the flange closing the pipe.

At the exit of the test section the mixture can be throttled to atmospheric pressure through the valve V2. To prevent pressure oscillations which occur when a slug-type two-phase flow is throttled, it is important to assure that the flow leaves the test section homogeneously mixed. For that purpose a special homogenizer preceding the valve V2 is used. The dispositive consists essentially of 60 vertical short pipes fixed to a plate as shown in Fig. 4b. Each pipe has two longitudinal slots which allow the two phase flow to fill all the pipes simultaneously. The liquid accumulates at the bottom of the bundle whereas the gas fills the upper portion above the liquid. Independent on the interface level, gas and liquid flow homogeneously mixed through each pipe and therefore the total mixture flows homogeneously.

When only water flows through the valve V2, the orifice preceding the valve V2g is used to measure the gas mass flow rate W_{2g} at the end of the test section.

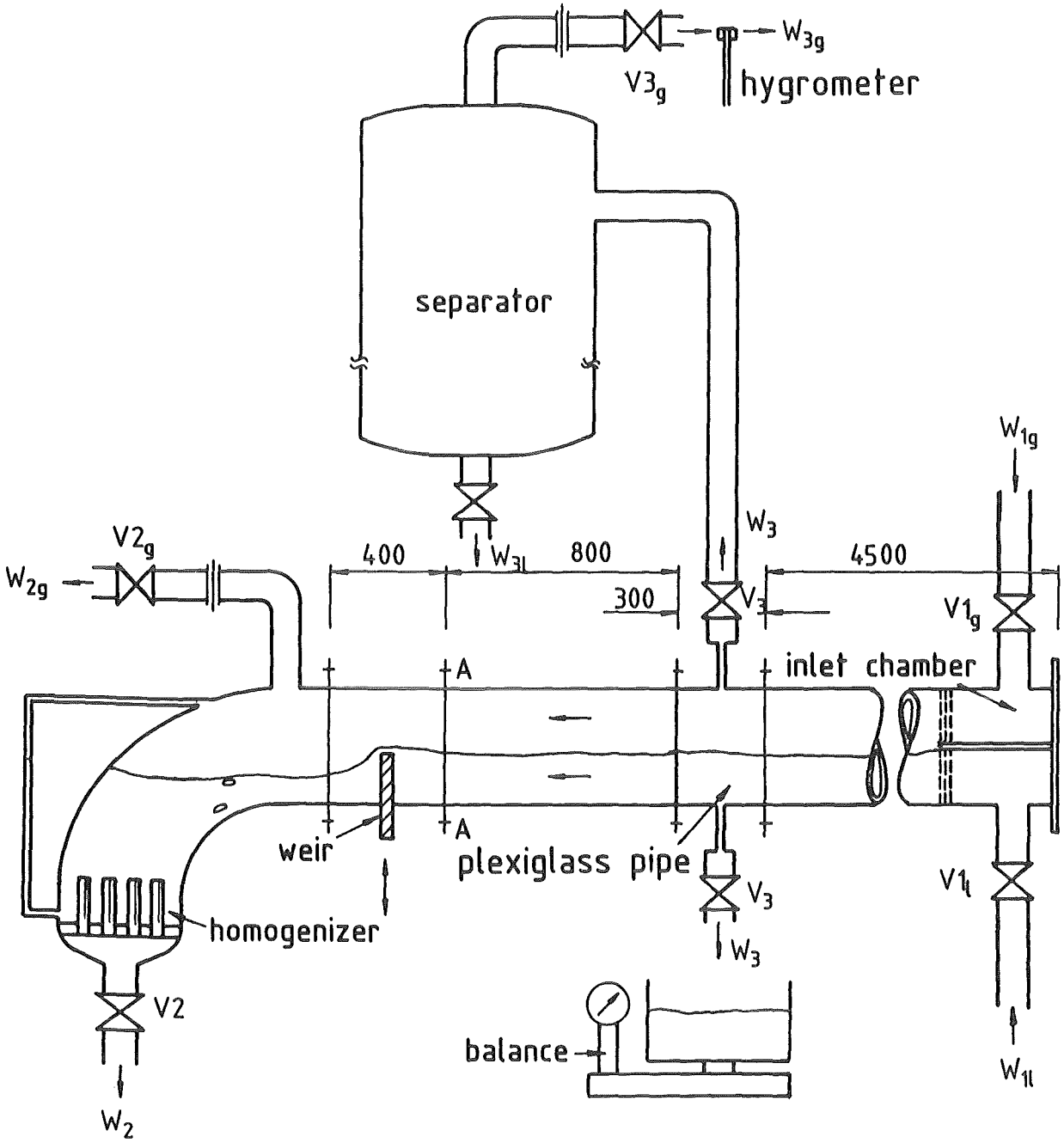

Fig. 3: Test section used for general measurements.

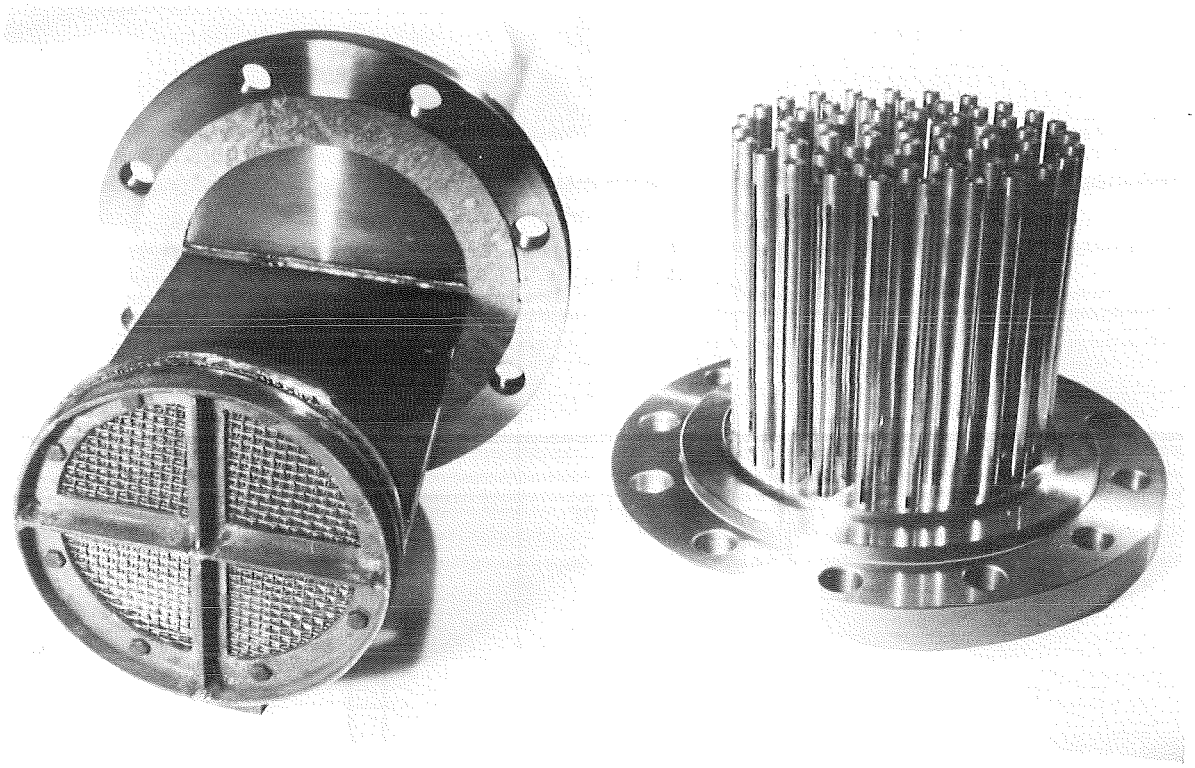

a) Inlet Chamber b) Homogenizer

Fig. 4: Details of the test section for small break experiments.

Fig. 5 shows details of the plexiglass pipe. This transparent section contains the branch inserts and allows visual observation of the flow phenomena in the vicinity of the branch entrance. In the main pipe, about 0.5 m upstream of the T-junction, a pressure tap is connected with the absolute pressure transducer P_1 and with differential pressure transducers for measurements of the liquid level ΔP_{h1} and branch pressure drops ΔP_{1-3}. The liquid level h_1, is also given by a vertical scale downstream of the branch in the plexiglass section.

The branches having a length of 55 mm and an ID of 6, 8, 12 or 20 mm, are pipe studs machined in interchangeable inserts with a sharp-edged entrance. Details are presented in Fig. 6. Four pressure taps at different positions along the branch axis are connected with absolute spring manometers (P_{31}, P_{32}, P_{33}, P_{34}) and with differential pressure transducers to measure the pressure differences ΔP_{1-31}, ΔP_{1-32}, etc. Just downstream of the branch, the 50 mm ID pipe contains a tap for additional pressure measurements (P_{35}).

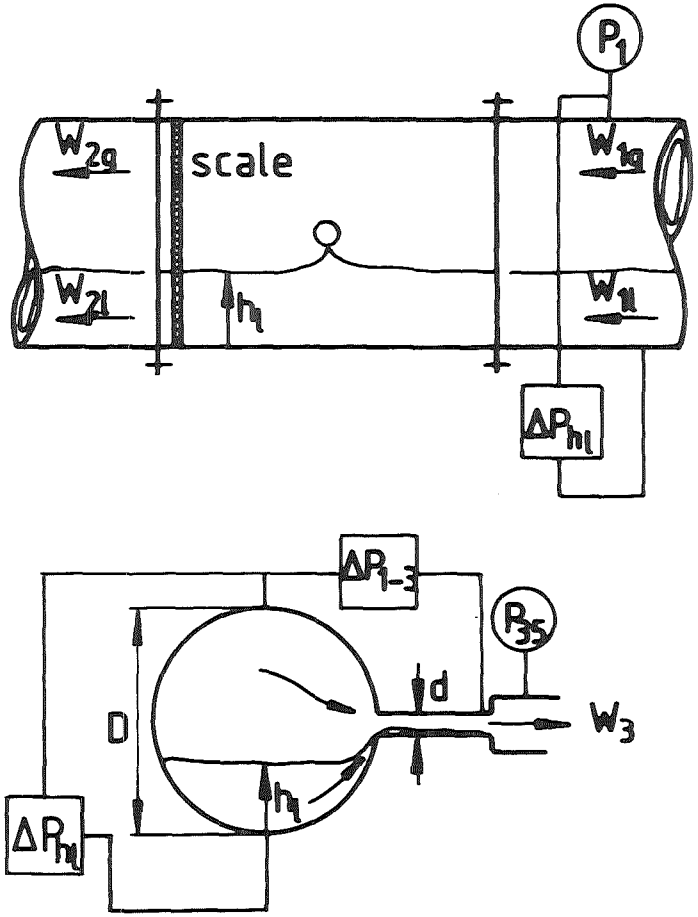

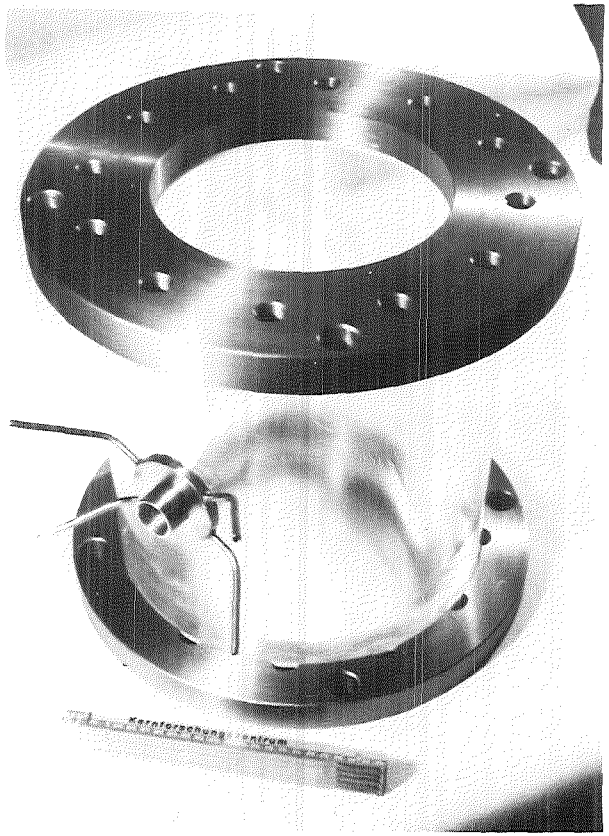

Fig. 5: Details of the plexiglass pipe containing the branch inserts.

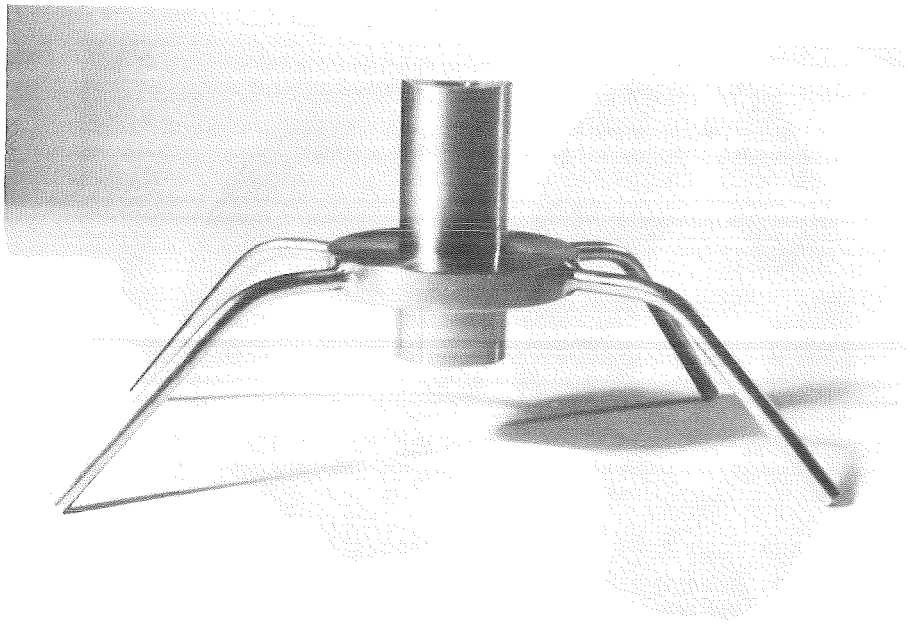

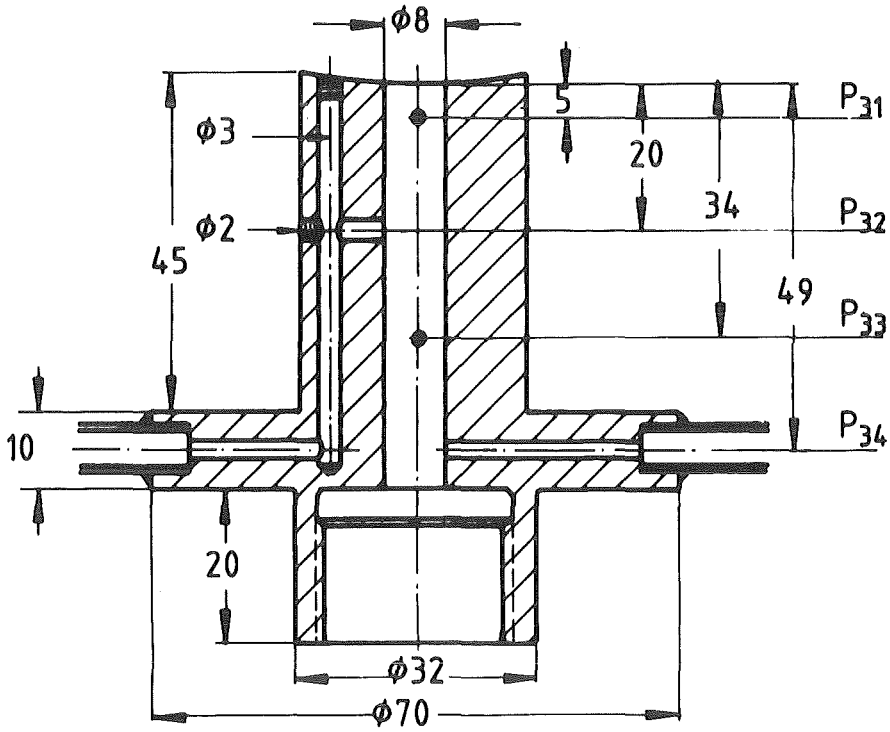

Fig. 6: Photo and details of the pipe studs used to simulate the breaks (Branches).

3. Description of the Experiments

3.1 General Characteristics

3.1.1 Experimental Method

The experiments were performed with stratified co-current air-water flow in the horizontal main pipe with different interface levels; the system was at ambient temperature and at a maximum pressure of 0.5 MPa. The differential pressure ΔP_{1-34} was varied between 0.01 and 0.4 MPa by means of the throttle valve V3 downstream of the branch. By continuously decreasing the absolute pressure P_{35}, the critical branch mass flux was evidenced by a constant reading of the pressure differences ΔP_{1-3}. Most of the experiments were performed with subcritical branch mass-fluxes. The fluctuations of ΔP_{1-34} increased drastically when entrainment began; therefore, the corresponding signals from the printout of the differential pressure transducer were used, in addition to visual observations, to determine the beginning of entrainment. For quantitative measurements an integrated reading from a voltmeter was used.

The flow field in the vicinity of the branch entrance was observed visually through the plexiglass test section, or through the window at the end of the horizontal pipe when a liquid film on the plexiglass walls made it impossible to observe details of the flow pattern.

During the experiments the interface level h_1 was fixed by regulating the liquid inflow and outflow and, when the measurement of W_{2g} was of interest, the interface level at the end of the test section was controlled visually with a transparent U-tube and kept constant at such a position that no bubbles were pulled through valve V2.

Branch Orientation	Superficial Velocities					
	v_{1sg} m/s	v_{2sg} m/s	v_{3sg} m/s	v_{1sl} m/s	v_{2sl} m/s	v_{3sl} m/s
Downward*	0.495	0.109	84.72	0.154	0.095	24.71
Upward	0.711	0.253	155	0.087	0.087	0.035
Horizontal	1.068	1.020	169	0.334	0.328	17.0

Table 1: Maximum superficial velocities registered in the test section and branches. * Data from /17, 18/.

The maximum superficial velocities used in the experiments, defined as the maximum ratios of single phase volume flow rates to total cross section, are summarized in the Table above.

3.1.2 Measurements Accuracy

The error in the measured pressures, temperature, liquid level and water weight, constitute the main contributions to the error in the variables calculated from the present experiments. The method used to determine the propagated errors is presented in Appendix A1.

The absolute error for the pressure measured with spring tube manometers ranges between ± 0.05 bar for steady-state single-phase flow and ± 0.2 bar for the very unstable two phase flows occurring in the branches. In these cases, however, the integrated digital reading from the voltmeter used to determine the pressure differences ΔP_{1-31}, ΔP_{1-32}, etc. has a relative error <0.5 % of the full scale. Therefore, maximal absolute errors of ± 0.01, ± 0.05, ± 0.1 and ± 0.25 bar can be assigned to pressure differences below 0.2, 1, 2 and 5 bar, respectively, at the end of the scale. The absolute error in the reading from the U-tube mercury manometers range between ± 1 mm Hg for very stable flow and ± 10 mm Hg when fluctuations occur.

The error for the absolute temperature T measured with Mercury thermometers is about ± 1.5 K.

The rates of single phase gas and liquid mass flow through the orifices were determined with equations of the form: $W_g = c_g\ (P_o\ \Delta P_o/T_o)^{0.5}$ and $W_l = c_l(\rho_l \Delta P_o)^{0.5}$, where c_g and c_l are the orifice calibration coefficients for gas and liquid, respectively, P_o and T_o are the pressure and temperature upstream of the orifice, and ΔP_o is the pressure drop through the orifice. Using these equations with the typical values for the inflow P_o = 7 bar, T_o = 15 °C and 100 mm Hg < ΔP_o < 1400 mm Hg, the absolute errors estimated above give relative propagated errors in the ranges 1-6 % for W_{lg} and 0.4-5 % for W_{ll}, the maximum relative errors corresponding to minimum mass flow rates. Similar values are valid for mass flow rates measured with the orifices preceding the valves $V2_g$ and $V3_g$.

In the range of the present experiments the density of the water was considered as a constant with negligible error and the density of the air in the test section was given by $\rho_g = c_a\ P_1/T_1$ with $c_a = 348.5$ kg K m^{-3} bar^{-1}, which produces a typical relative error of ± 2.5 %.

For a smooth stratified interface in the main pipe the vertical millimetred scale used to measure liquid levels, allows readings with an absolute error of $\pm$ 1 mm. In experiments with a wavy interface, an estimated mean value of the liquid levels read on the scale and recorded in the printout of the ΔP_{h1} transducer, was considered. The corresponding absolute error depends on the waves amplitude; maximum estimated values are about ± 5 mm.

Measurements of the water weight were made using a balance with a precision of ± 0.1 kg. To measure small quantities of water ($\leq$ 2 liters) accumulated in the separator connected to upward branches, a recipient was used with a scale allowing readings with an error of ± 0.005 liter.

Time intervals were measured using a chronometer with a precision of ± 0.1 sec. However, an estimated error of about ± 3 sec. was introduced by indeterminations in the times corresponding to beginning and end of the measured interval.

3.2 Experiments with Downward Branches

In addition to previous investigations /17, 18/ some experiments were performed to measure the beginning of gas entrainment (b.g.e.) and the gas entrainment (g.e.) without superimposed liquid velocities, that means with V2 closed.

To determine the b.g.e., the input and branch mass flow rates were adjusted in such a way that the interface level decreased very slowly (for instance Δh_1 = 5 mm in 100 sec). The system pressure was kept constant by using a small gas flow regulated with the valves $V1_g$ and $V2_g$. Therefore the experiment can be assumed to be steady-state. The formation of first gas hoses reaching the break outlet and producing a characteristic change in the signal from the ΔP transducers, was considered as the b.g.e. and the corresponding liquid level was recorded.

In experiments to measure the g.e., the valves $V2_g$ and V2 were closed and a balance between the input and break mass flow rates was adjusted to keep the liquid level constant (steady-state experiments). Therefore, the gas and the liquid mass flow rates through the branch were determined with the orifices preceding the main pipe inlet (Fig. 3). In previous experiments with superimposed liquid velocities /17,18/, the branch liquid mass flow rate W_{31} was determined by weighing a timed sample at the exit of the branch, and the superimposed mass flow rate W_{21} was the difference $W_{11}-W_{31}$.

3.3 Experiments with Upward Branches

In this case the beginning of liquid entrainment (b.l.e.) and the liquid entrainment (l.e.) for different interface levels in the main pipe were measured. The small quantity of liquid entrained in upward branches is mixed with a relative high gas mass flow rate. Therefore, for quantitative measurements the experiments were performed with the branch connected to the separator as shown in Fig. 3.

A constant W_{3g} at a constant pressure P_1 was adjusted to a slowly increasing liquid level ($\Delta h_1/\Delta t \simeq 1$ mm/min) and the b.l.e. was determined visually when a few droplets raised from the interface reached the break outlet. Suitable orifices preceding the valve $V3_g$ at the exit of the separator were used to measure W_{3g} and, in case of superimposed gas velocities given by the difference $W_{1g} - W_{3g}$. The highest superimposed gas velocities were limited by the occurrence of high waves or slug flow in the main pipe.

To determine the entrainment rate, it was waited until equilibrium established between liquid inflow and outflow in the test section, and then the water was collected at the bottom of the separator during a defined period of time after which the liquid was measured. In experiments with superimposed liquid velocities the difference $W_{11} - W_{31}$ was used to determine W_{21}.

The liquid-gas interaction due to entrainment phenomena, produces an increased evaporation of water downstream of the branch inlet which leads to underestimation of W_{31}. In order to evaluate this amount of water, the humidity of the branch gas flow was measured at the exit of the separator in some experiments with and without liquid entrainment. The correspondig differences were used to determine the mass of evaporated water, which reached values

between 10 and 20 % of the liquid collected.

3.4 Experiments with Horizontal Branches

With horizontal branches both gas and liquid entrainment can occur depending on the interface level in the main pipe.

To determine the b.g.e. and the g.e., the same procedure as described in 3.2 was applied. For the b.g.e. additional, experiments with superimposed gas or liquid velocities were performed. In these cases the branch gas flow rate is negligible; therefore, W_{2g} was given by the measured W_{1g}; W_{21} was the difference $W_{11} - W_{31}$.

To determine the b.l.e. and the l.e., the method described in 3.3 was followed; however, the separator was not used and the branch was directly connected to the water tank to weigh timed samples.

The b.l.e. started when a very thin film of water raised from the interface moving on the pipe wall and reached the branch entrance. This was observed visually and from a characteristic change in the signal from the ΔP transducer.

For the b.l.e. again additional experiments with superimposed velocities were performed.

4. Flow Phenomena

4.1 Downward Branch

Although in the present investigations the experiments with downward branches were performed always with V2 closed, the description and photographs of the flow with superimposed liquid velocities (from /17, 18/), will be included to get a complete picture of the flow phenomena.

If liquid is supplied to the test section with the valve V2 closed, the inflow rate is equal to the branch flow rate and no liquid flow perpendicular to the branch axis results. This situation is unstable with regard to the enhancement of velocity components around to the branch axis and causes a vortex flow, Figs. 7-8 (from /17, 18/). The vortex axis is deflected somewhat in the direction opposite to the inflow side and the gas entrainment starts when a very thin gas hose reaches the branch inlet (Fig. 7).

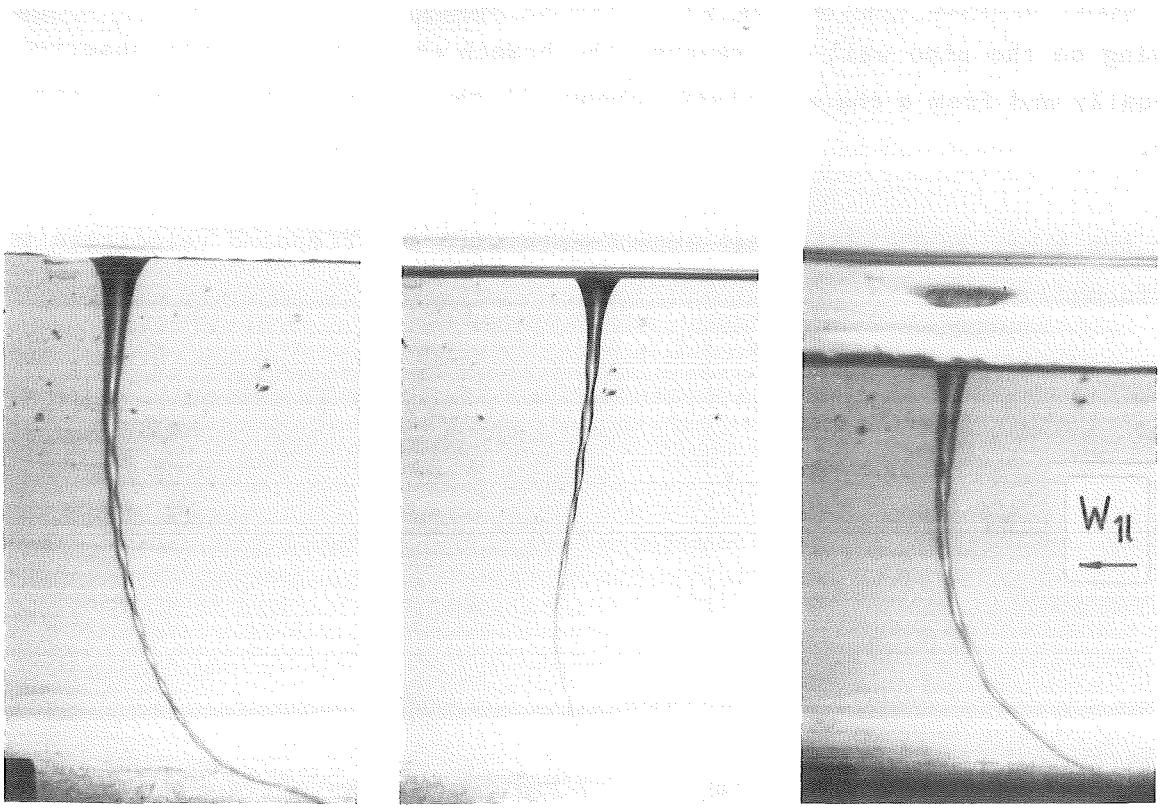

Fig. 7: Beginning of gas entrainment in downward branch (from /17,18/).

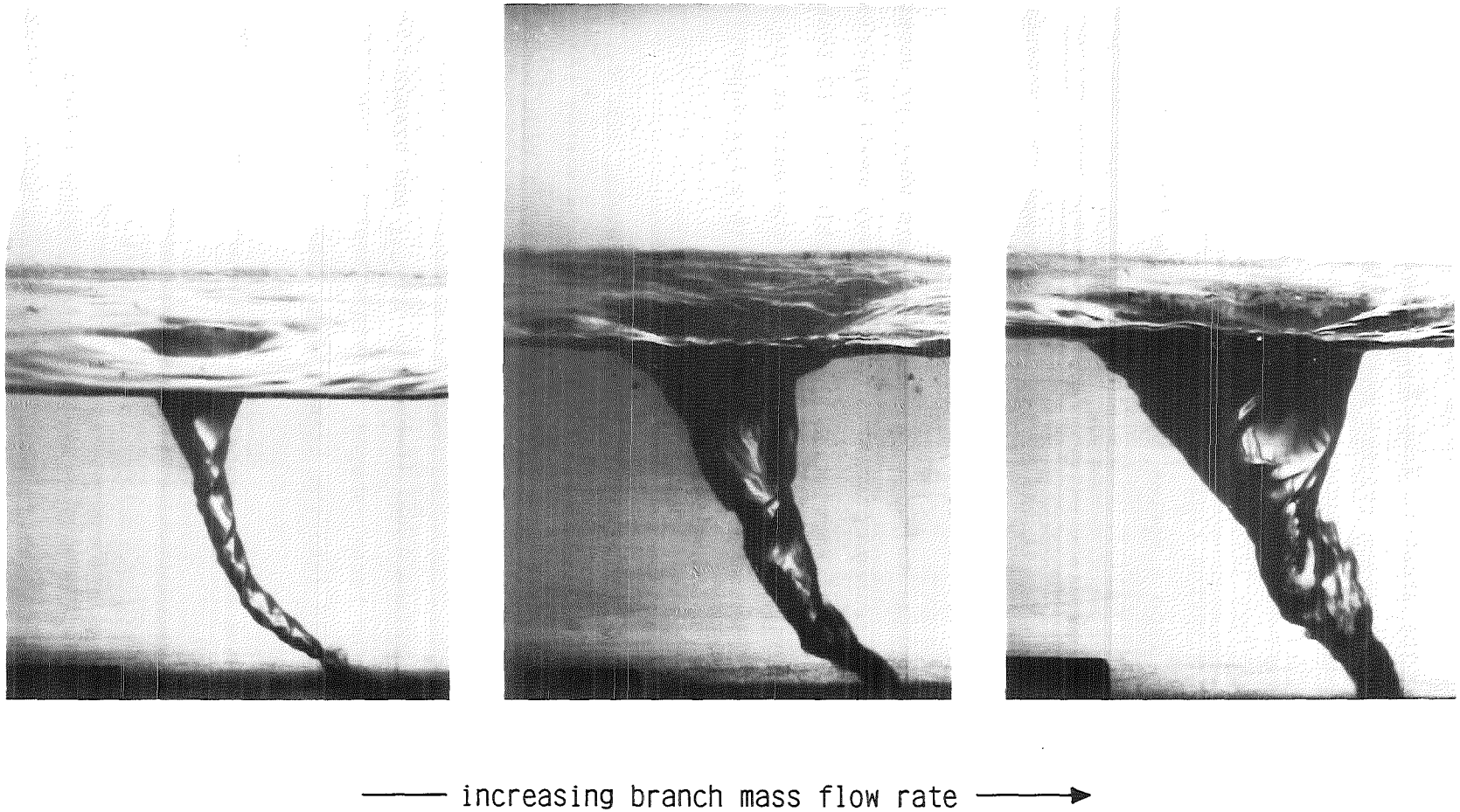

Fig. 8: Development of gas entrainment in downward branch for increasing W_3; $W_{21} = 0$ (from /17, 18/).

This first gas hose is not stable but swept away after some seconds, and a long time can pass until another gas hose is formed. By lowering the interface level or increasing the pressure drop Δp_{1-34} and branch mass flow rate, respectively, the gas hose becomes thicker and more stable (Fig. 8).

In Fig. 9.a the spiral-type streamlines at the interface are clearly seen. By lowering further the interface level a condition is reached where the water flow pattern changes from vortex flow to vortex-free flow (Figure 9.b). A reason for the transition from a vortex to a vortex free flow field is the increasing influence of the wall friction with decreasing interface levels. Dagget and Keulegan /9/ found, in similar experiments, that near the bottom of a vessel the radial velocity of the vortex increases and the tangential velocity rapidly decreases due to the development of a boundary layer.

Another transition from vortex to vortex free flow occurs when the superimposed liquid velocity exceeds a certain value. With very small superimposed velocities ($V_{21} \leq 0.06$ m/s) the vortices are very unstable (Fig. 10 from /20/). Such low values of v_{21} were obtained by raising the weir at the end of the test section, which gives a high interface level with a low superimposed velocity.

At higher superimposed velocities with low interface levels, e.g. $v_{21} = 0.25$ m/s, the flow field observed in the experiments was always vortex free as shown in Fig. 11 (from /17, 18/). The photograph 11a shows a test point without gas entrainment but an already considerably deflected interface.

At a slightly lowered interface level (increased ΔP_{1-34} and branch flow, respectively) the tip of the funnel-shaped interface begins to oscillate and gas is intermittently sucked into the branch (Fig. 11b).

At lower interface levels a continuous gas pull-through is reached (Fig. 11c).

4.2 Upward Branch

For liquid levels far below the branch entrance and constant values of ΔP_{1-34} and W_{3g}, only gas enters the branch, the interface being a nearly ideal horizontal plane. Due to the acceleration of the gas entering the

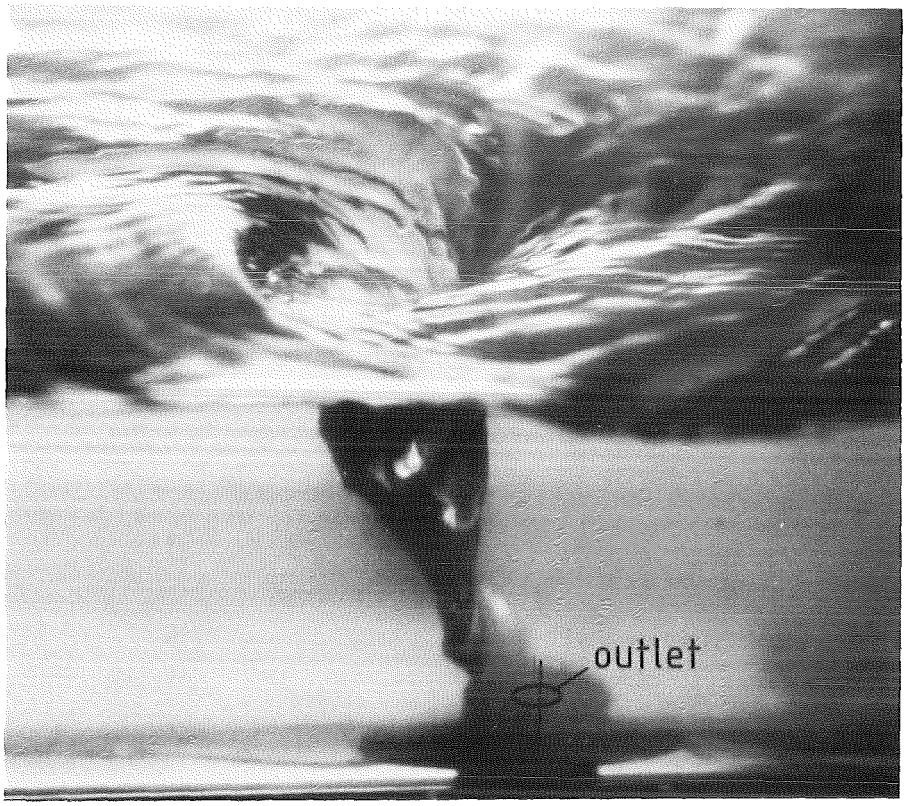

a) strong vorticity at intermediate interface level

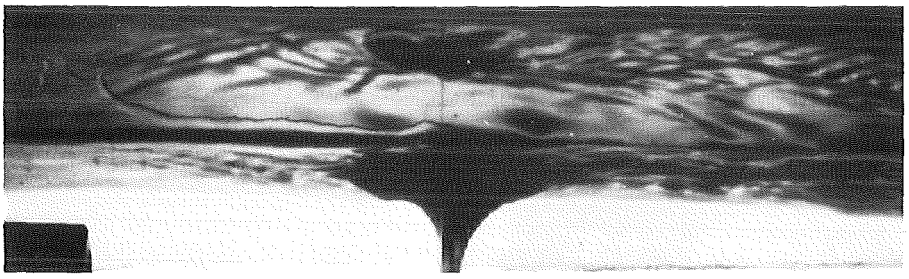

b) vortex free flow at low interface level

Fig. 9: Gas entrainment in downward branch; $W_{21} = 0$ (from /17, 18/).

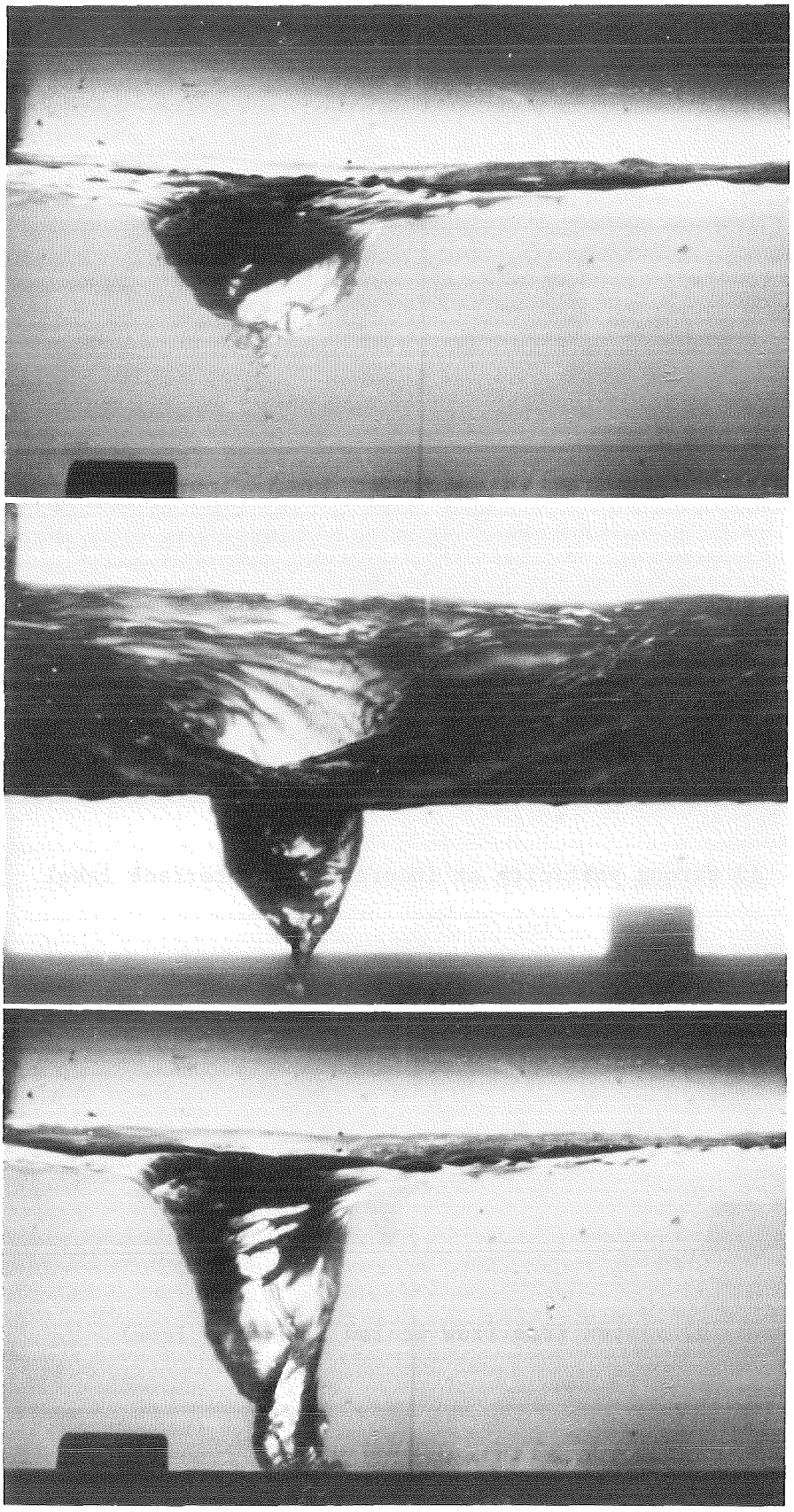

Fig. 10: Unstable vortex gas entrainment in downward branch occurring at high interface level with v_{21} 0.04 m/s (from /20/).

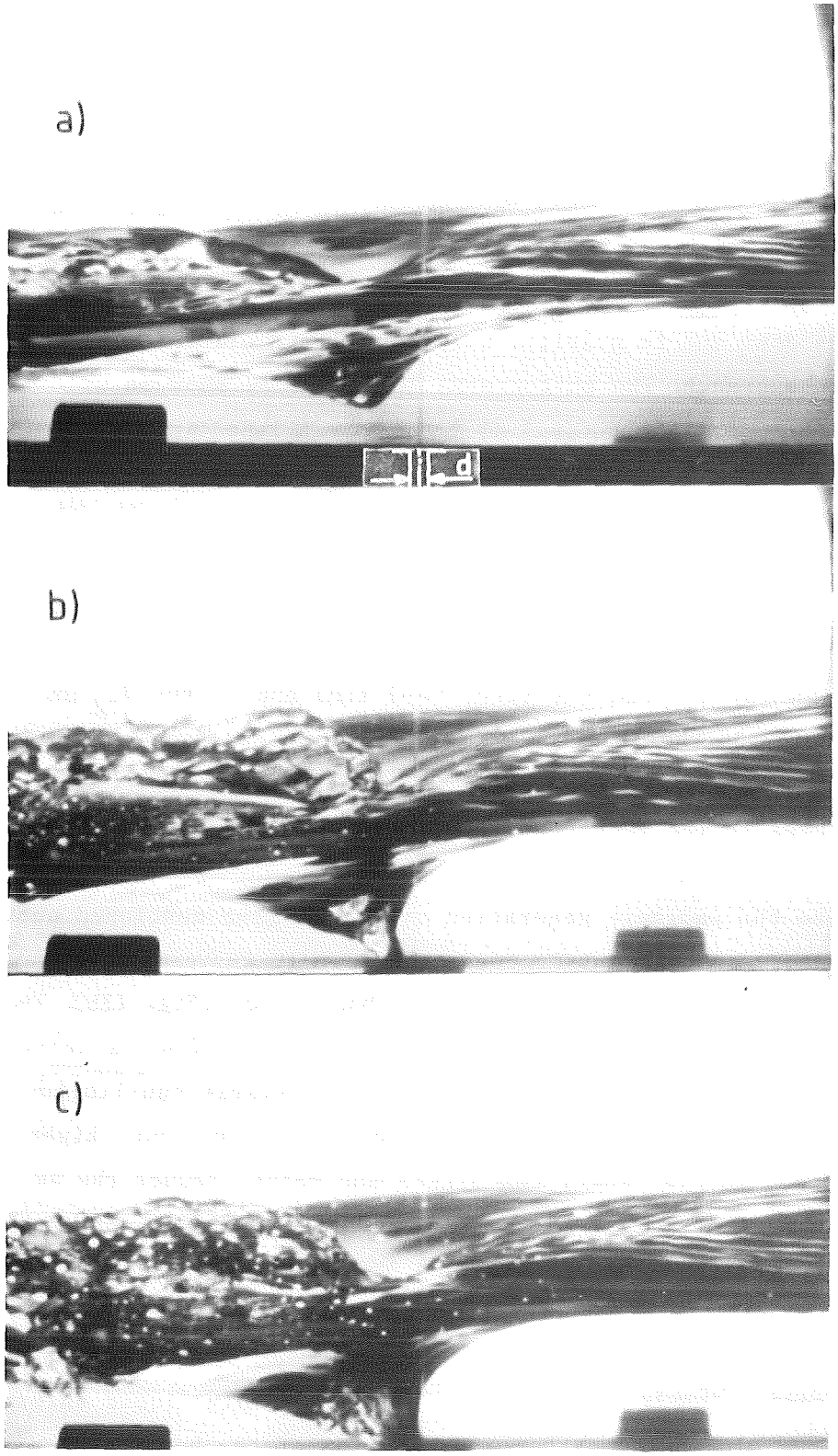

Fig. 11: Development of vortex free gas entrainment in downward branch for v_{21} = 0.3 m/s and increasing ΔP_{1-34} (from /17, 18/):
a) no gas entrainment, ΔP_{1-34} = 0.04 MPa;
b) oscillating gas entrainment, ΔP_{1-34} = 0.065 MPa;
c) continuous gas entrainment, ΔP_{1-34} = 0.22 MPa.

branch the pressure above the interface is lowered (Bernoulli effect) and the interface below the branch entrance is locally raised.

Fig. 12 (from /21/) shows sequences of photographs (48 pictures/s) taken from the end of the horizontal pipe. A considerable amount of liquid can be torn away from the interface. However, due to the large vorticity of the gas flow, the droplets are radially accelerated and only a small fraction reaches the branch inlet. The droplets hitting the wall give rise to a liquid film which mostly drains down due to gravity; only a small fraction near the inlet is sucked into the branch. The photographs in Figure 12 show an oscillatory behavior of the entrainment (typical frequency $\simeq$ 3 Hz) probably initiated by a momentarily larger amount of liquid entering the branch which causes a decrease of the gas flux. This decrease of gas flux diminishes the liquid entrainment which again increases the gas flux, etc.

Fig. 13 (from /21/) contains photographs taken through the plexiglass test section. The inflow is from the right-hand side and valves $V2_g$ and V2 are closed. In photo 13a the location of the maximum interface deflection (lowest local pressure) is shifted some centimeters to the left side. This asymmetry also contributes to the fact that the liquid portion reaching the branch is small.

In addition to the periodic generation of entrainment mentioned above, another oscillatory entrainment process occurred; It was caused by low amplitude interface waves with wavelengths λ of about 15 cm (Fig. 13b). These are surface gravity waves driven by a balance between the fluid's inertia and its tendency, under gravity, to return to a state of stable equilibrium with the heavier fluid (water) underlying the lighter (air) (see e.g. Lighthill /22/). Such waves occur at high inlet gas fluxes and rather reduce the amount of liquid entrainment or decrease the distance between branch entrance and interface at the beginning of entrainment. A further increase of the gas inflow rate finally causes the transition from stratified to slug flow by growing low-frequency waves of wavelengths of the order of the pipe diameter. Fig. 13c shows a test point in the slug flow regime: mainly liquid enters the branch when the slug bridges the cross section of the horizontal pipe, and the time averaged branch liquid flow rate is considerably increased. The occurrence of slug flow is coupled to strong pressure oscillations in the test section, up to several bars in the present experiments. This flow regime was therefore generally avoided.

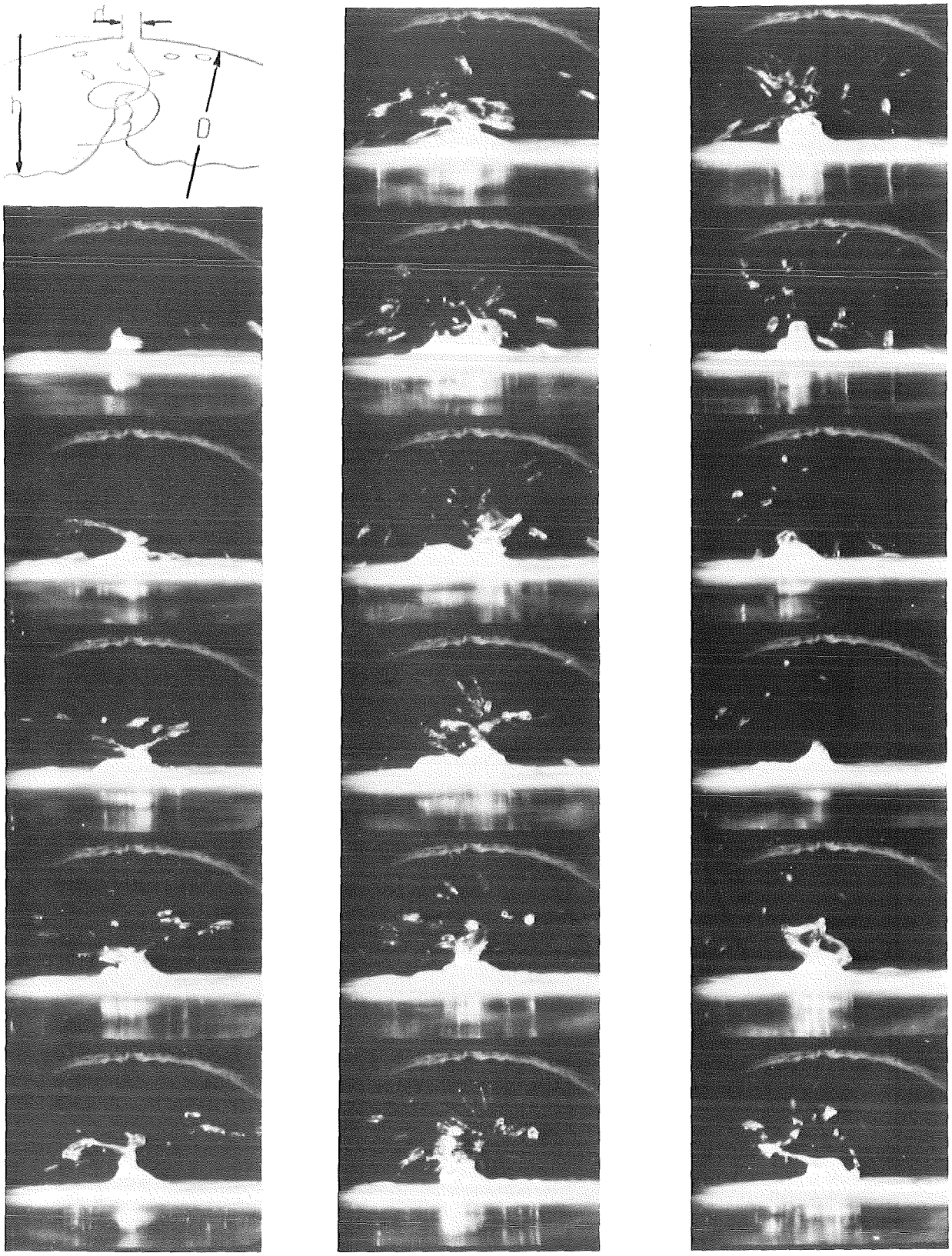

Fig. 12: Oscillatory liquid entrainment in upward branch:
$h/D = 0.3$; $W_{3g} = 0.06$ kg/s; $P_1 = 0.4$ MPa(from /21/).

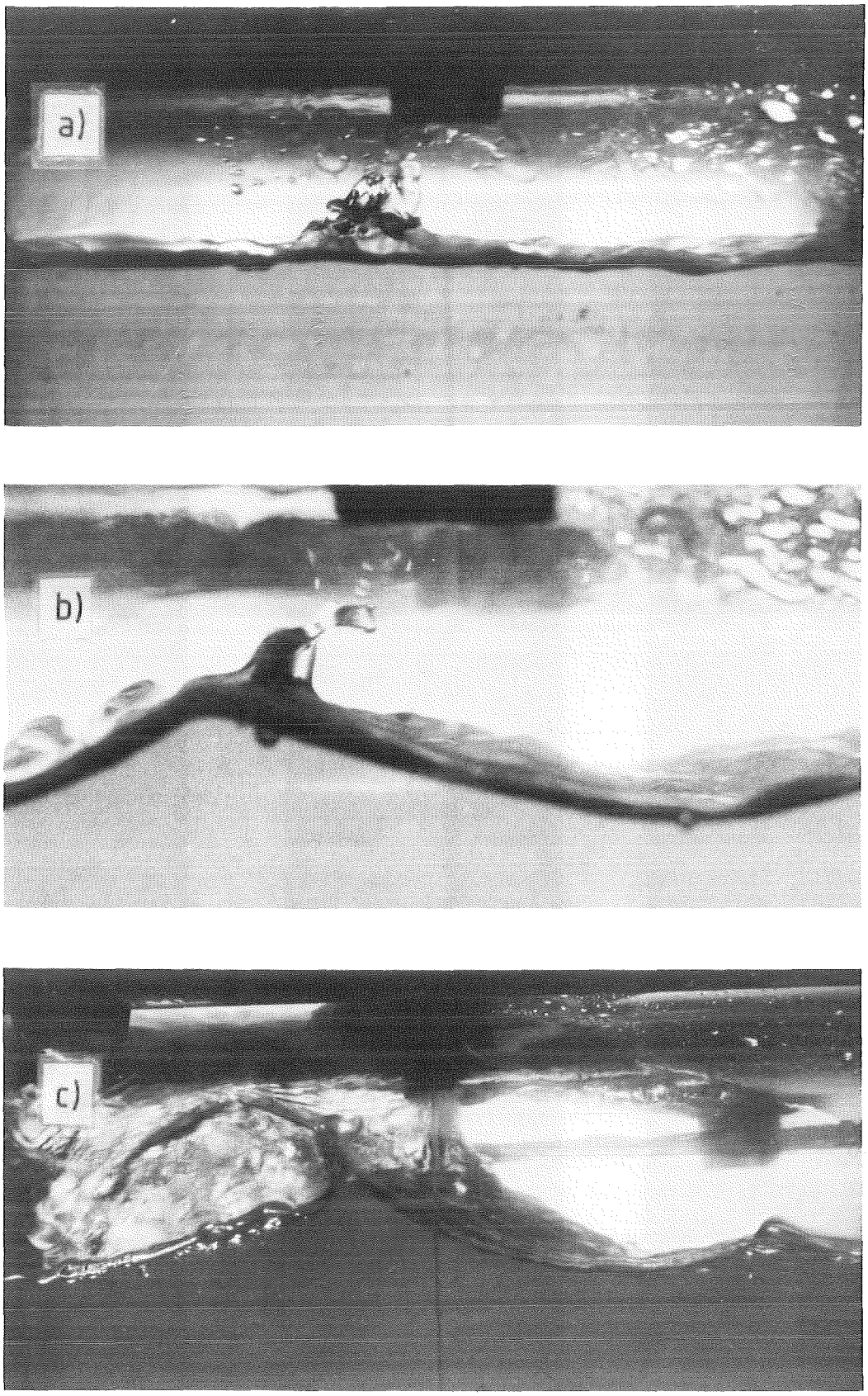

Fig. 13: Liquid entrainment in upward branch for different flow regimes in the horizontal pipe and $v_{2g} = 0$ (from /21/): a) stratified, b) wavy, c) slugging

The effect of superimposed gas velocities was a slight displacement of the vortex axis and deflected interface in the direction of the outflow. This phenomenon is illustrated by the photographs in Fig. 14 corresponding to experiments with $v_{2g} \simeq 0.4$ m/s. The comparison with Fig. 13 shows an increased distance between the raised interface and the branch axis which again delays the beginning of entrainment. Higher values of the superimposed gas velocities produce the waves and slug flow described above and, due to this limitation in the maximum value of v_{2g}, the transition from vortex to vortex free flow with increasing superimposed velocities could not be observed.

No effect of the superimposed liquid velocities on the position of the deflected interface was observed in the range covered by the present experiments ($v_{21} \leqslant 0.12$ m/s).

Fig. 14:
Beginning of liquid entrainment in upward branch for increasing h_1; $v_{2g} \simeq 0.4$ m/s.

4.3 Horizontal Branch

For this geometry the flow field configuration is clearly different from those observed in downward and upward branches.

With the interface below the branch axis again liquid entrainment can occur. The Bernoulli effect is first evidenced by the deflection of the interface in the vicinity of the pipe wall and, with further increase of the liquid level, a thin ascendent film of water, not influenced by vorticity, determines the b.l.e. With a superimposed gas velocity no appreciable displacement of this water film occurs because the friction forces dominate at the wall. Again no influence of the superimposed liquid velocities on the ascendent liquid film is observed.

The photographs in Fig. 15 show the ascendent liquid during entrainment for different liquid levels in the main pipe and $\Delta P_{1-34} \cong 0.04$ MPa. Due to the strong acceleration near the branch entrance, the liquid film is dispersed into very small droplets entering the branch. Fig. 16 shows photographs in the direction of the pipe axis, for a fixed position of the interface and increasing pressure differences. For the higher ΔP_{1-34} (Fig. 16c), the dispersed flow near the entrance is clearly seen.

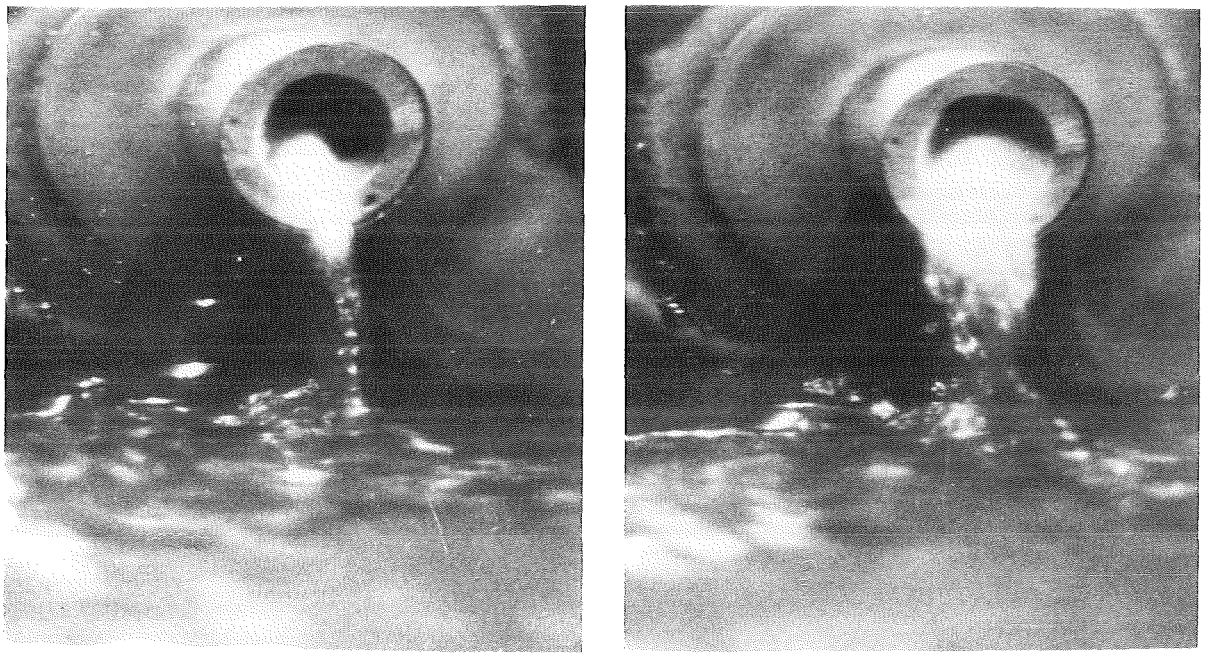

a) h_1 = 176 mm b) h_1 = 182 mm

Fig. 15: Liquid entrainment in horizontal branch: $\Delta P_{1-34} \cong 0.04$ MPa.

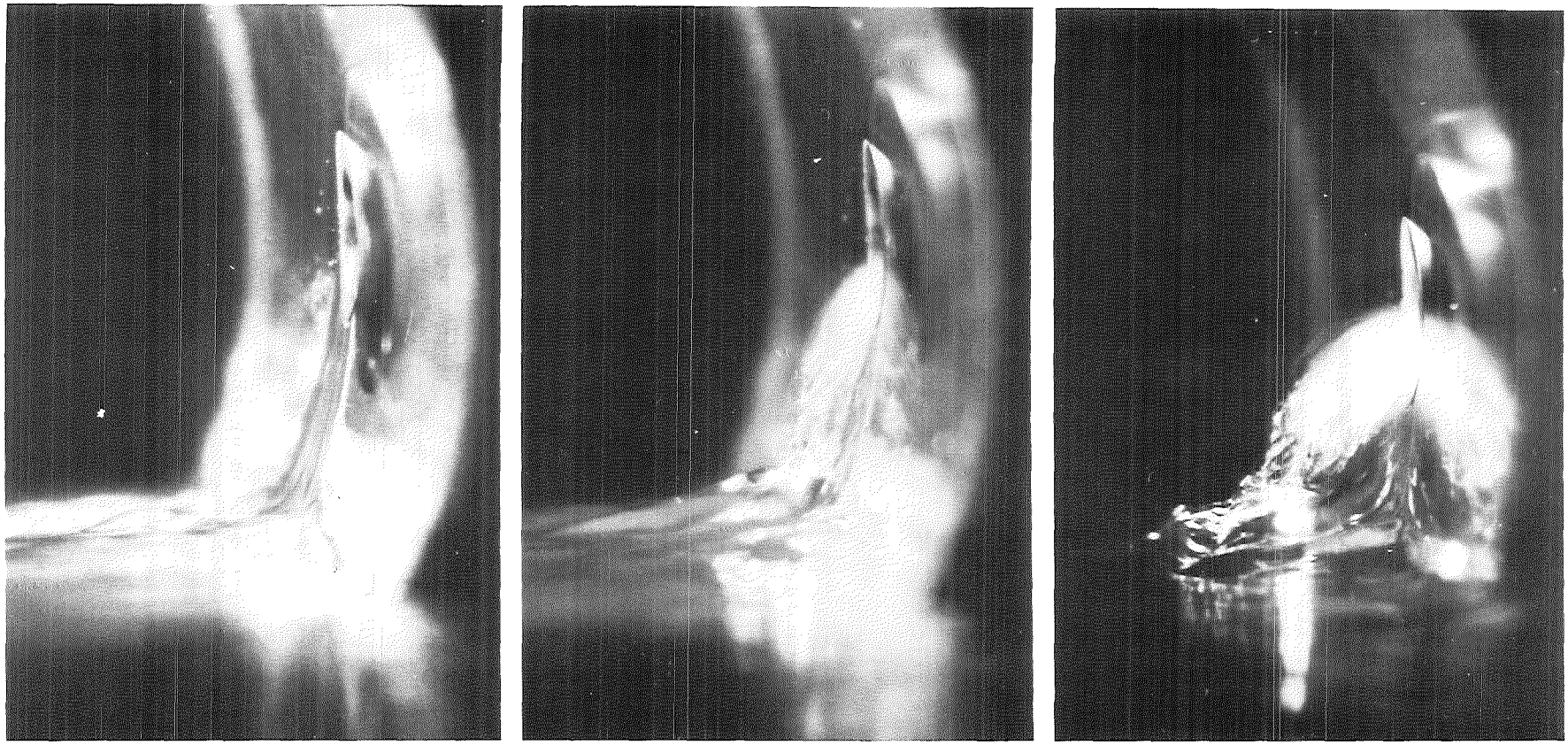

a) ΔP_{1-34} = 0.02 MPa, b) ΔP_{1-34} = 0.04 MPa, c) ΔP_{1-34} = 0.06 MPa.

Fig. 16: Liquid entrainment in horizontal branch for increasing ΔP_{1-34}, h_1 = 183 mm

With the liquid level above the branch axis, again gas entrainment can occur. The continuous liquid phase exhibits a very small vorticity difficult to observe on the interface. Along the vortex axis, at a short distance from the pipe wall, thin hoses of gas reach the branch entrance and determine the b.g.e. If the interface level is further lowered or ΔP_{1-34} increased, the initial hoses of gas are observed to approach rapidly the pipe wall. The wall friction prevent the vorticity from developing and after short intermittences the gas is in direct contact with the wall. Thus, the vorticity is completely suppressed and a vortex free gas flow exist between the liquid and the pipe wall.

4.4 Transition from Stratified to Slug Flow

For high interface levels in the main pipe, which were of interest in the investigation involving upward branches, the transition from stratified to slug flow occurred. Specific experiments were performed to determine the conditions for this transition: With the valve for water drain closed, sufficient liquid was provided to fill the main pipe up to the desired level. Then a slowly increasing gas flow rate was adjusted by opening gradually the valve $V1_g$. The air was released to the atmosphere either through valve $V2_g$ or through the branch. The evolution of the flow field was observed visually: at low air flow rates, the water surface was horizontal and smooth, in the sense that only capillary waves or small ripples with $\lambda < 5$ cm were observed. With these disturbances the effect of the surface tension acting as a restoring force is comparable with the effect of gravity; therefore, these waves are unable to propagate and disappear almost instantaneously if the air flow is suppressed (see Lighthill /22/). A higher air flow gave rise to uniform small waves, with $\lambda > 10$ cm, for which the influence of the surface tension is negligible (compare /22/) and therefore they can be considered as pure gravity waves.

With an increasing gas flow, the action of the air moving in the same direction as the waves but at a greater velocity, is an excess of pressure on the rear slopes and a tangential drag on the crests. The wave amplitude will tend to increase to such an extent that the dissipation balances the work done by the surface forces (see e.g. Lamb /23/). Thus, the air flow was increased until waves developed whose crests reached the top of the pipe: the air flow rate causing this slugging flow, was recorded and a new experiment with a

different initial interface level was performed.

To analyze the experimental data, the model proposed by Taitel and Dukler /24, 25/ was first considered. The authors assume that the transition takes place as a result of the Kelvin-Helmholtz instability causing waves of finite size on the stratified film. The wavelength at which the stratified flow becomes unstable depends on gravity and surface tension, and the instability is produced by the decrease of the pressure over the waves, due to the Bernoulli effect when gas accelerates locally over the liquid. The transition from stratified to elongated bubble or slug flow patterns occurs when the lifting Bernoulli forces resulting from the decrease of the pressure over the wave, overcome the downward gravity forces.

On this basis, Taitel and Dukler deduced a relationship, valid for horizontal round pipes which allows to predict the gas phase velocity at which the transition occurs:

$$v_g \geq \frac{h_g}{D}\left[\frac{(\rho_l-\rho_g)\, g\, A_g}{\rho_g\, A'_l}\right]^{0.5} \qquad (1)$$

where: $A'_1 = D[1-(2h_1/D-1)^2]^{1/2}$

v_g = gas phase velocity

h_g = gap of gas above the liquid

h_1 = height of the liquid from the pipe bottom

D = diameter of the pipe

$\rho_{1,g}$ = liquid, gas density

g = acceleration of gravity

A_g = gas-flow cross-sectional area

Eq. (1) predicts a decrease of v_g with decreasing h_g. In the present experiments however, independent of the liquid level in the main pipe, a nearly constant value of the gas phase velocity was measured at the transition. The results are shown in Fig. 17 together with the model proposed by Taitel and Dukler. The method described in Appendix A1 was used to calculate bars of error for points with extremal coordinates.

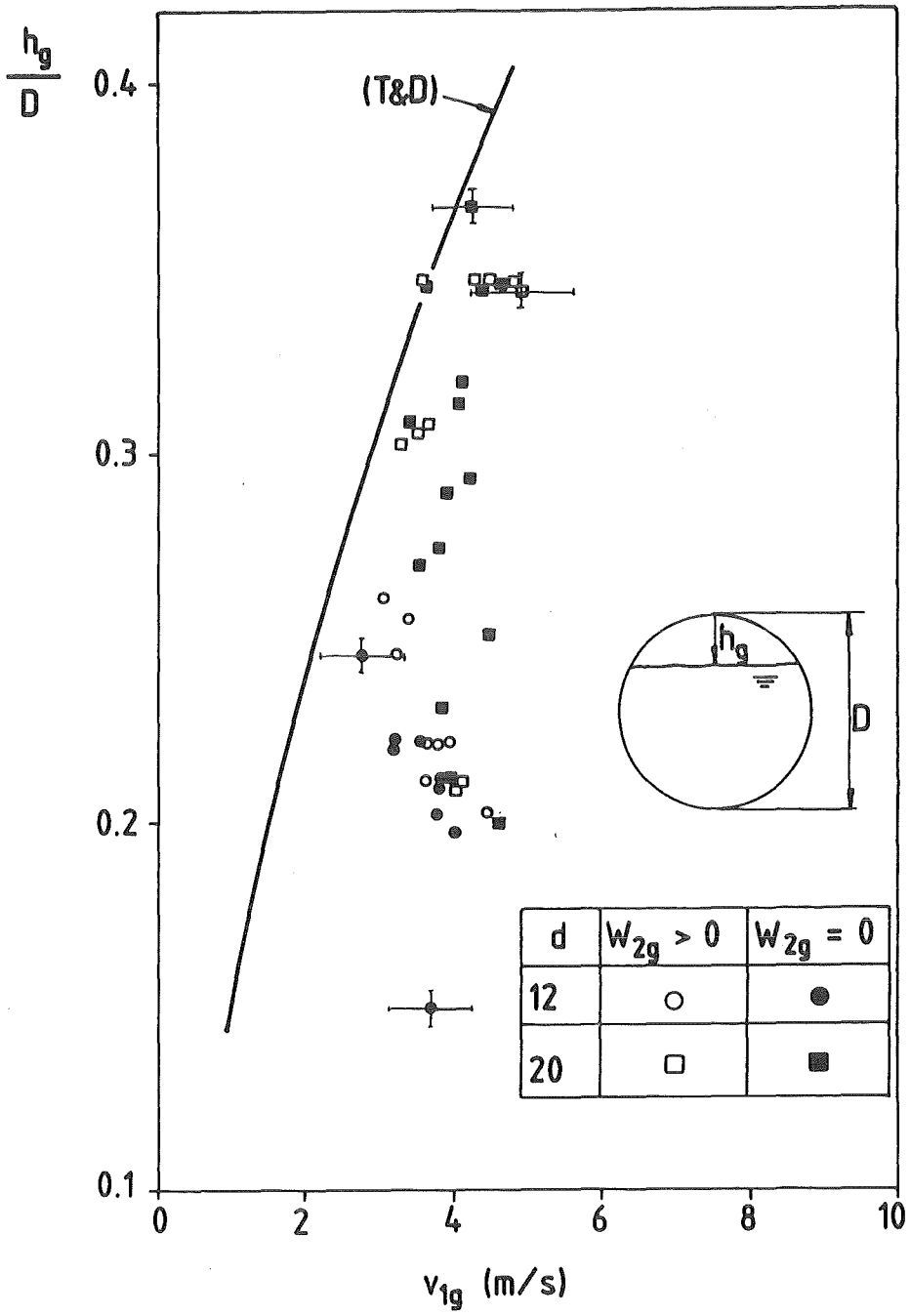

Fig. 17: Transition from stratified to slug flow. Comparison of experimental data with theoretical model from Taitel and Dukler /24, 25/.

The discrepancy between the present results and the model from Taitel and Dukler was evaluated by plotting the ratio of measured v_{1g} to the value given by Eq. (1), as a function of h_g/D. The results are shown in Fig. 18a.

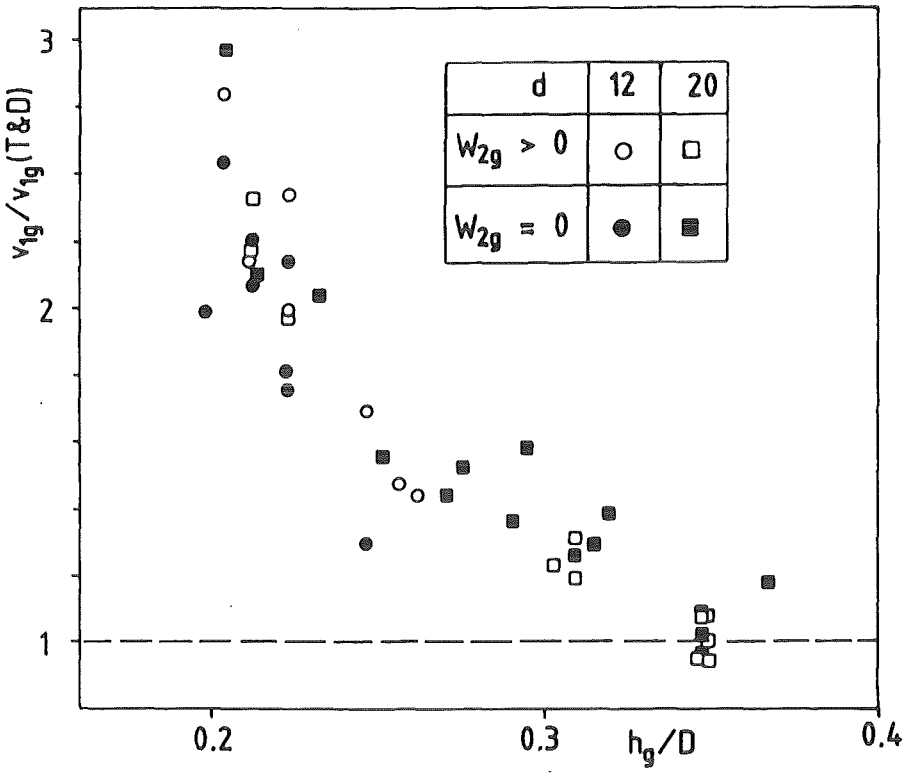

a) Ratio of measured to theoretical values from Taitel and Dukler /24, 25/

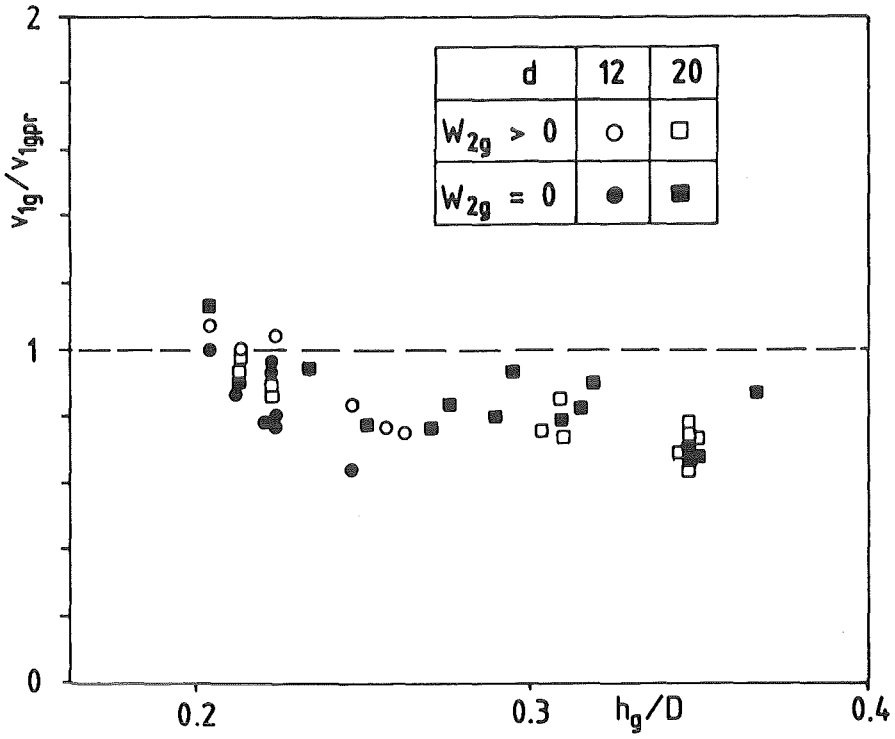

b) Ratio of measured to predicted values

Fig. 18: Transition from stratified to slug flow

Wallis and Dobson /26/ deduced a relationship for the onset of slugging in rectangular ducts which can be written as follows:

$$v_g \geq 0.5 \left[\frac{(\rho_l - \rho_g) g h_g}{\rho_g} \right]^{0.5} \qquad (2)$$

where 0.5 is an experimental coefficient.

The authors attribute the discrepancy of this coefficient with the greater value predicted by the classical theory of the Kelvin Helmholtz instability, to the fact that it is an essentially one-dimensional theory. They argue that two-dimensional flows over large waves of finite wavelength, give rise to larger dynamic forces than those predicted by the simple theory.

If the factor h_g/D in Eq. (1) is replaced by the coefficient 0.5 proposed by Wallis and Dobson, the transition is described as follows:

$$v_g \geq 0.5 \left[\frac{(\rho_l - \rho_g) g A_g}{\rho_g A'_l} \right]^{0.5} \qquad (3)$$

which indicates that v_g depends on h_g, only through the ratio A_g/A'_1, or in other words, the transition is dominated by the gas phase velocity and not by the gap of gas.

Using Eq. (3) again the ratio of measured to predicted values of v_g was plotted as a function of h_g/D as shown in Fig. 18b.

The agreement with the model is fairly good, even if the measured values are about 20 % lower than the predicted ones, which may be partly due to a different criterion employed to determine the onset of the transition. It is interesting that the experimental data were not remarkably influenced by the way the gas was leaving the test section, i.e. through valve $V2_g$ or through the branch. This indicates that the transition is not governed by the local upward acceleration of the gas in the vicinity of the branch entrance but rather by the gas moving in the direction of the waves and favoring the increase of the waves amplitude.

5. Beginning of Gas and Liquid Entrainment

5.1 Dimensional Analysis

To describe the beginning of gas or liquid entrainment, a general case is illustrated in Fig. 19 where again the labels 1, 2, 3 are used to distinguish between inflow, outflow and branch-flow, respectively.

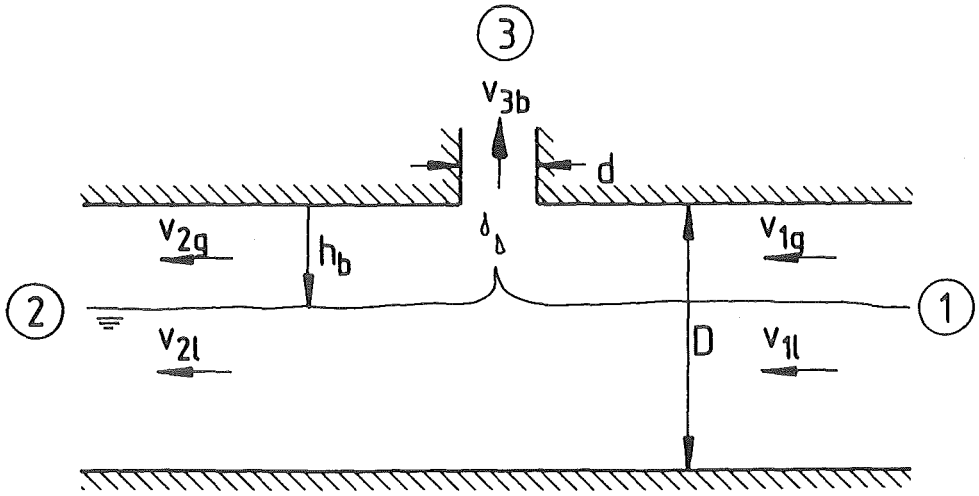

Fig. 19: General variables to determine the beginning of entrainment.

If the effects of viscosity and surface tension are neglected, the significant variables for the determination of the beginning of entrainment (b.e.) can be classified as follows:

Geometrical parameters:

h_b = distance from the branch entrance to the interface at the beginning of entrainment

d = diameter of the branch

D = diameter of the main pipe

Kinematic quantities:

v_{2g} = gas velocity in the outflow

v_{2l} = liquid velocity in the outflow

v_{3b} = velocity of the continuous phase at beginning of entrainment

Fluids properties:

ρ_b = density of the continuous phase at beginning of entrainment

$\rho_l - \rho_g$ = difference between liquid and gas densities

External forces:

g = acceleration of gravity.

By combination of these variables, the following dimensionless groups are chosen to describe the beginning of entrainment:

$$\frac{h_b}{d}\ ,\quad \frac{\rho_b\, v_{3b}^2}{g\, d\,(\rho_l-\rho_g)}\ ,\quad \frac{\rho_g\, v_{2g}^2}{\rho_b\, v_{3b}^2}\ ,\quad \frac{\rho_l\, v_{2l}^2}{\rho_b\, v_{3b}^2}\ ,\quad \frac{d}{D}$$

The first group is the most important geometrical parameter since it represents the influence of the break size on the beginning of entrainment; the second constitutes the ratio of inertial to gravitational forces in the branch flow (Froude number Fr); the following two terms are ratios between momentum-fluxes and constitute a relative magnitude of the superimposed velocities; the last group is a geometrical parameter indicating the relative size of the break.

The magnitude of the various dimensionless numbers for the present experiments with different branch flow configurations, are summarized in Table 2 which also indicates whether a vortex or a vortex-free flow was observed in the continuous phase.

	vortex flow	vortex free	vortex flow	vortex flow	vortex flow
$\frac{h_b}{d}$	2.8 - 12	1.5 - 5.5	2.5 - 7	0.4 - 3.8	0.5 - 3.2
$\frac{v_{3b}^2\ \rho_b}{gd(\rho_1-\rho_g)}$	$1 - 5\times10^3$	$2\times10^2-5\times10^3$	4 - 50	$2 - 1.8\times10^3$	$4 - 4.8\times10^3$
$\frac{\rho_g\ v_{2g}^2}{\rho_b\ v_{3b}^2}$	$0 - 10^{-5}$	$0 - 10^{-5}$	$0 - 1.5\times10^{-4}$	$0 - 3\times10^{-3}$	$0 - 10^{-3}$
$\frac{\rho_1\ v_{21}^2}{\rho_b\ v_{3b}^2}$	$0 - 10^{-6}$	$0;\ 10^{-6}-10^{-4}$	$0 - 1.6\times10^{-4}$	$0-1.7\times10^{-3}$	$0 - 3\times10^{-3}$
$\frac{d}{D}$	$<10^{-1}$	$<10^{-1}$	$<10^{-1}$	$<10^{-1}$	$<10^{-1}$

Table 2: Range of values adopted by the dimensionless groups chosen to describe the beginning of entrainment.

For downward branches the data corresponding to b.g.e. with superimposed liquid velocities were taken from previous results /17, 18/. In those experiments (see section 3.2) a small gas flow rate was used to keep the system pressure constant; this is indicated by the range $0-10^{-5}$ assigned to the group $\rho_g\, v_{2g}^2/\rho_b v_{3b}^2$.

In agreement with the description in Section 4.1 a vortex free flow in downward branches occurred only with $\rho_l v^2_{21}/\rho_b v^2_{3b}$ equal to zero or greater than 10^{-6}.

Table 2 shows that, in the range of the experiments, the momentum flux in the outflow is at least three orders of magnitude lower than the momentum flux in the branch. Therefore, no significant influence is expected of the superimposed velocities on the b.e. and the groups containing v_{2g} or v_{21} may be discarded. The ratio d/D was always smaller than 0.1. This means that for the investigated branches a geometrical similitude can be assumed for the various flow fields and the b.e. can be considered to be independent of d/D. Therefore only the correlation between h_b/d and the Froude number is investigated below.[1)]

5.2 A General Correlation for the Beginning of Entrainment

On the basis of the dimensional analysis made above the following correlation is proposed to describe the b.e. in branches with arbitrary orientations:

$$F_r^{\,a} = K^* \frac{h_b}{d} \qquad \text{or} \qquad \left[\frac{v_{3b}^2\, \rho_b}{g\, d\, (\rho_l - \rho_g)}\right]^a = K^* \frac{h_b}{d} \tag{4}$$

where a and K^* are constants to be determined from the experiments.

With $v_{3b} = v_{31}$ and $\rho_b = \rho_l$, Eq. (4) is identical to the correlation used in /17, 18/ to describe the b.g.e. in downward branches. The authors fitted their experimental data with a = 0.2 and proposed to substitute v_{3b} in the Froude number by the form $W_{3b}/\rho_b \pi d^2/4$ to get the following correlation which does not depend explicitly of d:

$$\frac{h_b\left[g\rho_b(\rho_l-\rho_g)\right]^{0.2}}{W_{3b}^{0.4}} = K \tag{5}$$

From this result the authors concluded that for $h_b/d \gg 1$ the flow field

1) This conclusion is based on a Taylor expansion of the implicit function of all relevant dimensionless groups.

generated by the branch is equivalent to that due to a punctual sink at the branch entrance, i.e., it is dominated by the branch mass flow rate and not by the branch diameter.

This equivalence with a punctual sink was also used by Craya /12/ who described analytically the b.l.e. in a side orifice at a distance h above the interface between two liquids of densities ρ and $(\rho + \Delta\rho)$ with a correlation like (5). From considerations of equilibrium at the interface (see Appendix A2), Craya obtained:

$$\frac{\Delta\rho}{\rho_b} \, g \, \frac{h_b^5}{q^2} = \text{constant} \qquad (6)$$

where q represents the volume flow through a three-dimensional punctual sink at the orifice outlet Eq. (6) was experimentally confirmed by Gariel /13/. At b.l.e.: $q = W_{3b}/\rho_b$, therefore by replacement of the lighter liquid by gas: $\Delta\rho = (\rho_l - \rho_g)$, the correlation from Craya becomes:

$$\frac{h_b \left[g \, \rho_b \left(\rho_l - \rho_g \right) \right]^{0.2}}{W_{3b}^{0.4}} = K \qquad (7)$$

which coincides with Eq. (5).

The validity of Eq. (5) to describe the b.l.e. in upward branches is discussed below.

5.3 Theoretical Considerations for the Beginning of Liquid Entrainment in Upward Branches

5.3.1 Flow Field Generated by the Break

To determine the conditions for the b.l.e. in upward branches the flow field generated by the break was investigated by using the potential flow theory.

For stratified flow without superimposed velocities in the main pipe, the flow of the continuous phase can be described as the superposition of

- a line vortex with the axis along the branch, and
- a punctual sink at the branch entrance, bounded by a rigid wall.

The contribution of a line vortex to the velocity potential $\emptyset$ at a distance r

from the vortex axis (the branch axis) is proportional to 1/r, which gives a velocity, $\vec{V} = -\nabla\phi$, proportional to $1/r^2$ describing circular paths around the branch axis (compare e.g. Li and Lam /27/).

This velocity does not modify the pessure drop in the direction of the branch axis and, therefore, with regard to the b.l.e., without superimposed velocities, only the flow field generated by the punctual sink at the branch inlet must be considered.

Figure 20 represents a punctual sink coinciding with the origin of cartesian coordinates (x, y, z) at the branch inlet. Some streamlines are drawn to represent qualitatively the flow field corresponding to a sink bounded by a rigid plane at z = 0 and a wall represented by the ideally horizontal interface at z = -h.

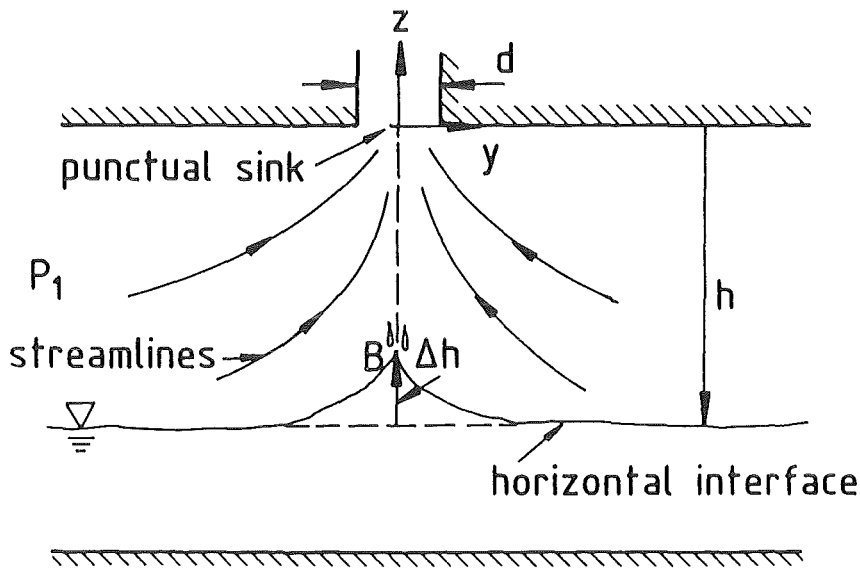

Fig. 20: Flow field generated by a punctual sink at the branch entrance.

The gas accelerated towards the sink produces a pressure drop above the liquid (Bernoulli effect) and consequently the interface is locally raised to satisfy the hydrostatic condition: Pressure and density are constant along a horizontal surface of the fluid, thus:

$$P_B + g\rho_\ell \Delta h = P_1 \qquad (8)$$

where P_B is the local static pressure at the top B of the deflected interface

and h is the corresponding height of liquid above the horizontal interface (see Fig. 20). Fluctuations of the flow field produce droplets detached from the top of the deflected interface as observed in the experiments (see Section 4.2). The b.l.e. occurs when the upward force produced by the pressure drop overcomes the gravitational force acting on the droplets. The upward force is a function of the z-component of the gas velocity which increases when the gas approaches the z-axis, as indicated by the corresponding increasing slope of the streamlines. Therefore, the droplets above the deflected interface and in the vicinity of the z-axis, will be the first to reach the branch entrance. In this region the streamlines can be assumed to be entirely radial, i.e. the influence of the interface on the velocity field, can be disregarded.

5.3.2 Determination of the Beginning of Entrainment

Figure 21 represents a punctual sink S at the origin of the spherical coordinates (R, Θ, φ), bounded by a rigid plane at $z = 0$.

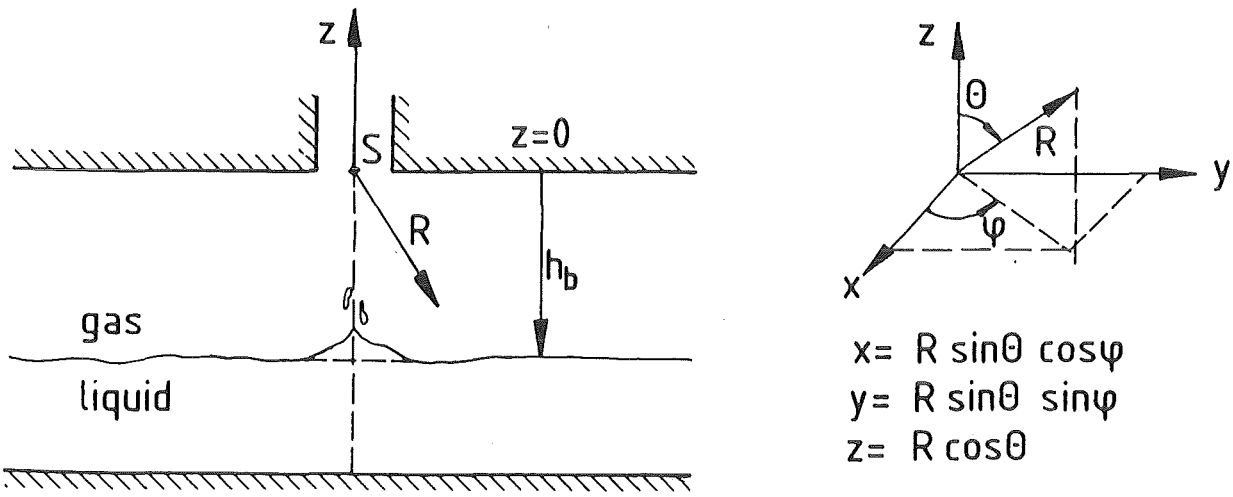

Fig. 21: Definition of the coordinates used to describe the beginning of liquid entrainment in upward branches.

The corresponding velocity potential is (see e.g. /27/):

$$\phi = -2q \,/\, 4\pi R \qquad (9)$$

where q = volume flow through the sink

R = distance from the sink.

Thus, the velocity field generated by the sink, $\vec{V} = -\nabla\phi$, is entirely radial:

$$u = -\frac{\partial\phi}{\partial R} = -\frac{2q}{4\pi R^2} \tag{10}$$

which in terms of the variables used to describe the branch flow, becomes:

$$u = -\frac{W_{3g}}{2\pi\rho_g R^2} \tag{11}$$

The condition for the b.l.e., can be written in terms of the forces acting on a droplet detached from the interface as follows:

$$F_p + F_g = 0 \tag{12}$$

where F_p is the force due to the pressure drop along the z-axis and F_g is the gravitational force.

Along the streamline represented by the z-axis the Bernoulli equation takes the form:

$$\frac{1}{2}\rho_g u^2 + P + \rho_g g z = \text{constant} \tag{13}$$

In this particular streamline the coordinate $z = R\cos\theta$ takes the value $z = R\cos\pi = -R$; therefore, the pressure distribution given by the last equation is:

$$P = -\frac{1}{2}\rho_g u^2 + \rho_g g R + \text{constant} \tag{14}$$

By differentiation, assuming ρ_g constant in the test section, it results:

$$\frac{dP}{dR} = -\rho_g u \frac{du}{dR} + \rho_g g \tag{15}$$

and with the value of u given by Eq. (11)

$$\frac{dP}{dR} = \frac{W_{3g}}{2\pi^2\rho_g R^5} + \rho_g g \tag{16}$$

This is the upward force per unit volume due to the Bernoulli effect, acting on a liquid drop detached from the interface at a distance R on the z-axis. At b.l.e. the distance to a drop just above the deflected interface is $R = R_b$

and the last equation takes the form:

$$F_p = \frac{W_{3g}^2}{2\pi^2 \rho_g R_b^5} + \rho_g g \tag{17}$$

The gravitational force per unit volume of liquid is given by:

$$F_g = - \rho_l g \tag{18}$$

With Eqs. (17) and (18) into Eq. (12) and after rearranging, the condition for the b.l.e. is:

$$\frac{R_b \left[g \rho_g (\rho_l - \rho_g) \right]^{0.2}}{W_{3g}^{0.4}} = \left(\frac{1}{2\pi^2} \right)^{0.2} \tag{19}$$

In experiments with upward branches, the height Δh of the cone shaped interface at b.l.e. was observed to be about 20 % of the distance h_b measured with a horizontal interface. Thus, with $R_b \simeq 0.8\ h_b$, the b.l.e. in upward branches is described by:

$$\frac{h_b \left[g \rho_g (\rho_l - \rho_g) \right]^{0.2}}{W_{3g}^{0.4}} = K \tag{20}$$

where $K = 1.25\ (1/2\pi^2)^{0.2} \simeq 0.688$

With ρ_g and W_{3g} replaced by ρ_b and W_{3b} respectively, this correlation is identical to Eq. (5) which consequently can be used to describe the beginning of entrainment in downward, horizontal and upward branches. The results in this section also confirm the hypothesis made in /17/ of equivalence between break and sink flow.

5.3.3 Influence of Superimposed Velocities

The shifting of the gas vortex entering upward branches, when a superimposed gas flow is applied, was described in section 4.2 and is schematically illustrated in Fig. 22.

If the vortex is assumed to rotate along the axis CS the observations made in Section 5.3.1 that the vortex does not contribute to the Bernoulli effect de-

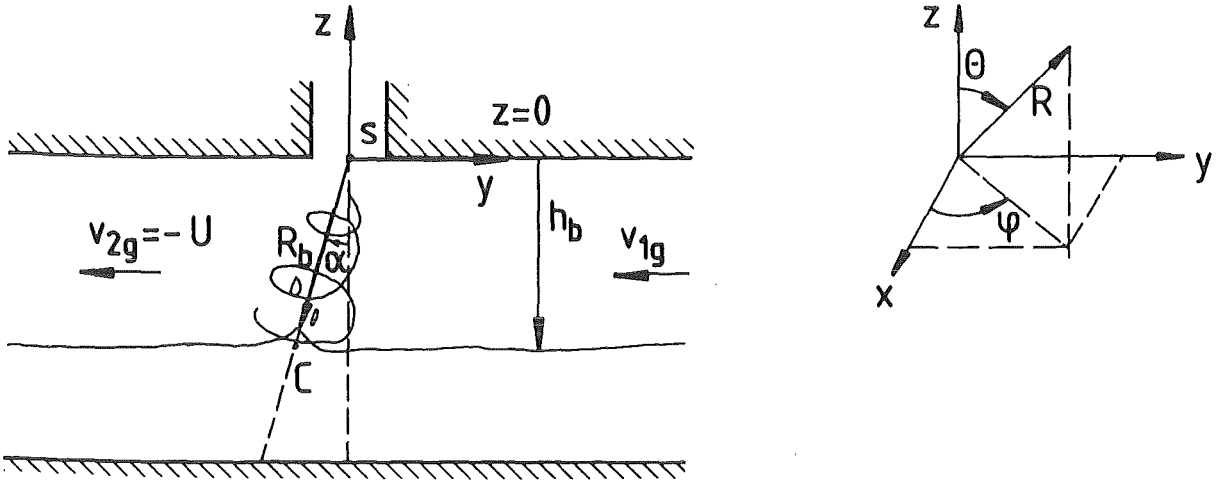

Fig. 22: Illustration of the gas vortex displacement produced by a superimposed gas flow.

termining the b.l.e., is again valid and only the uniform flow with velocity $-U$, along the y-axis, and the sink S at the intake, must be considered. The corresponding velocity potential in spherical coordinates is:

$$\phi = -\frac{2q}{4\pi R} - UR \sin\theta \sin\varphi \tag{21}$$

or, with $q = W_{3g}/\rho_g$ and $\varphi = -\frac{\pi}{2}$

$$\phi = -\frac{W_{3g}}{4\pi \rho_g R} + UR \sin\theta \tag{22}$$

Along the stream lines, the flow velocity $\vec{V} = -\nabla\phi$ has now two components but only the radial component $u = -\frac{\partial\phi}{\partial R}$ along the line CS is of interest; with $\theta = -\pi + \alpha$ it takes the value

$$u = -\frac{W_{3g}}{2\pi \rho_g R^2} + U \sin\alpha \tag{23}$$

Since the velocities toward the sink are considered to be negative, Eq. (23) shows a decrease in the radial velocity proportional to $\sin\alpha$. The corresponding decrease in the Bernoulli effect is obtained by substitution of Eq. (23) and $z = -R\cos\alpha$ into Eq. (13), which, with the procedure used in Section 5.3.2, leads to the following pressure force per unit volume in the radial direction at b.l.e.:

$$F_p = \frac{W_{3g}}{2\pi^2 \rho_g R_b^5} + \rho_g g \cos\alpha \tag{24}$$

The radial component of the gravitational force per unit volume of liquid at C is:

$$F_g = -\rho_\ell g \cos\alpha \tag{25}$$

With the two last expressions the condition for b.l.e. given by Eq. (12) becomes:

$$\frac{h_b \left[g \rho_g (\rho_\ell - \rho_g)\right]^{0.2}}{W_{3g}^{0.4}} = \left(\frac{1}{2\pi^2 \cos\alpha}\right)^{0.2} \tag{26}$$

and with $R_b \simeq 0.8\ h_b/\cos\alpha$ (see Fig. 22) the final correlation is:

$$\frac{h_b \left[g \rho_g (\rho_\ell - \rho_g)\right]^{0.2}}{W_{3g}^{0.4}} = K \tag{27}$$

where $K = 1.25\ (1/2\pi^2)^{0.2}\ (\cos\alpha)^{0.8} \simeq 0.688\ (\cos\alpha)^{0.8}$.

In agreement with the smaller h_b measured with superimposed gas flows, this result shows a diminution of the constant K with respect to the value for $v_{2g} = 0$ (Eq. (20)). This diminution is proportional to $(\cos\alpha)^{0.8}$ and, therefore, a higher reduction of K is expected with higher superimposed gas flow (higher α), as long as a stratified flow prevails. According to the description of the flow phenomena in Sec. 4.2, no change in K is expected with a superimposed liquid flow ($\alpha = 0$).

5.4 Results

For the three geometries under investigation h represents the distance from the branch entrance (branch axis) to the interface and symbol h_b is used to represent the distance h at beginning of entrainment. For the different geometries the value of K given by Eq. (5) was plotted as a function of h_b/d.

The results shown in Figs. 23-25 correspond to b.e. without superimposed velocities. The data for b.g.e. in downward branches, Fig. 23, show a good agreement with previous results from /17, 18/. Data for b.l.e. in upward branches (from /21/) are presented in Fig. 24 and data for b.l.e. and b.g.e. in horizontal branches (from /28/) are shown in Fig. 25. For the various

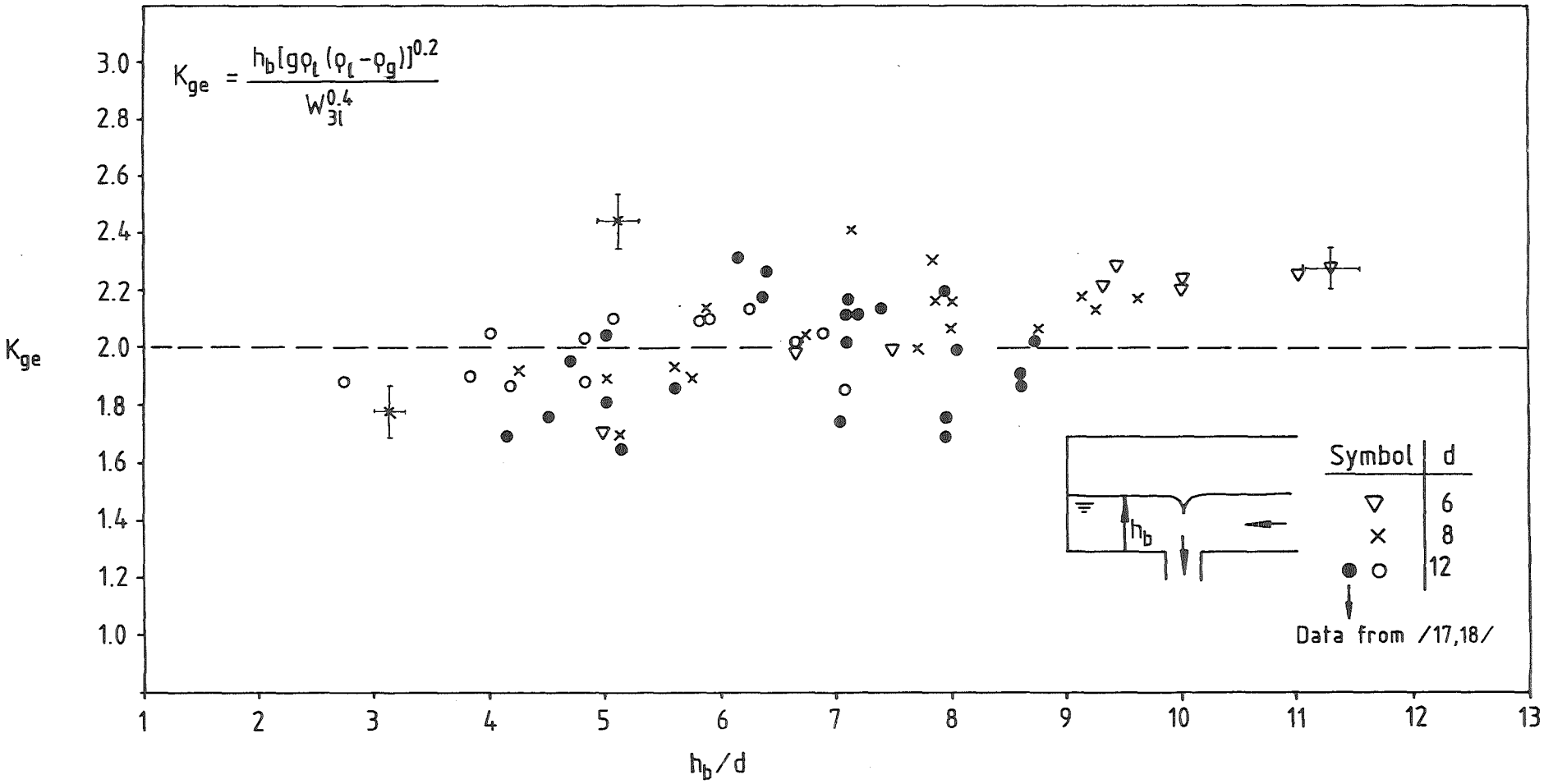

Fig. 23: Beginning of gas entrainment in downward branches.

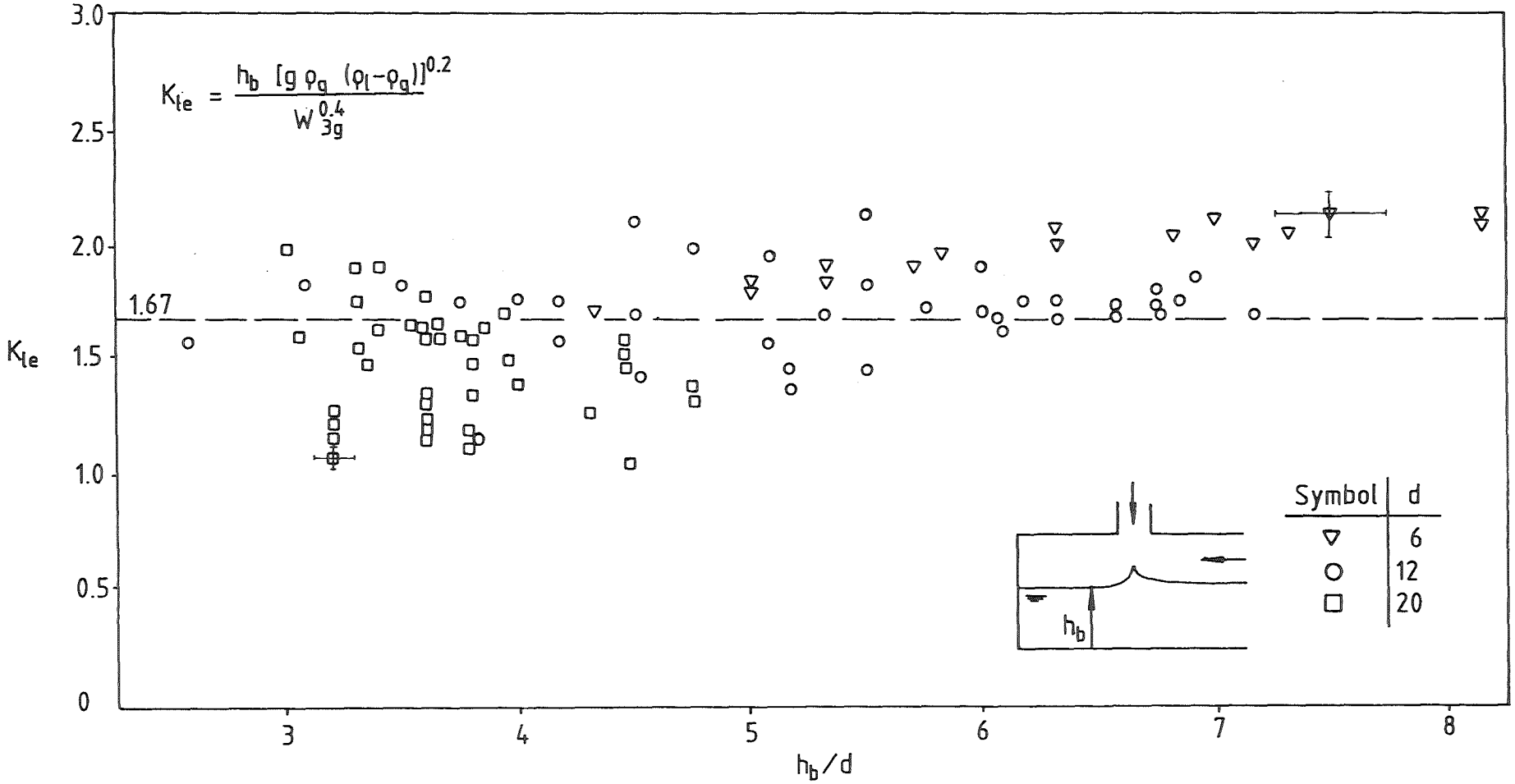

Fig. 24: Beginning of liquid entrainment in upward branches.

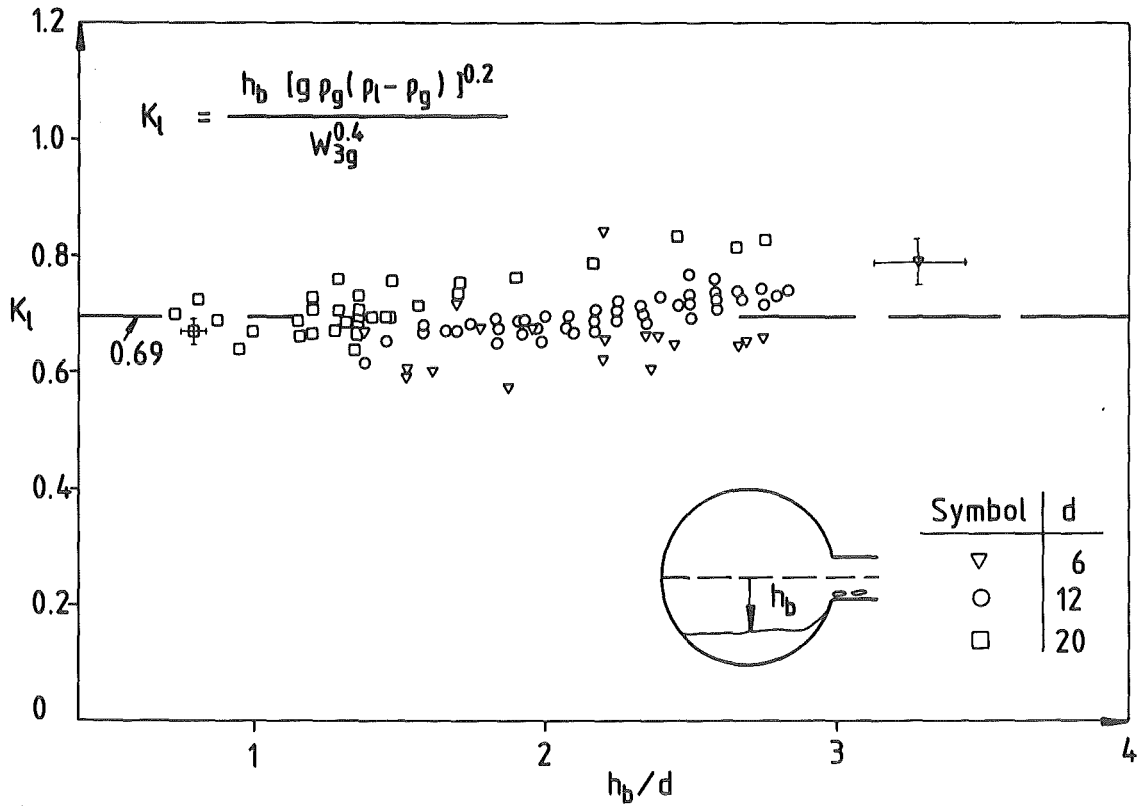

a) Beginning of liquid entrainment

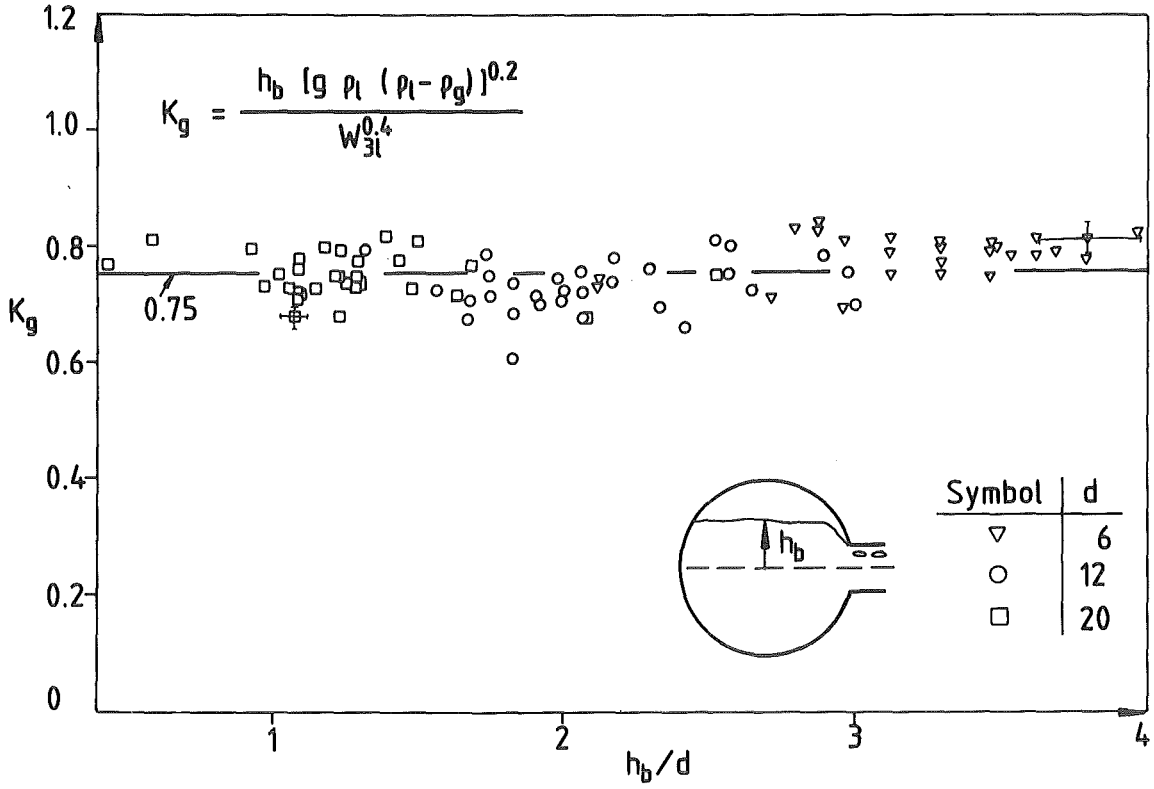

b) Beginning of gas entrainment

Fig. 25: Beginning of entrainment in horizontal branches

geometries no dependency of K on h_b/d is observed.

Eq. (5) was also used to describe the transition from vortex to vortex free flow in downward branches without superimposed velocities. Results from /17, 18/ are shown in Fig. 26 where the parameter h_{tr} represents the liquid level for the transition. Again, in a reasonable approximation, a constant value of K was obtained.

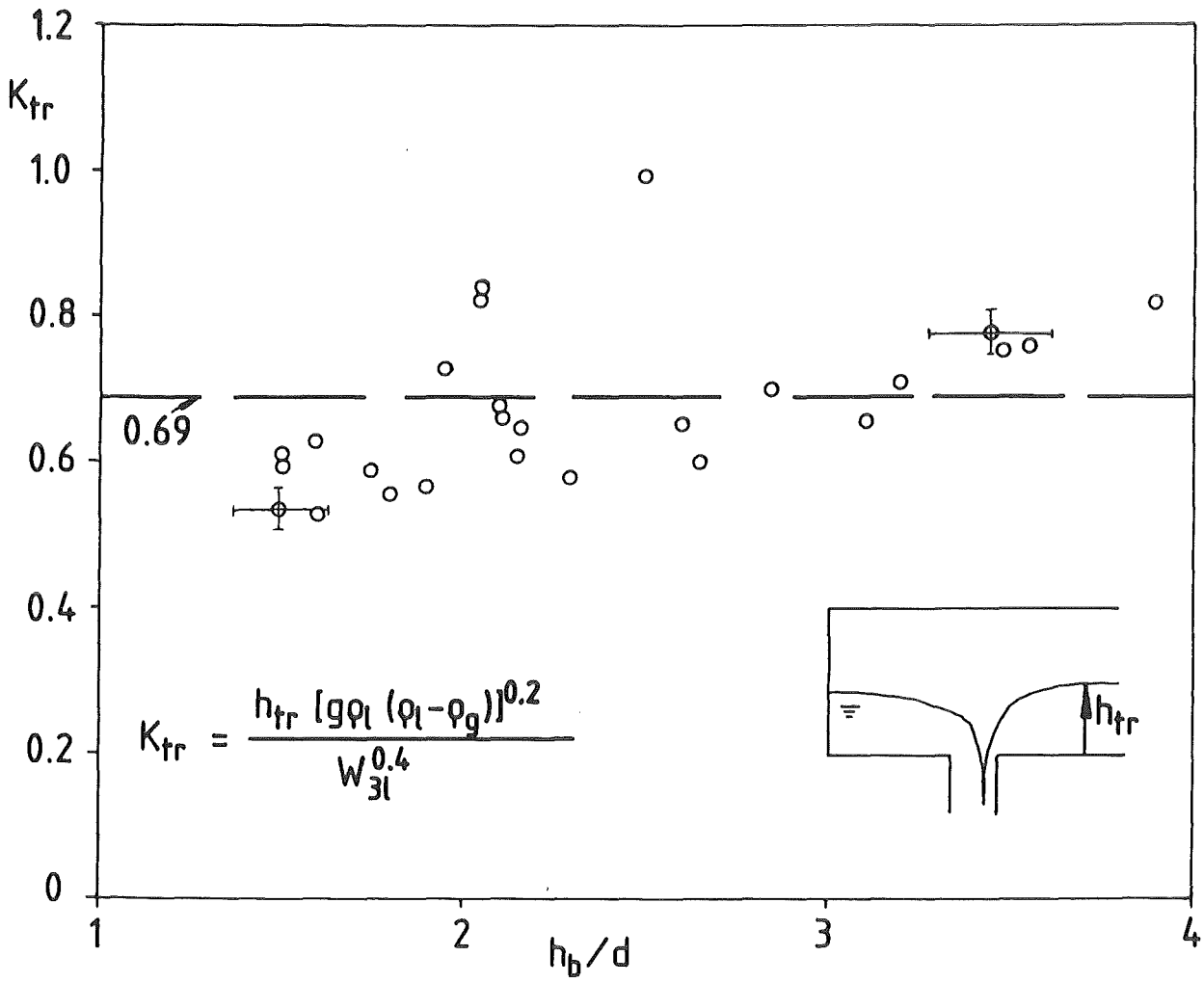

Fig. 26: Transition from vortex to vortrex free flow in downward branches; d = 12 mm, v_{21} = 0 (data from /17, 18/).

The mean values of K and the corresponding standard deviation σ of the experimental points are summarized in Table 3 below.

	Downward		Upward	Horizontal	
	b.g.e.	Transition	b.l.e.	b.g.e.	b.l.e.
K	2.00	0.69	1.67	0.75	0.69
σ %	13	18	16.2	5.5	5.2

Table 3: Experimental results for the constant K given by Eq. (5).

A general data scatter greater than that corresponding to inaccuracies of measurements is not surprising if the characteristics of the flow field described in Sec. 4 are considered. For downward branches (Sec. 4.1) the instability in the first hoses of gas entering the branch determine the b.g.e. at different liquid levels for identical experiments. Also a considerable indetermination in the liquid level for the transition from vortex to vortex free flow is introduced by strong vortex fluctuations in the flow toward the branch. For upward branches, the vorticity in the continuous gas and the subsequent radial dispersion of the liquid raised from the interface (Section 4.2), cause an initial random arrival of droplets at the branch entrance, which makes it difficult to decide whether the conditions for the b.l.e. have been attained or not. For horizontal branches (Section 4.3) the fluctuations at b.g.e. were lower than in downward branches, and the ascendent water film determining the b.l.e. was not affected by the vorticity of the gas. Therefore, a data scatter smaller than for the previous geometries was obtained.

To investigate the influence of superimposed velocities on the b.e. data from experiments performed with $v_{2g} > 0$ and $v_{21} > 0$ were used to plot K as a function of the dimensionless ratios of momentum flux $\rho_g v_{2g}^2/\rho_b v_{3b}^2$ and $\rho_1 v^2{}_{21}/\rho_b v_{3b}^2$, respectively.

Results from /17, 18/, corresponding to b.g.e. in downward branches with $v_{21} \leqslant 0.36$ m/s, are shown in Fig. 27. The transition from vortex to vortex-free flow described in Section 4.1 (Fig. 10), is very unstable and occurs for relatively small values of v_{21}. For higher superimposed liquid velocities the vortex free flow is stable and the constant value K = 1.17 was obtained to describe the b.g.e.

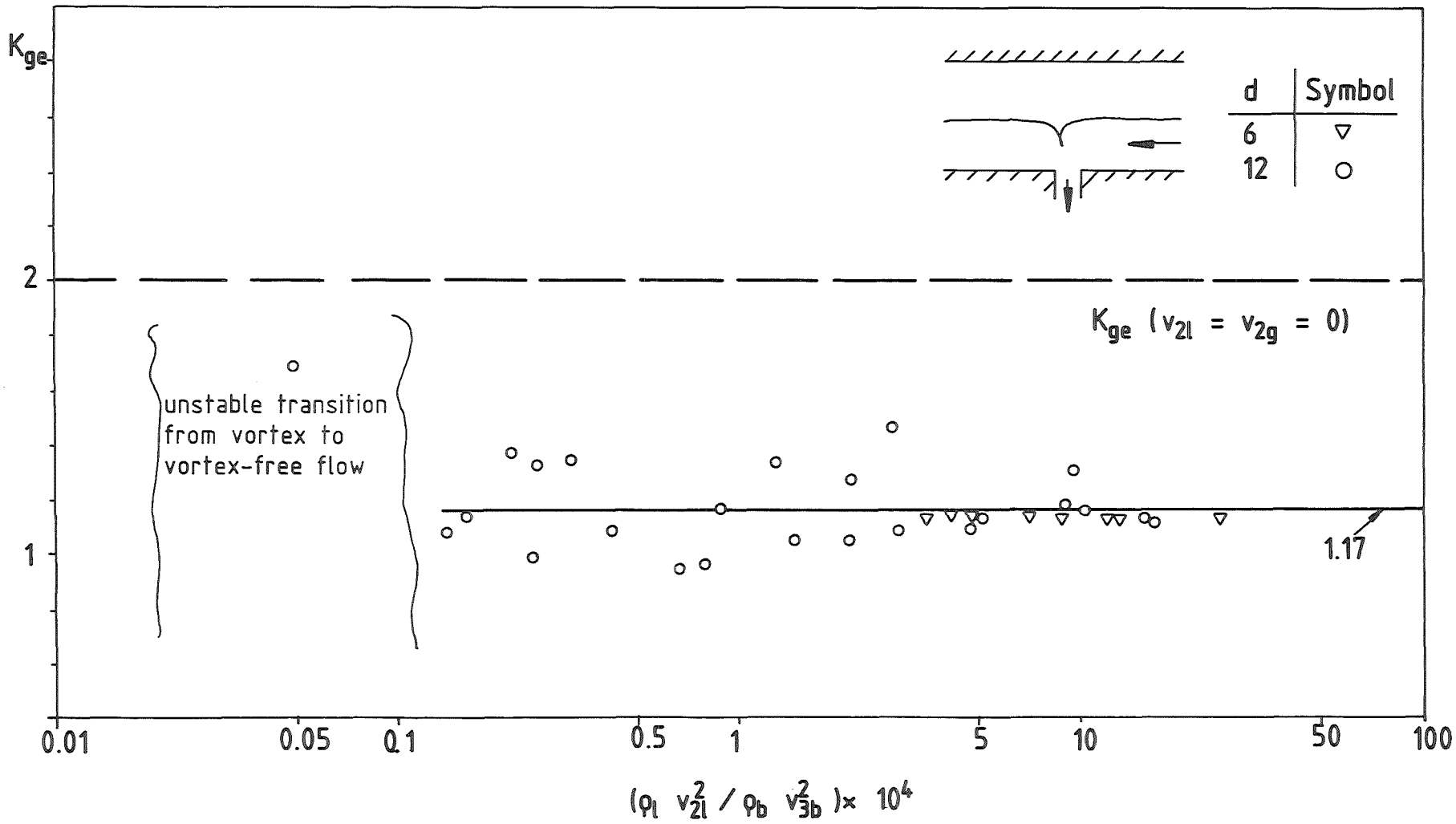

Fig. 27: Beginning of gas entrainment in downward branches with superimposed liquid velocities: $v_{21} \leq 0.36$ m/s (data from /17, 18/).

Results corresponding to b.l.e. in upward branches with $v_{2g} \leq 2.1$ m/s and $v_{21} \leq 0.12$ m/s, are presented in Fig. 28. The gas flow entering the branch was always dominated by vorticity and, in agreement with the analysis in Section 5.3.3, the value of K in Fig. 28a is observed to decrease for increasing v_{2g}. Due to the limitation in the maximum value of v_{2g} imposed by the transition to slug flow (see Section 4.2), a vortex free flow cannot be reached.

As expected, no change in K is observed for varying v_{21} (see Fig. 28b). For both flow configurations the present results are in good agreement with previous data from /29/.

The results for horizontal branches are presented in Figs. 29-30. In these experiments the ratios of momentum fluxes were one order of magnitude greater than the corresponding values for upward branches.

The curves in Fig. 29 correspond to b.l.e. with $v_{2g} \leqslant 1.6$ m/s and $v_{21} \leqslant 0.7$ m/s. The increasing value of K with increasing v_{2g} (Fig. 29a) and v_{21} (Fig. 29b) is surprising. It can be attributed to small capilary waves ($\lambda \simeq 1$ cm) on the interface. In effect, the b.l.e. will be determined by the liquid raised from the crest of the waves and therefore a higher value of the distance h_b between the branch axis and the ideally horizontal interface will be registered at b.e.

The results in Fig. 30 correspond to b.g.e. with $v_{2g} \leq 1.9$ m/s and $v_{21} \leq 0.5$ m/s. With the interface far above the branch axis, no influence of surface ripples on the b.g.e. is expected. However, with the high mass flow rates used in these experiments ($0.8 \leq W_{11}$(kg/s) ≤ 11), possible fluctuations in the liquid flow may favor the occurrence of the initial intermittent thin hoses of gas determining the b.g.e., which explains the slightly increasing value of K obtained with $v_{21} > 0$ (Fig. 30b). The experiments with $v_{2g} > 0$ were performed with $v_{11} = 0$, and therefore no change in K is observed (Fig. 30a).

The solid line curves in Figs. 28a, 29 and 30b were qualitatively drawn through the experimental points.

The results in this section show that relatively low superimposed velocities ($v_{2g} \leqslant 1$ m/s; $v_{21} \leqslant 0.1$ m/s) have a very little influence on the values of K

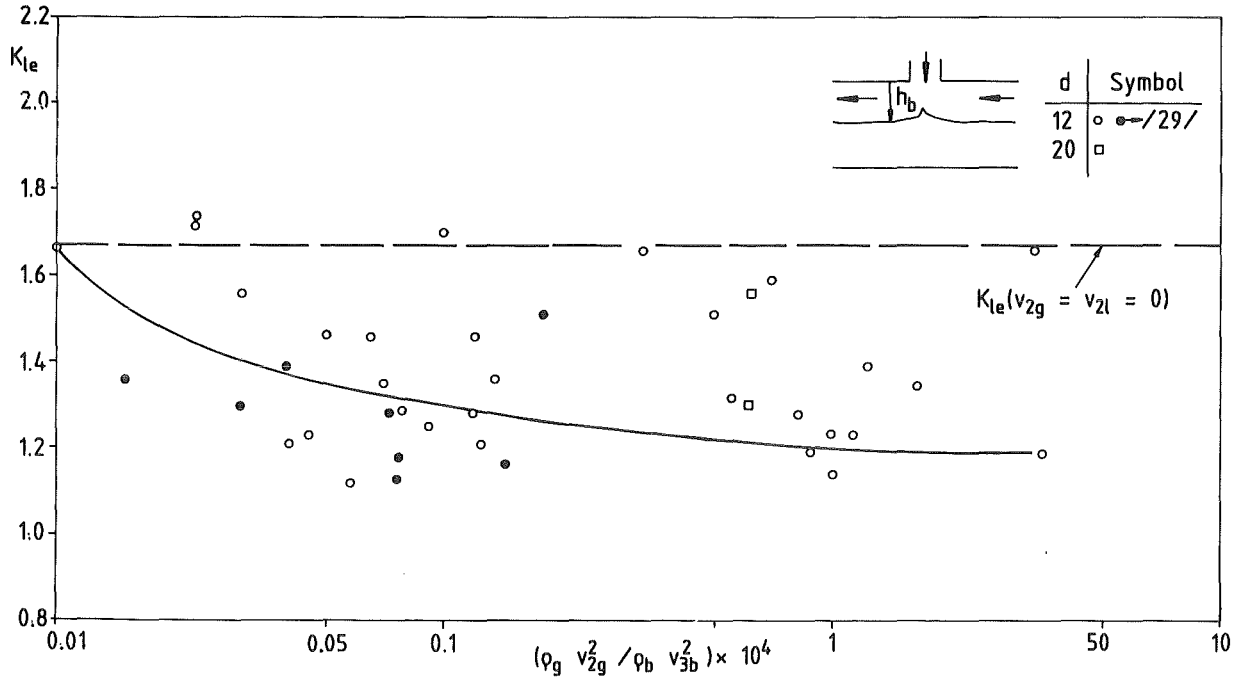

a) $v_{2g} \leq 2.1$ m/s; $v_{21} = 0$.

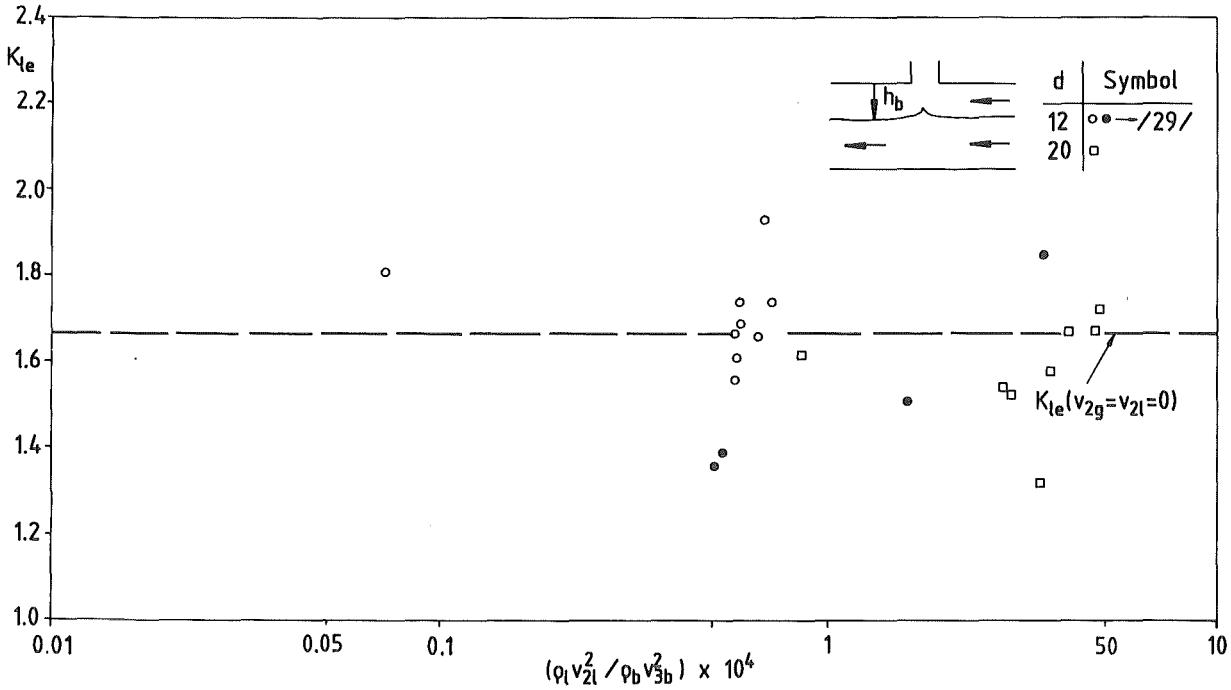

b) $v_{21} \leq 0.12$ m/s; $v_{2g} = 0$.

Fig. 28: Beginning of liquid entrainment in upward branches with superimposed velocities.

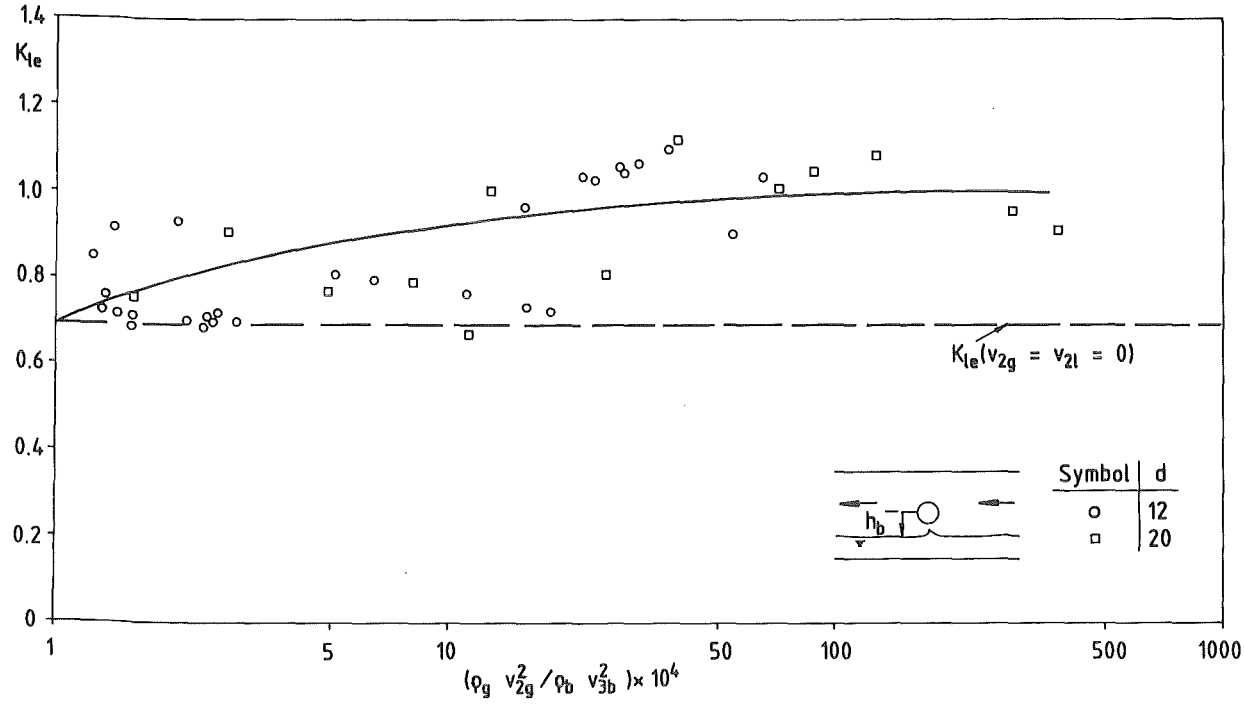

a) $v_{2g} \leq 1.6$ m/s; $v_{2l} = 0$

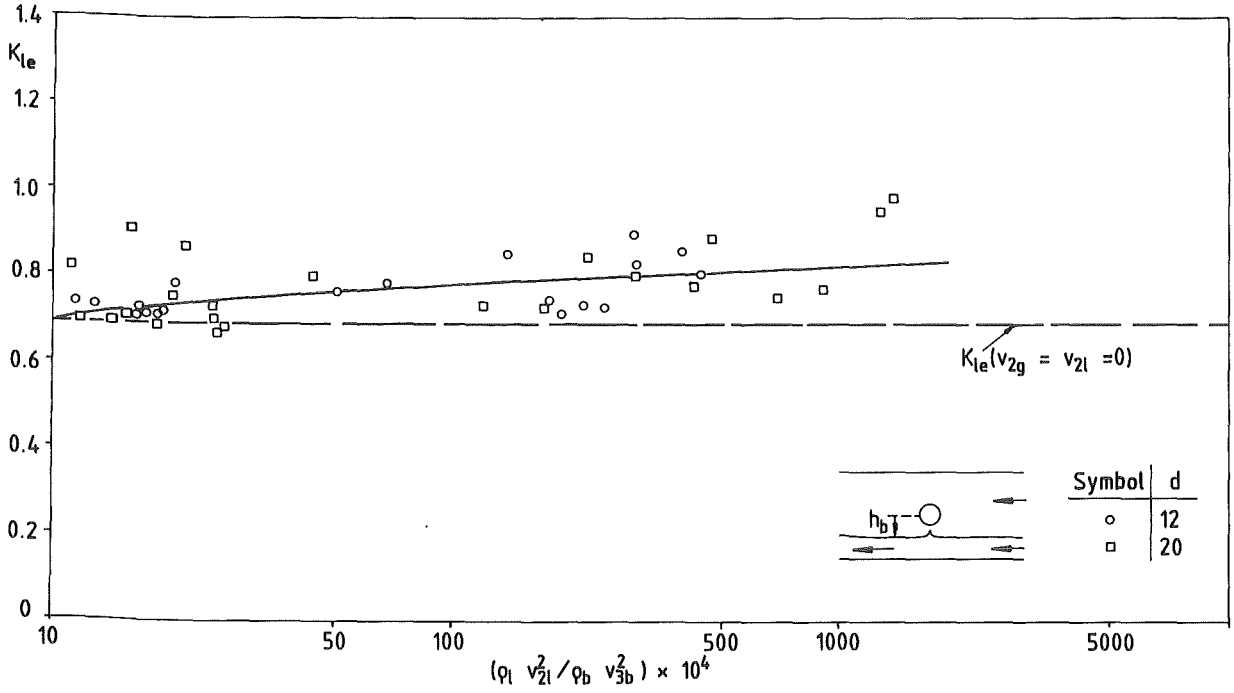

b) $v_{2l} \leq 0.7$ m/s; $v_{2g} = 0$.

Fig. 29: Beginning of liquid entrainment in horizontal branches with superimposed velocities.

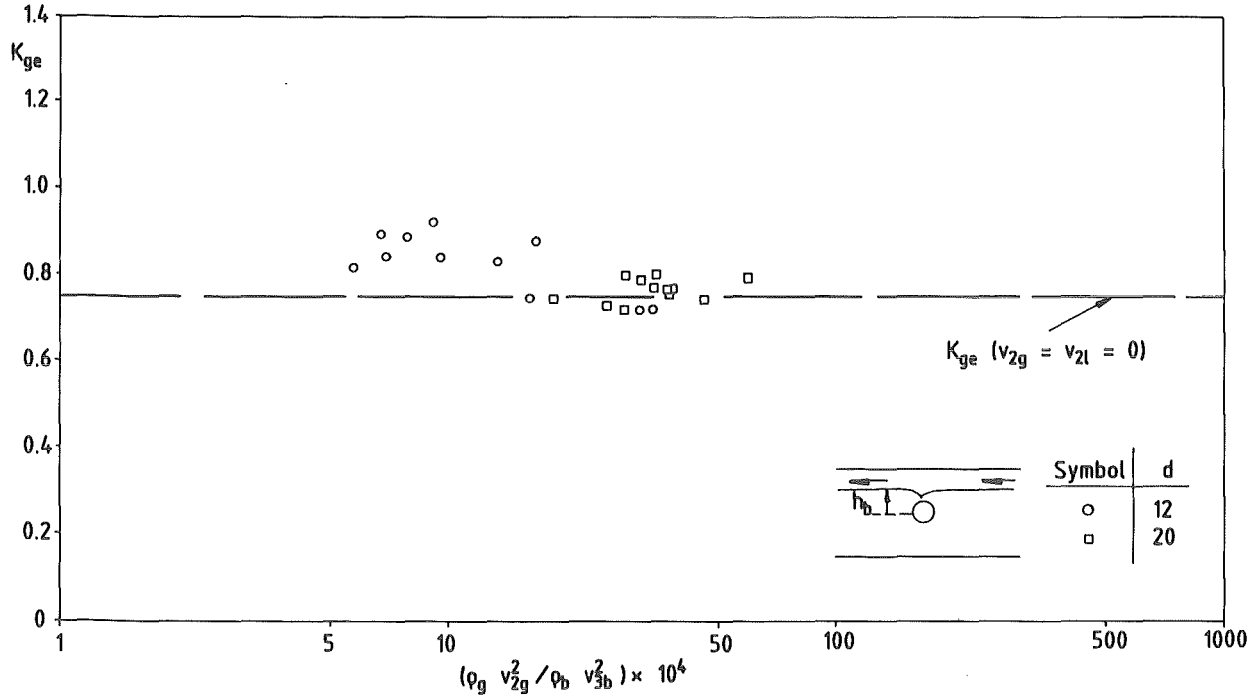

a) $v_{2g} \leq 1.9$ m/s; $v_{2l} = 0$

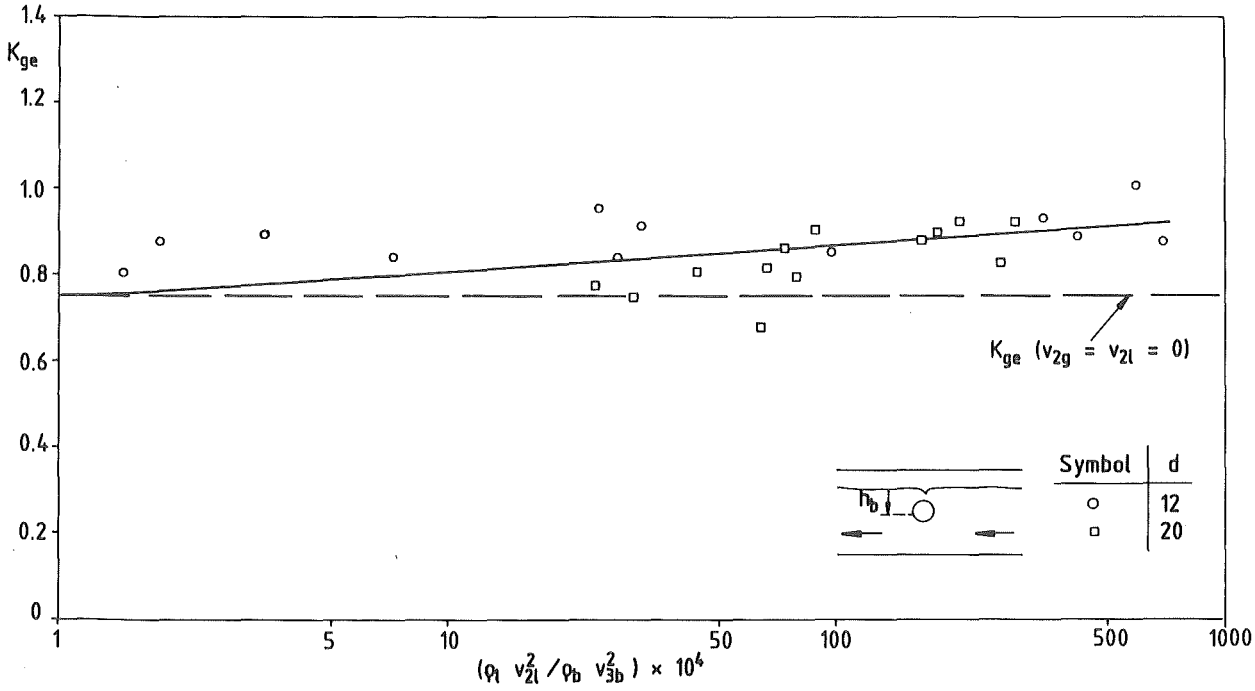

b) $v_{2l} \leq 0.5$ m/s; $v_{2g} = 0$

Fig. 30: Beginning of gas entrainment in horizontal branches with superimposed velocities

for b.e. Therefore, in experiments without superimposed velocities, for which always $v_1 << v_3$, no significant change of K can be expected if the inflow is reduced to zero. In such a case the values of K in Table 3 could be used together with Eq. (5) to determine the b.e. in small breaks at the bottom, the top or the side of large reservoirs, in which the momentum of the fluid is negligible.

6. Branch Quality and Mass Flux

6.1 Single Phase Flow

To determine the single phase branch mass flux as a function of the total pressure difference ΔP_{1-34}, the influence of the flow parallel to the main pipe is neglected and two zones in the branch flow are distinguished (Fig. 31): an acceleration zone a vena contracta develops followed by a friction zone extending up to the end of the branch.

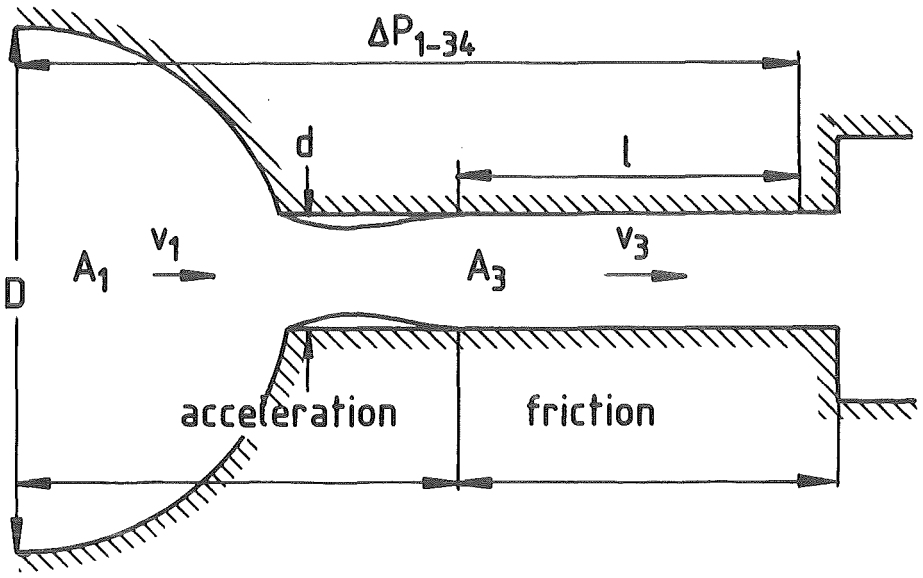

Fig. 31: Acceleration and friction zones in the branch flow.

The total pressure difference ΔP_{1-34} can be written as follows

$$\Delta P_{1-34} = \Delta P_{rev} + \Delta P_{irrev} \tag{28}$$

The term ΔP_{rev} represents the total reversible pressure drop due to the acceleration of the fluid and is given by:

$$\Delta P_{rev} = \frac{1}{2\rho}\left(G_3^2 - G_1^2\right) \tag{29}$$

For a diameter ratio $d/D \ll 1$ ($G_1 \ll G_3$) Eq. (29) reduces to:

$$\Delta P_{rev} = \frac{1}{2}\,\frac{G_3^2}{\rho} \tag{30}$$

The term ΔP_{irrev} in Eq. (28), represents the pressure loss due to the irreversible processes occurring in the acceleration and friction zones:

$$\Delta P_{irrev} = \left(K_c + \frac{4l}{d} f\right) \frac{1}{2} \frac{G_3^2}{\rho} \tag{31}$$

where K_c and f are empirical coefficients corresponding to the acceleration and frictional zones, respectively. The length l is defined in Fig. 31.

For sudden contractions with sharp edged entrance and $A_3/A_1 \rightarrow 0$, Weisbach /30/ proposes the value 0.5 for the coefficient K_c. For the friction coefficient f many correlations are available. In particular, a frequently used expression valid for $3x10^3 \leq Re \leq 3x10^6$, was given by Drew et al /31/:

$$f = 0.0014 + 0.125\ Re^{-0.32} \tag{32}$$

With the following typical values from the present experiments: l = 50 mm; d = 12 mm; Re = 7.5 x 10^4 it results: 4 lf/d $\simeq$ 0.1. Thus, Eq. (31) gives

$$\Delta P_{irrev} \simeq 0.3 \frac{G_3^2}{\rho} \tag{33}$$

By substituting Eq. (33) and Eq. (29) into Eq. (28), the total pressure difference through the branch is:

$$\Delta P_{1-34} = 0.8 \frac{G_3^2}{\rho} \tag{34}$$

which finally gives for the incompressible branch mass flux:

$$G_3 = 1.12 \sqrt{\rho\, \Delta P_{1-34}} \tag{35}$$

In practice, however, an expression of the form

$$G_3 = \zeta \sqrt{\rho\, \Delta P_{1-34}} \tag{36}$$

was used with the flow coefficient ζ determined experimentally.

Although recent experiments have revealed ζ to be a function of Reynolds number and boundary roughness (compare e.g. Streeter /32/), these influences can in practice be ignored and only a weak dependency on the geometry could be expected.

The forgoing treatment can be extended to compressible fluids by multiplying the right hand side of Eq. (36) with the expansion coefficient ε for gases, which gives:

$$G_3 = \zeta \varepsilon \sqrt{\rho \, \Delta P_{1-34}} \tag{37}$$

with ε as given in VDI 2040 /33/:

$$\varepsilon = 1 - \left[0.3707 + 0.3184\left(\frac{d}{D}\right)^2\right]\left[1 - \left(\frac{P_3}{P_1}\right)^{1/\gamma}\right]^{0.935} \tag{38}$$

where the isentropic coefficient is $\gamma = 0.4$ for air.

Eq. (37) was used to determine the flow coefficient ζ for water and subcritical air flow through branches of different diameters. The results are presented in Fig. 32 as a function of Re.

In the range covered by the experiments no significant dependency of ζ on Re can be inferred. A small difference exists between the results for air and water flows; however, a mean value valid for single phase flow was taken for each diameter, as summarizd in Table 4 below

d (mm)	6	8	12	20
ζ	0.905	0.949	0.990	0.968
σ (%)	8	17	6	16

Table 4: Subcritical single phase flow coefficient for branches of different diameters.

The different values of ζ obtained for different branch diameters can be attributed to small differences of the branch entrance geometry (roundness for instance).

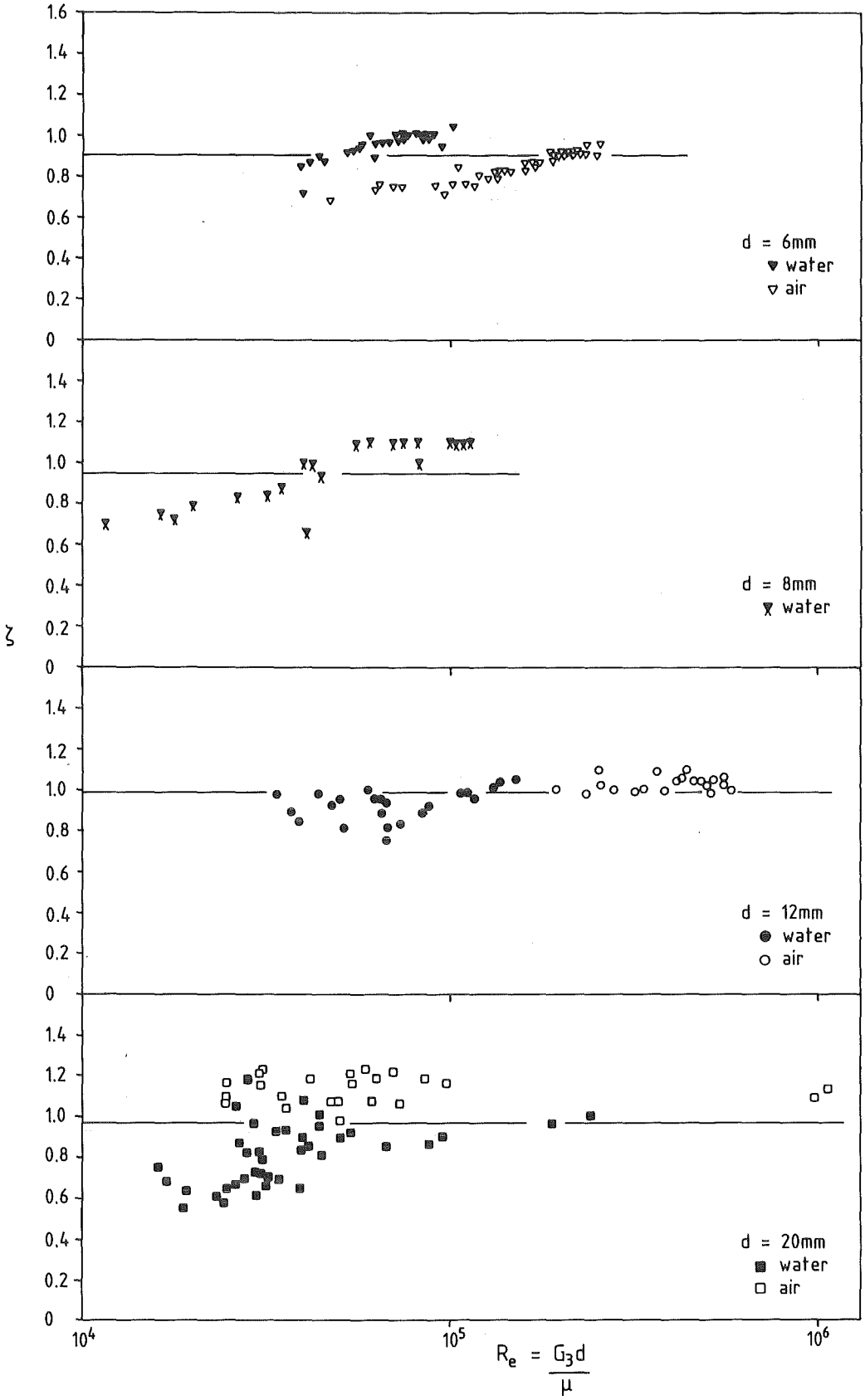

Fig. 32: Flow coefficients for single phase subcritical flow in branches with different diameters, as a function of Reynolds number.

6.2 Two Phase Flow

6.2.1 Generalized Representation of Data

To present the data for liquid or gas entrainment the procedure previously used (/17, 18/) was applied: the measured h and G_3 were normalized with h_b an G_{3b} respectively, which were calculated with the P_1 and ΔP_{1-34} measured during entrainment. Since at b.e. a single phase flow can be assumed in the branch, the parameter G_{3b} was calculated with Eq. (37) rewritten as follows:

$$G_{3b} = \zeta \varepsilon \sqrt{\rho_b \Delta P_{1-34}} \tag{39}$$

A similar expression is valid for W_{3b}:

$$W_{3b} = \zeta \varepsilon A_3 \sqrt{\rho_b \Delta P_{1-34}} \tag{40}$$

where A_3 is the branch cross-sectional area. By substitution of Eq. (40) into Eq. (5), the parameter h_b is given by:

$$h_b = \frac{K(\zeta \varepsilon A_3)^{0.4}}{g^{0.2}} \left(\frac{\Delta P_{1-34}}{\rho_\ell - \rho_g}\right)^{0.2} \tag{41}$$

6.2.2 Experimental Results

6.2.2.1 Downward Branch

For the normalized representation of data for g.e. with vortex and vortex-free flow, the parameter h_b (Eq. (41)) was calculated with the value of K for b.g.e. in the corresponding flow configuration. Thus, for entrainment with vortex flow the value K = 2 from Table 3 was used, because it corresponds to b.g.e. with vortex flow. However, for vortex free entrainment, observed when $v_{21} > 0$ or when the transition from vortex to vortex free flow with $v_{21} = 0$ has occurred, h_b was calculated with the value K = 1.17 from Fig. 27 corresponding to vortex free b.g.e.

Results including data from /17, 18/ are presented in Figs. 33-34. Various symbols are used to distinguish between experiments with and without superimposed velocities. The procedure used to fit the data in Fig. 33 is presented in Section 6.2.3.2.

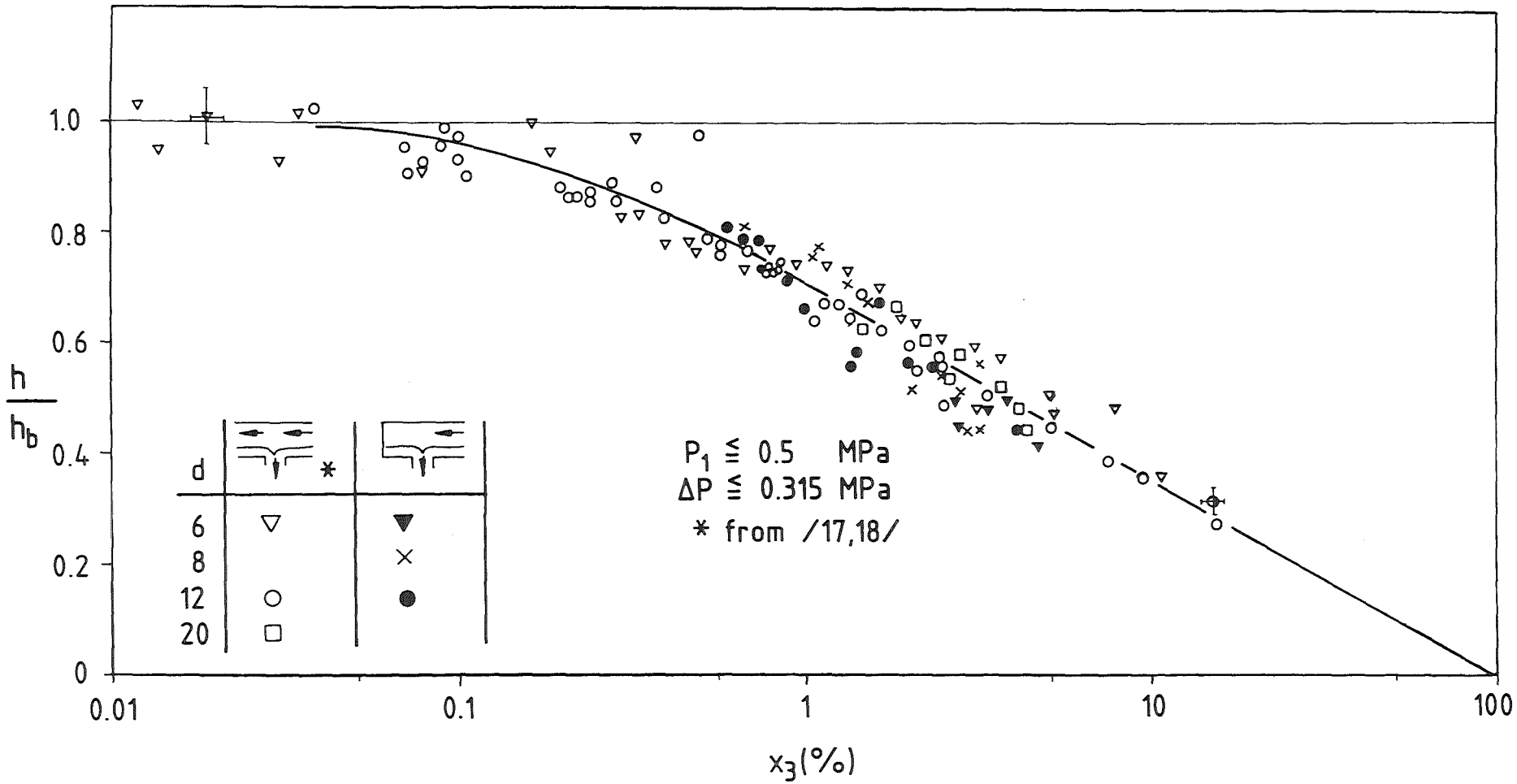

Fig. 33: Gas entrainment in downward branches: dimensionless interface level h/h_b as a function of the branch quality x_3.

The curve in Fig. 34 was qualitatively drawn through the experimental points.

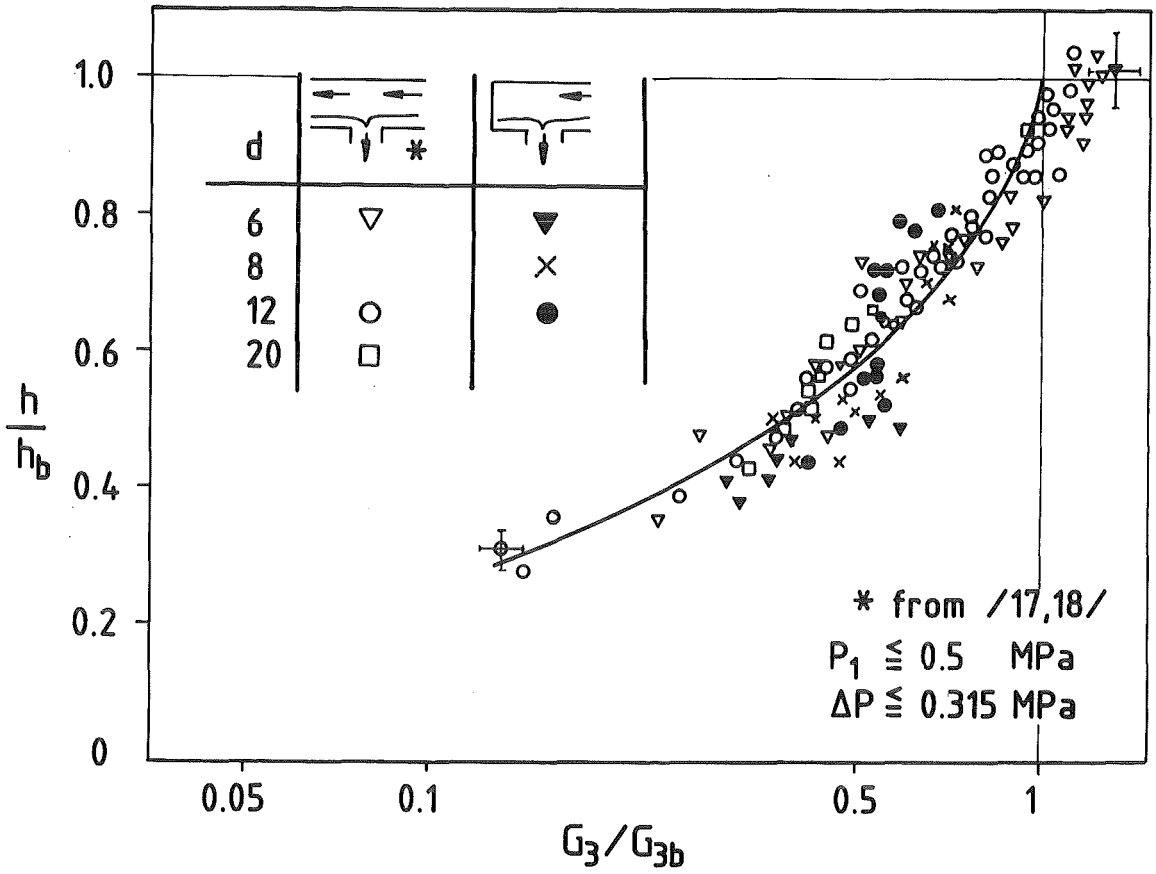

Fig. 34: Gas entrainment in downward branches: dimensionless interface level h/h_b as a function of the normalized branch mass flux G_3/G_{3b}.

6.2.2.2 Upward Branch

Figure 35 shows results for $v_{2g} = 0$ (K = 1.67). The solid line curve in Fig. 35a is a qualitative fitting of the data: Starting at $h/h_b = 1$, and for decreasing values of h/h_b, the change in x_3 is relatively small until a sudden decrease occurs at $h/h_b \simeq 0.6$ which corresponds to the transition from stratified to slug flow in the test section. The slow decrease of x_3 during stratified flow is due to the radial dispersion of droplets, produced by the strong vorticity of the gas described in Section 4.2 which avoids the water to reach the branch entrance. Qualities about 100 % determine the value $G_3/G_{3b} \simeq 1$ shown in Fig. 35b. A strong increase of G_3/G_{3b} occurs when the slug flow regime is reached.

Figure 35 contains some test points with critical branch flux for which h_b and G_{3b} were calculated with the critical pressure difference $\Delta P_{1-34} = P_1 - P_{34\ crit} \simeq 0{,}47\ P_1$; no significant influence is observed. The criterion used to draw the dashed curve in Fig. 35 a will be explained in Section 6.2.3.3.

For a typical value $x_3 = 0{,}99$ (Fig. 35 a) maximal errors of 0.27 % for x_3 and 7.4 % for G_3/G_{3b} can be expected (see Appendix A1).
A data scatter, greater than that introduced by measurement errors, is due to the fluctuations in the entrainment produced by surface waves in the various flow regimes (see Section 4.2).

According to these results for l.e. in upward branches, it may be justified to assume that only gas flows through the branch as long as a stratified flow prevails in the main pipe.

6.2.2.3 Horizontal Branch

As previously, the distance to the interface was measured from the branch axis, however, for liquid levels below this axis, h was considered to be negative; thus, points with $h > 0$ correspond to g.e. and those with $h \leq 0$ to l.e. Figure 36 shows the normalized interface level in the range $-1 \leq h/h_b \leq 1$ as a function of the measured quality. The data for different ΔP_{1-34} and branch diameters, are again well fitted by a single curve. With a logarithmic scale for the quality, the value $x_3 = 0$ is at minus infinite on the horizontal axis; however, in a good approximation, the curve is a straight line in a very wide range of qualities. The criterion used to fit the data will be explained in the next section.

Figure 37 shows the dependency of h/h_b on G_3/G_{3b}. The very different values of G_{3b} for liquid and gas entrainment (see Eq. (39)) determine the discontinuity observed at $h = 0$.

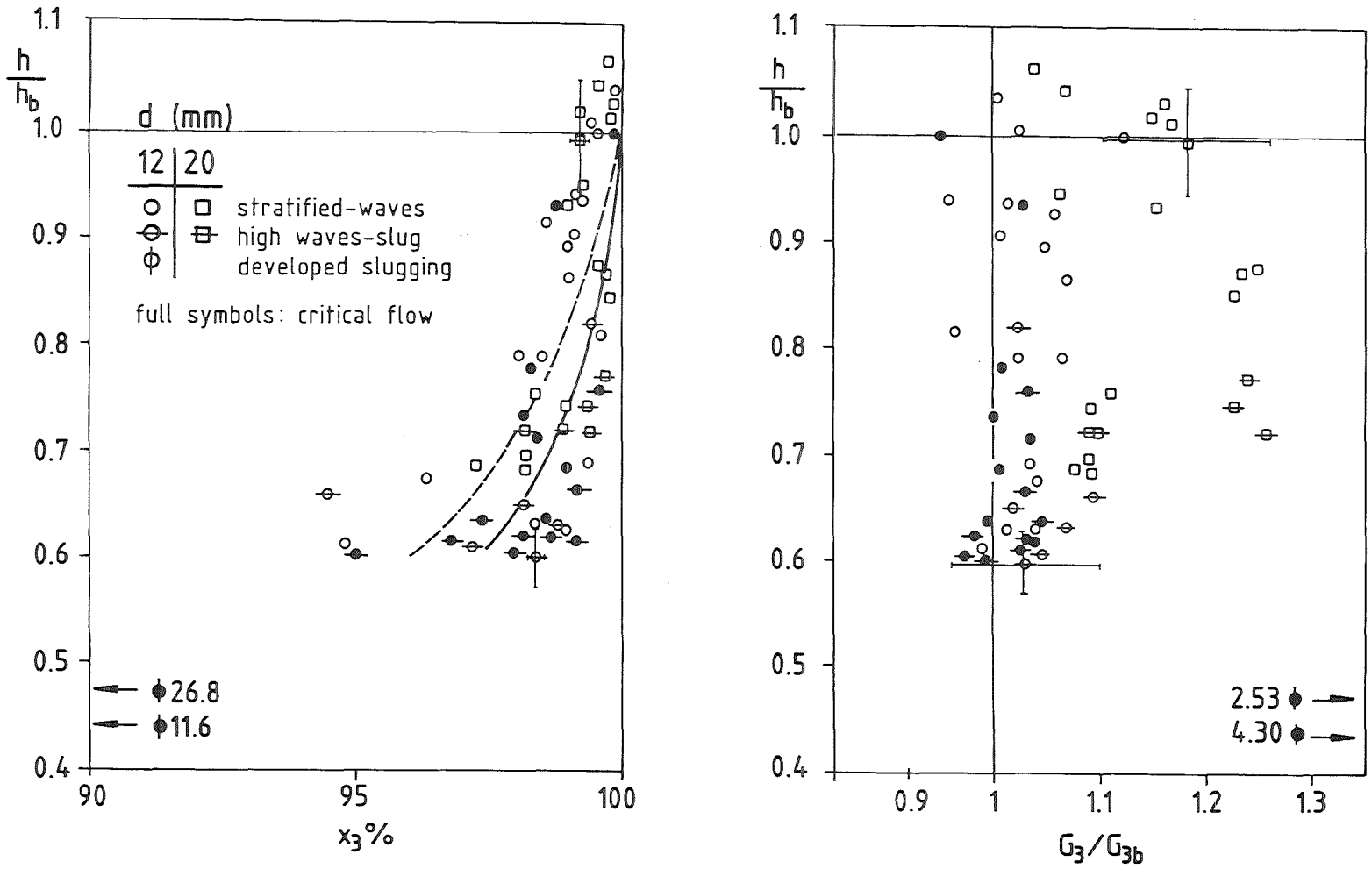

a) dimensionless interface level h/h_b as a function of the branch quality x_3

b) dimensionless interface level h/h_b as a function of the normalized branch mass flux G_3/G_{3b}

Fig. 35: Liquid entrainment in upward branches

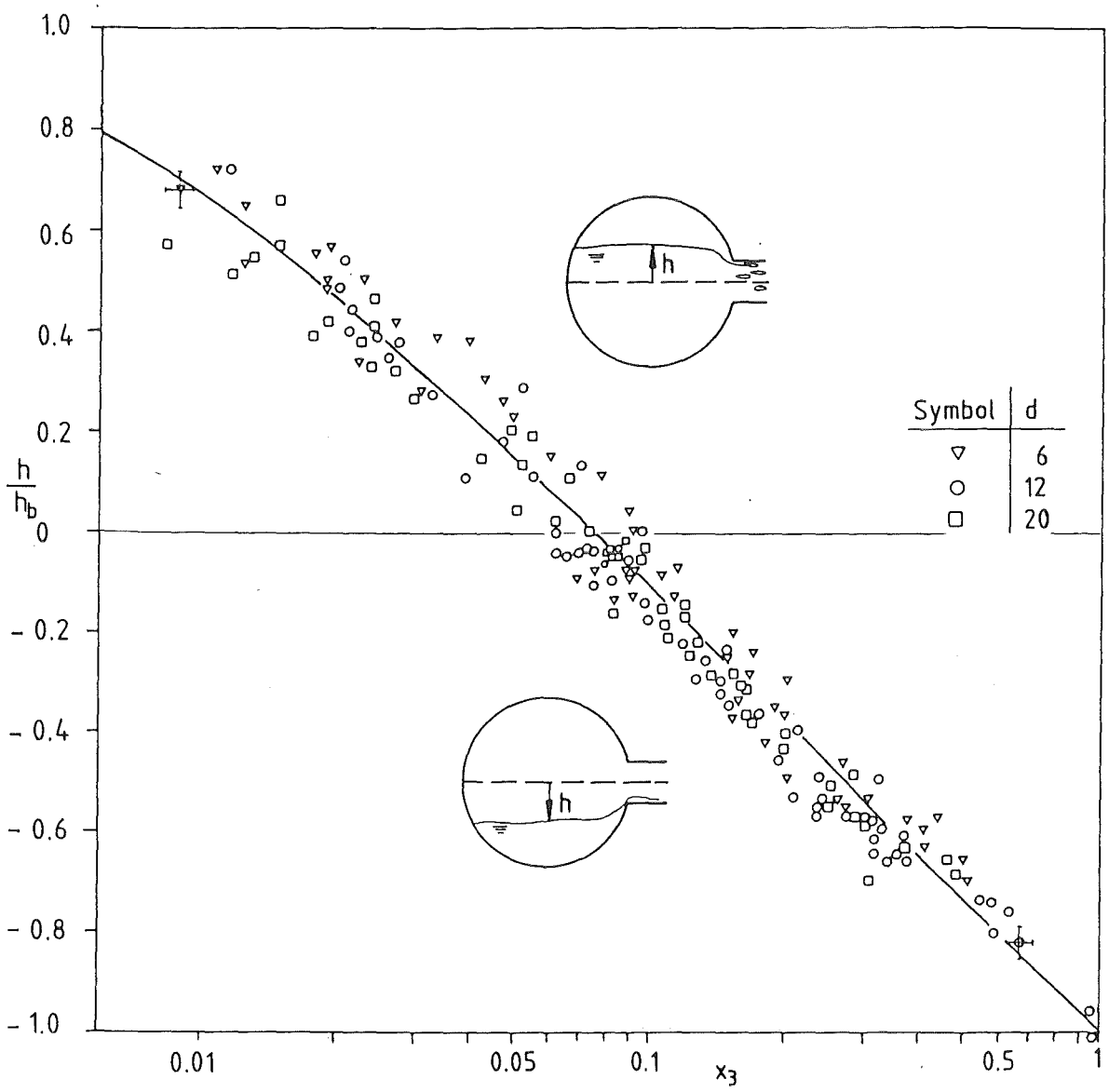

Fig. 36: Gas and liquid entrainment in horizontal branches: dimensionless interface level h/h_b as a function of the branch quality x_3.

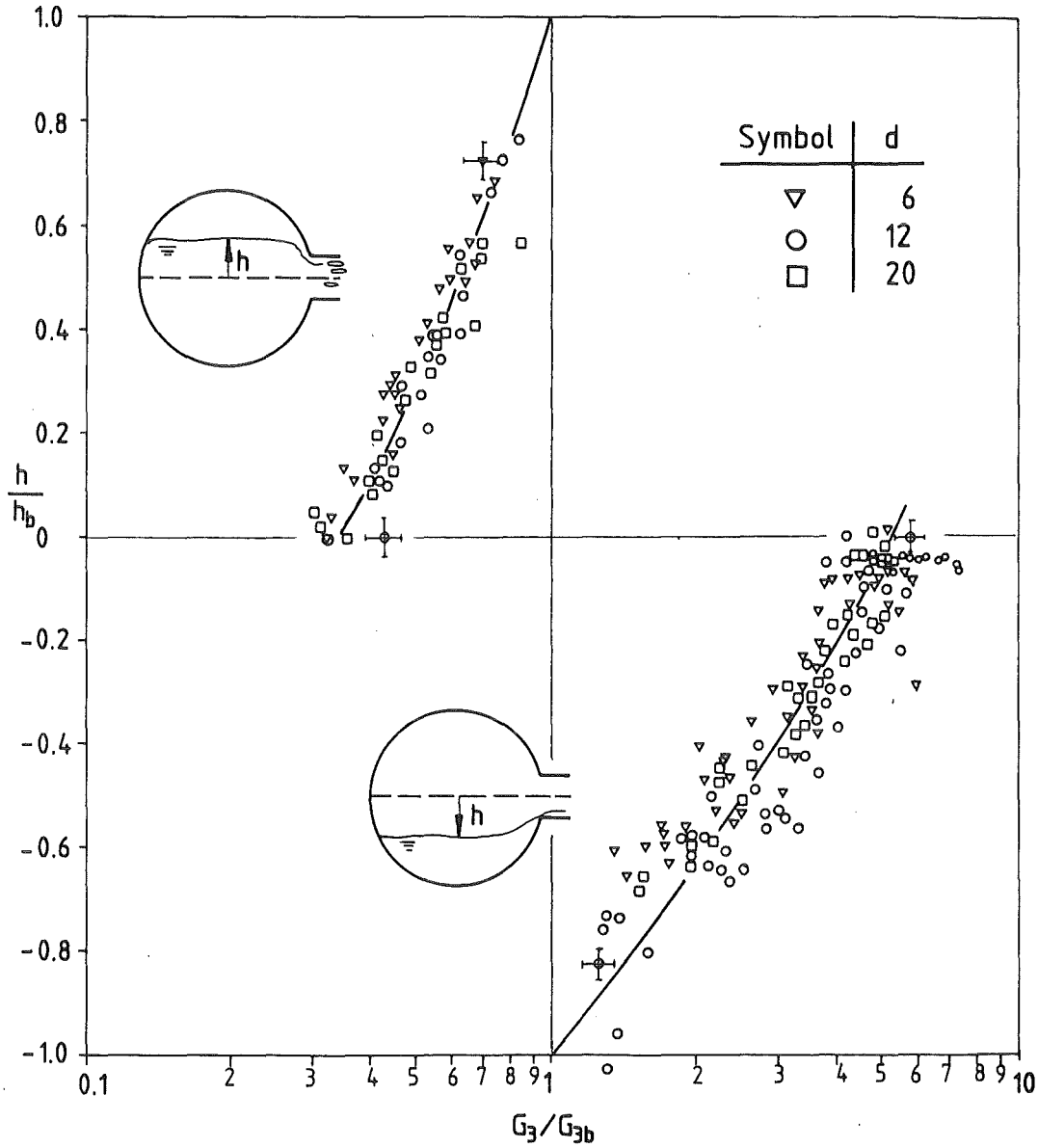

Fig. 37: Gas and liquid entrainment in horizontal branches: dimensionless interface level h/h_b as a function of the normalized branch mass flux G_3/G_{3b}.

6.2.3 Correlations for the Branch Quality

6.2.3.1 Horizontal Branch

The data for both liquid and gas entrainment were fitted with the following relationship:

$$x_3 = x_o^{\left(1+C\frac{h}{h_b}\right)}\left[1-\frac{1}{2}\frac{h}{h_b}\left(1+\frac{h}{h_b}\right)x_o^{\left(1-\frac{h}{h_b}\right)}\right]^{0.5} \qquad (42)$$

where x_o represents the quality for h = 0. To obtain this correlation, the linear dependency of h/h_b on log x_3 suggested by the results in Fig. 36 was first considered. Next, the term in brackets was introduced to give a quality tending to zero for h/h_b approaching unity. The coefficient C accounts for the change in the parameter h_b when passing from liquid to gas entrainment (see Eq. (41)). Thus, for l.e. ($h/h_b \leq 0$), C = 1 and for g.e. ($h/h_b \geq 0$), C = $h_{b.g.e.}/h_{b.l.e.}$. Using Eq. (41) with a typical value ε_{air} = 0.96 and the values of K given in Table 3, the resulting coefficient for g.e. is C = 1.09.

The value of x_o in Eq. (42) depends on the fluid densities; thus to obtain a general correlation, x_o must be expressed as a function of these variables. A simple model for x_o was developed assuming the conditions indicated in Fig. 38: the main pipe is filled with water up to the branch axis (h = 0); u_g and u_l represent the phase velocity of gas and liquid, respectively, at the branch entrance.

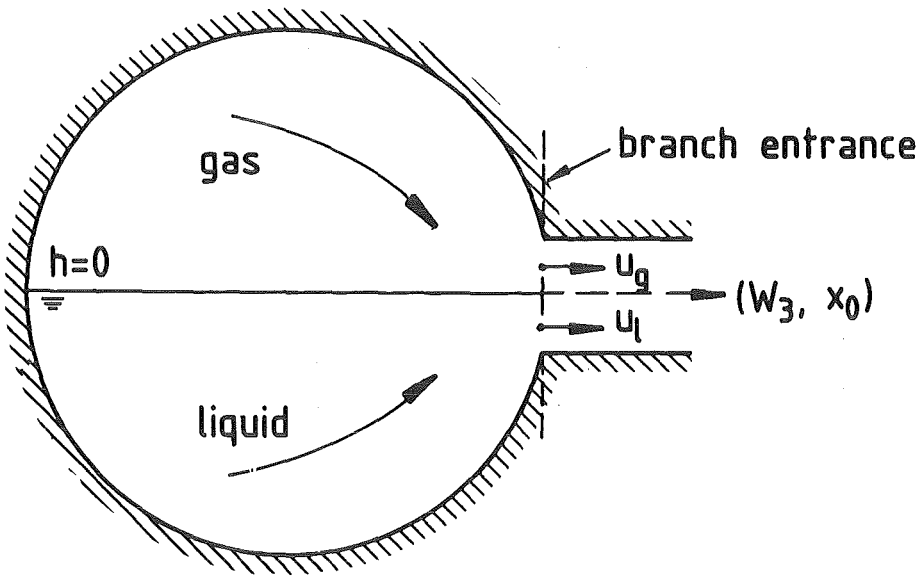

Fig. 38: Branch entrance conditions for interface level h = 0.

With the hypothesis that for h = 0 both phases have

a) the same acceleration pressure drop,

b) the same cross sectional area (α = 0.5),

the conditions at the branch entrance are given by:

$$\Delta P_{acc} = \frac{1}{2} \rho_g u_g^2 = \frac{1}{2} \rho_\ell u_\ell^2 \tag{43}$$

With α = 0.5, the phases satisfy: $\alpha \rho_g u_g = G_{3g} = W_{3g}/A_3$ and $\rho_1 u_1 = G_{31} = W_{31}/A_3$. Therefore, Eq. (43) can be rearranged to give:

$$\frac{W_{3\ell}}{W_{3g}} = \sqrt{\frac{\rho_\ell}{\rho_g}} \tag{44}$$

which, combined with the definition $x_3 = (1 + W_{31}/W_{3g})^{-1}$, gives:

$$x_o = \frac{1}{1+\sqrt{\rho_\ell/\rho_g}} \tag{45}$$

Specific experiments performed to measure x_o yielded, independently of P_1, ΔP_{1-34} and d, branch qualities about 15 % higher than the values calculated with Eq. (45). This discrepancy is not surprising if the complexity of the flow processes generated in the vicinity of the branch entrance is considered. Thus, the final correlation proposed to predict the quality ($x_{3,pr}$) in horizontal branches is:

$$x_{3pr} = \left(\frac{1.15}{1+\sqrt{\rho_\ell/\rho_g}}\right)^{\left(1+C\frac{h}{h_b}\right)} \left[1 - \frac{1}{2}\frac{h}{h_b}\left(1+\frac{h}{h_b}\right)\left(\frac{1.15}{1+\sqrt{\rho_\ell/\rho_g}}\right)^{\left(1-\frac{h}{h_b}\right)}\right]^{0.5} \tag{46}$$

where:

$$C = \begin{cases} 1 \text{ for l.e.} & (h/h_b \leq 0) \\ 1.09 \text{ for g.e} & (h/h_b > 0) \end{cases}$$

Figure 39 shows the ratio of measured to predicted quality (x_3/x_{3pr}) as a function of P_1. Data scatter around the value of one and no remarkable dependency on P_1 is observed. Figure 40 contains the same ratio as a function of h/h_b. Again a fairly symmetric distribution was obtained both for gas and liquid entrainment. The standard deviation of the data is σ = 19 %.

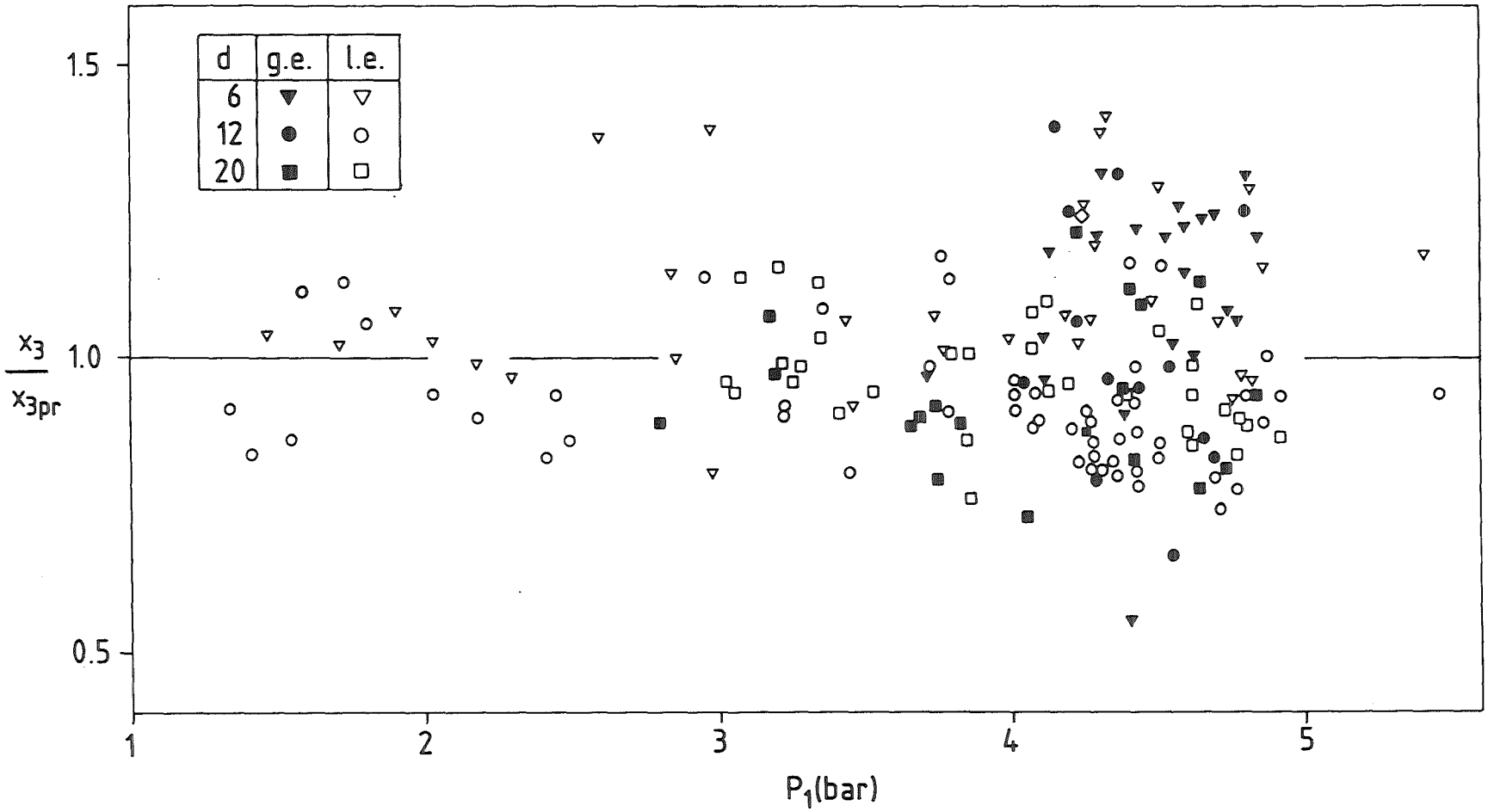

Fig. 39: Ratio of measured to predicted quality in horizontal branches as a function of system pressure P_1.

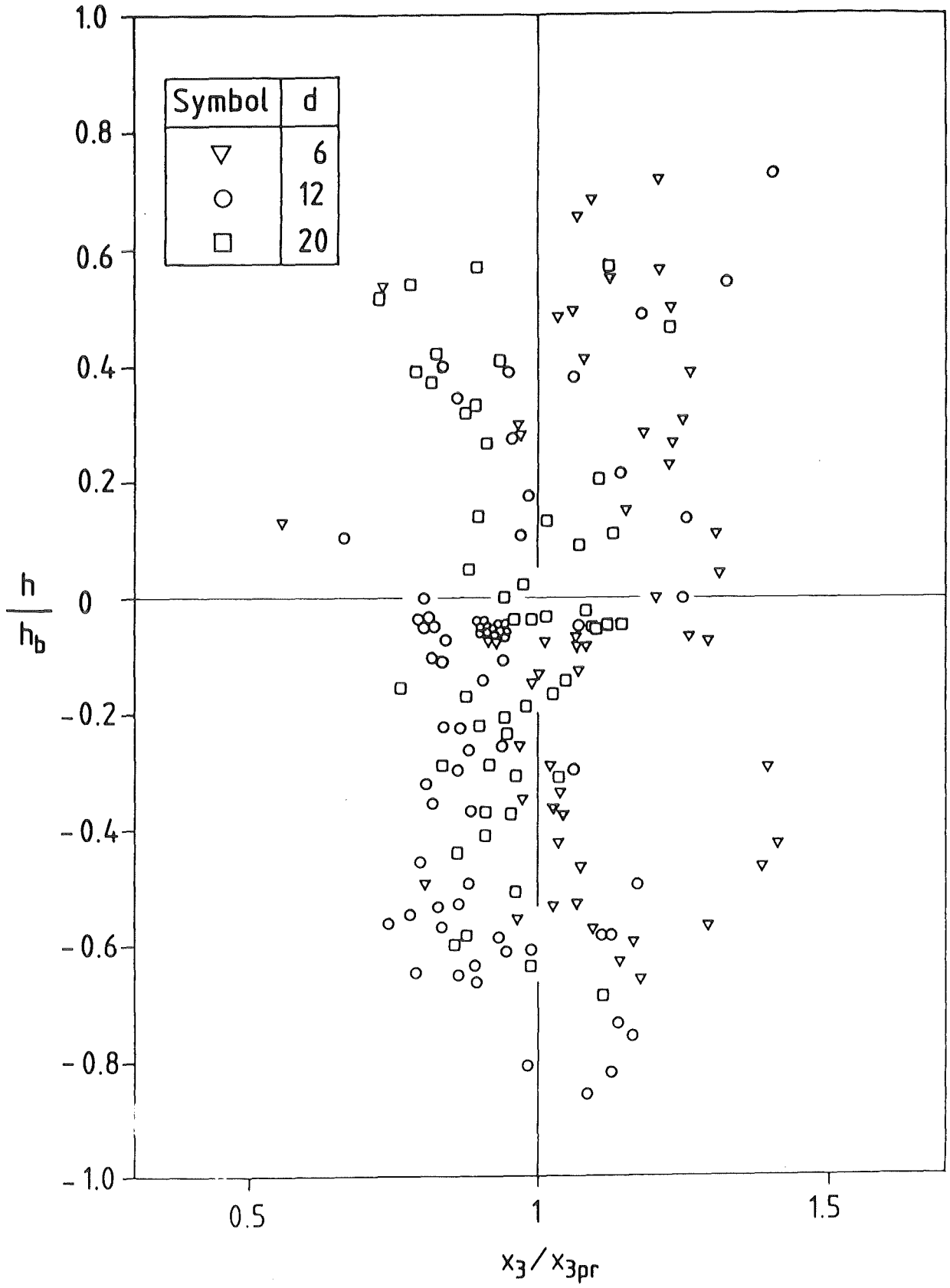

Fig. 40: Dimensionless interface level h/h_b as a function of measured to predicted quality in horizontal branches.

6.2.3.2 Donward Branches

For downward branches h was measured from the bottom of the horizontal pipe, which gives a quality x_3 approaching unity for h approaching zero. The correlation (46) was modified to satisfy this condition, and the data in Fig. (33) were fitted with the following expression:

$$x_{3pr} = \left(\frac{1.15}{1+\sqrt{\rho_e/\rho_g}}\right)^{2.5\frac{h}{h_b}} \left[1 - \frac{1}{2}\frac{h}{h_b}\left(1+\frac{h}{h_b}\right)\left(\frac{1.15}{1+\sqrt{\rho_e/\rho_g}}\right)^{\left(1-\frac{h}{h_b}\right)}\right]^{0.5} \qquad (47)$$

where the exponent 2.5 was adjusted to give a minimum mean square error.

Figure 41 shows the ratio x_3/x_{3pr} as a function of h/h_b for g.e. in downward branches. The strong data scatter observed at $h/h_b > 0.9$ where the relative error in the measured quality is lower than 20 %, is due to the practically horizontal fitting curve at low qualities (see Fig. 33). In fact, for $x_3 <$ 0.1 % ($h/h_b > 0.9$) an error of ± 5 % in h/h_b can introduce an error greater than 100 % in the predicted quality. However, in general, a symmetrical distribution of data around $x_3/x_{3pr} = 1$ is obtained. For $h/h_b < 0.9$ the standard deviation is $\sigma = 30$ %.

6.2.3.3 Upward Branch

The l.e. in upward branches can be considered as a flow phenomenon similar to the g.e. in downward branches with gas and liquid replaced by liquid and gas, respectively. Therefore, to predict the quality in upward branches an expression of the form:

$$x_{3pr(upward)} = 1 - x_{3pr(downward)} \qquad (48)$$

is proposed, with $x_{3pr(downward)}$ as given by Eq. (47). Again there is a change in the normalization factor h_b when passing from g.e. (downward) to l.e. (upward), therefore the exponent 2.5 h/h_b used in Eq. (47) was replaced by: 2.5 C_1 h/h_b, with $C_1 = h_{b.l.e.(upward)}/h_{b.g.e.(downward)}$. Calculating this coefficient as previously (Section 6.2.3.1) results in: $C_1 = 0.8$, and the expression proposed in (48) becomes:

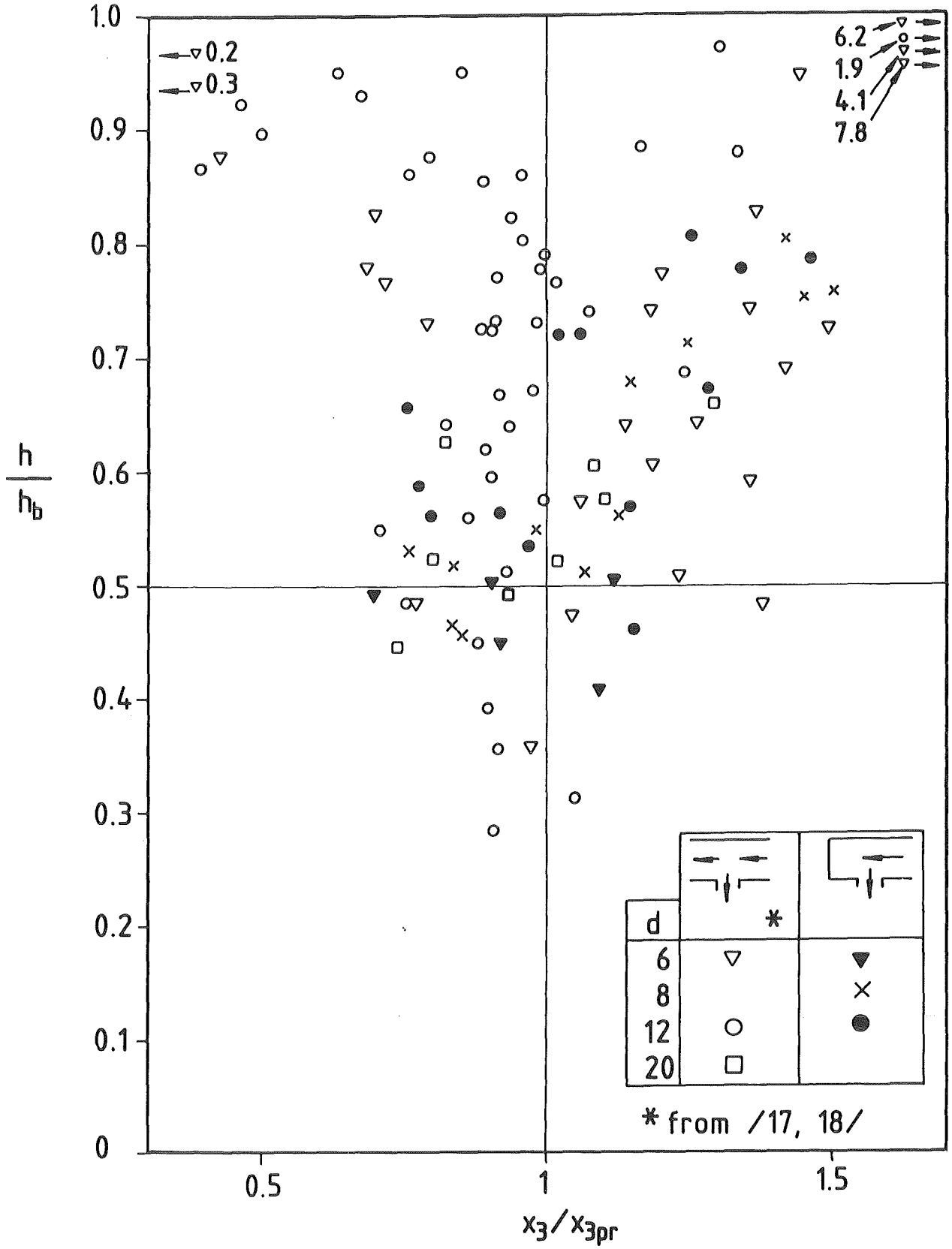

Fig. 41: Dimensionless interface level h/h_b as a function of measured to predicted quality in downward branches.

$$x_{3pr} = 1 - \left(\frac{1.15}{1+\sqrt{\rho_l/\rho_g}}\right)^{2\frac{h}{h_b}} \left[1 - \frac{1}{2}\frac{h}{h_b}\left(1+\frac{h}{h_b}\right)\left(\frac{1.15}{1+\sqrt{\rho_l/\rho_g}}\right)^{\left(1-\frac{h}{h_b}\right)}\right]^{0.5} \tag{49}$$

This correlation was used to draw the dashed curve in Fig. 35a assuming P_1 = 4 bar. The discrepancy with respect to the mean value of the experimental results is not greater than 1 %.

The ratio x_3/x_{3pr} as a function of h/h_b is presented in Fig. 42. An increasing scatter around the value $x_3/x_{3pr} = 1$ is observed for decreasing h/h_b which coincides with the occurrence of waves and intermittent slug in the main pipe. Discarding the points corresponding to developed slug flow, the standard deviation of the data is very low: σ = 1.5 %.

The results in Section 6.2.3 give correlations to predict the branch quality which are functions of the densities ratio and dimensionless interface level only:

$$x_{3pr} = f\left(\frac{\rho_l}{\rho_g}, \frac{h}{h_b}\right) \tag{50}$$

These correlations are considered as applicable to arbitrary fluids and arbitrary flow geometries downstream of the branch entrance, that means, they should be valid for orifices, pipe studs, nozzles, etc.

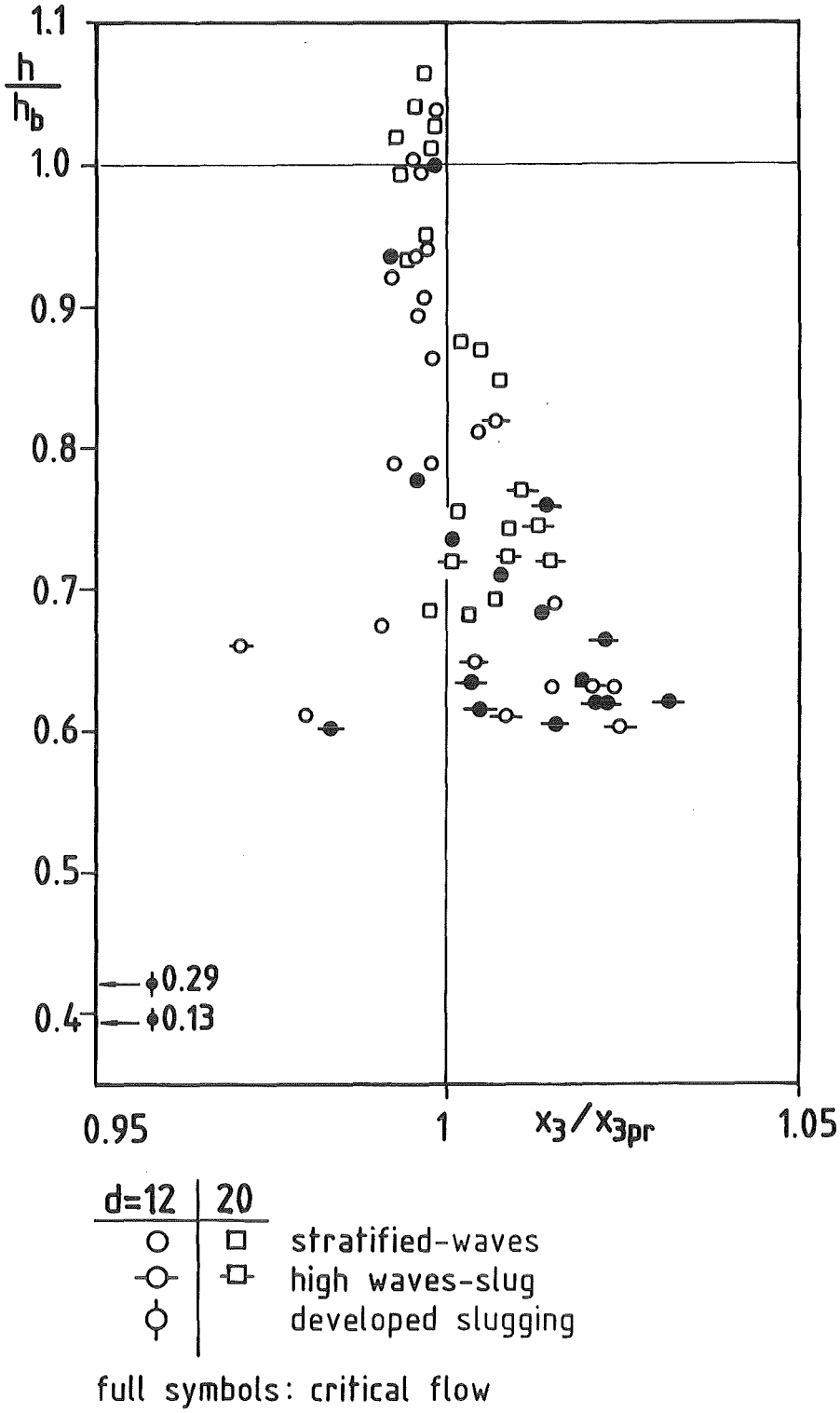

Fig. 42: Dimensionless interface level h/h_b as a function of measured to predicted quality in upward branches.

6.2.4 Correlations for the Branch Mass Flux

For two-phase flow the expansion coefficient ε in Eq. (37) was replaced by the expression $[1 + \alpha(\varepsilon - 1)]$, where α is the void fraction, therefore:

$$G_3 = \zeta\left[1 + \alpha(\varepsilon - 1)\right]\sqrt{\rho\,\Delta P_{1-34}} \tag{51}$$

With an appropiate model giving α and ρ as a function of x_3, Eq. (51) could be combined with the results in Section 6.2.3 to predict the total branch mass flux. Models for the branch mass flux are strongly dependent on the branch geometry and, therefore, will be different for orifices, nozzles, pipe studs etc.

It was not the aim of this investigation to model in detail the branch mass flux for the special geometry used in the present experiments therefore only the simplest model, the homogeneous model, has been applied and Eq. (51) is rewritten as follows:

$$G_{3H} = \zeta\left[1 + \alpha_H(\varepsilon - 1)\right]\sqrt{\rho_H\,\Delta P_{1-34}}$$

where (52)

$$\alpha_H = \left(1 + \frac{1-x_3}{x\,\rho_\ell/\rho_g}\right)^{-1} \; ; \quad \rho_H = \left(\frac{x_3}{\rho_g} + \frac{1-x_3}{\rho_\ell}\right)^{-1}$$

For each branch diameter the ratio of measured to homogeneous mass flux, G_3/G_{3H}, was plotted as a function of the quality measured in experiments with the three branch orientations.

Results for each branch diameter are presented in Fig. 43. It is obvious that the homogeneous model does not describe properly the branch mass flux for qualities between 2 and 60 %. However, almost the same dependency of G_3/G_{3H} on X_3 was obtained for the different diameters and, therefore, it was possible to use a single fitting function $F(x_3)$, valid for the branches used and expressed by:

$$\frac{G_3}{G_{3H}} \simeq F(x_3) = \begin{cases} 1 + (1-x_3)(-61\,x_3^2 + 12.2\,x_3) & ; \; x_3 \leq 0.1 \\ 1 + (1-x_3)\,x_3^{0.12}\,e^{-2.2x} & ; \; x_3 \geq 0.1 \end{cases} \tag{53}$$

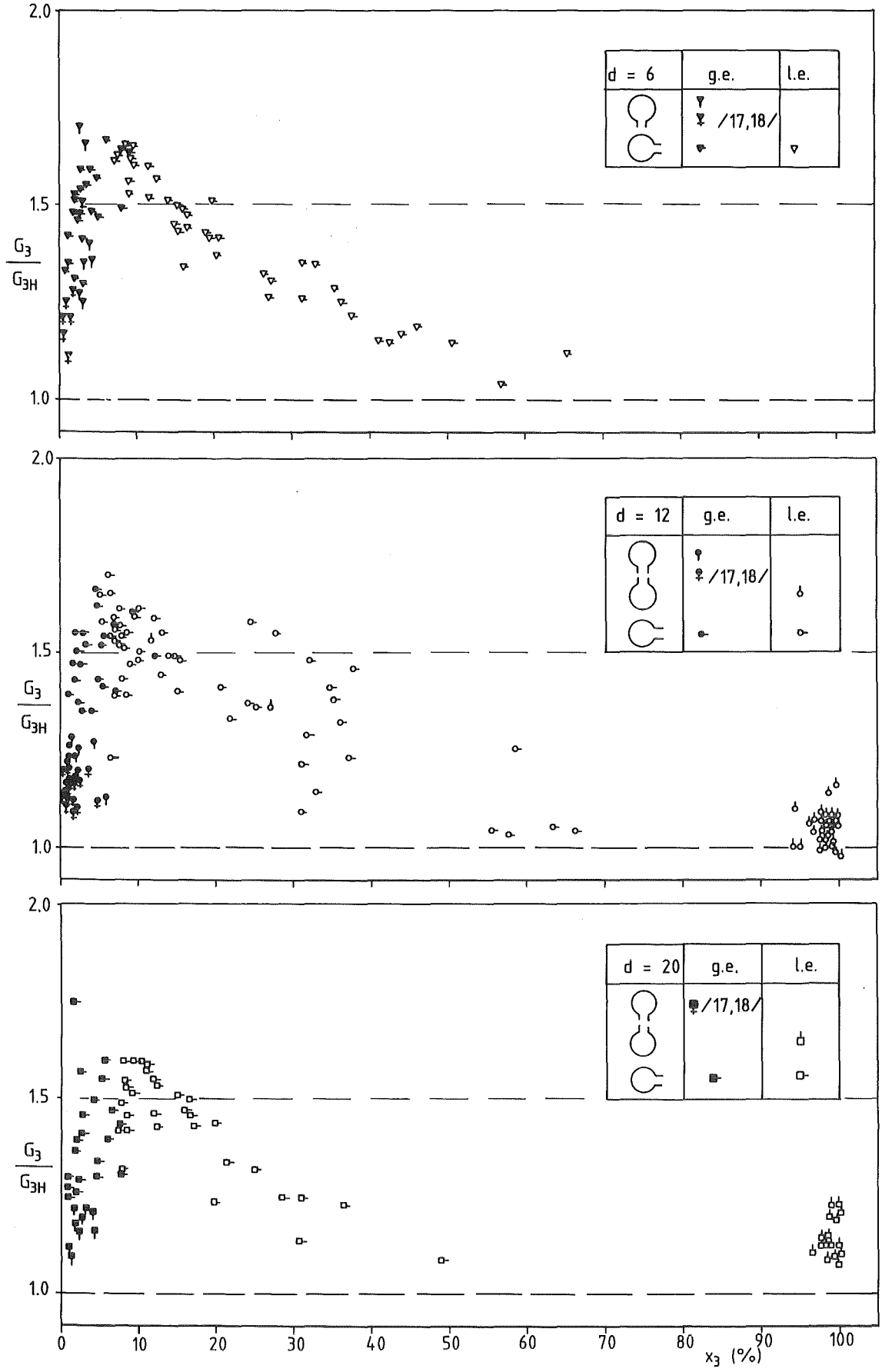

Fig. 43: Ratio of measured to homogeneous branch mass flux G_3/G_{3H} as a function of the branch quality x_3.

It is to note that this function should not be used for other branch geometries. To check the validity of Eq. (53) for the geometries under consideration, a predicted branch mass flux was calculated as a function of the measured quality x_3 as follows:

$$G_{3Pr}(x_3) = G_{3H}(x_3)\ F(x_3) \tag{54}$$

With this procedure the ratios of measured to predicted branch mass fluxes G_3/G_{3pr} were calculated for each branch orientation and plotted as a funtion of x_3, as shown in Fig. 44. Figure 44a, corresponding to l.e. in upward branches, shows that for $x_3 > 97$ % the measured G_3 is about 8 % greater than the predicted one. A discrepancy of the same order is observed for $x_3 < 1$ % in Fig. 44b, corresponding to g.e. in downward branches, whereas in Fig. 44c, for gas and liquid entrainment in horizontal branches, a fairly symmetric distribution around the value one, is observed for all qualities.

The differences between the measured and predicted mass fluxes can be corrected by fitting the data in Fig. 43 with a different function $F(x_3)$ for each branch diameter, which gives a different G_{3pr} for each branch; but again this was not the aim of this investigation. Therefore, the final correlation proposed to predict the branch mass flux is:

$$G_{3pr} = G_{3H}(x_{3pr})\ F(x_{3pr}) \tag{55}$$

where x_{3pr} is calculated with the correlations obtained in Section 6.2.3 for each branch orientation.

The corresponding results, showing the ratio G_3/G_{3pr} for the diffeent branch orientations as a function of h/h_b, are presented in Figs. 45-47. The standard deviation of data from 1 is σ = 18 % for upward branches (Fig. 45), σ=12 % for downward branches (Fig. 46), and σ= 9.5 % for horizontal branches (Fig. 47). These relative small deviations correlate with the asymmetries observed in Fig. 44.

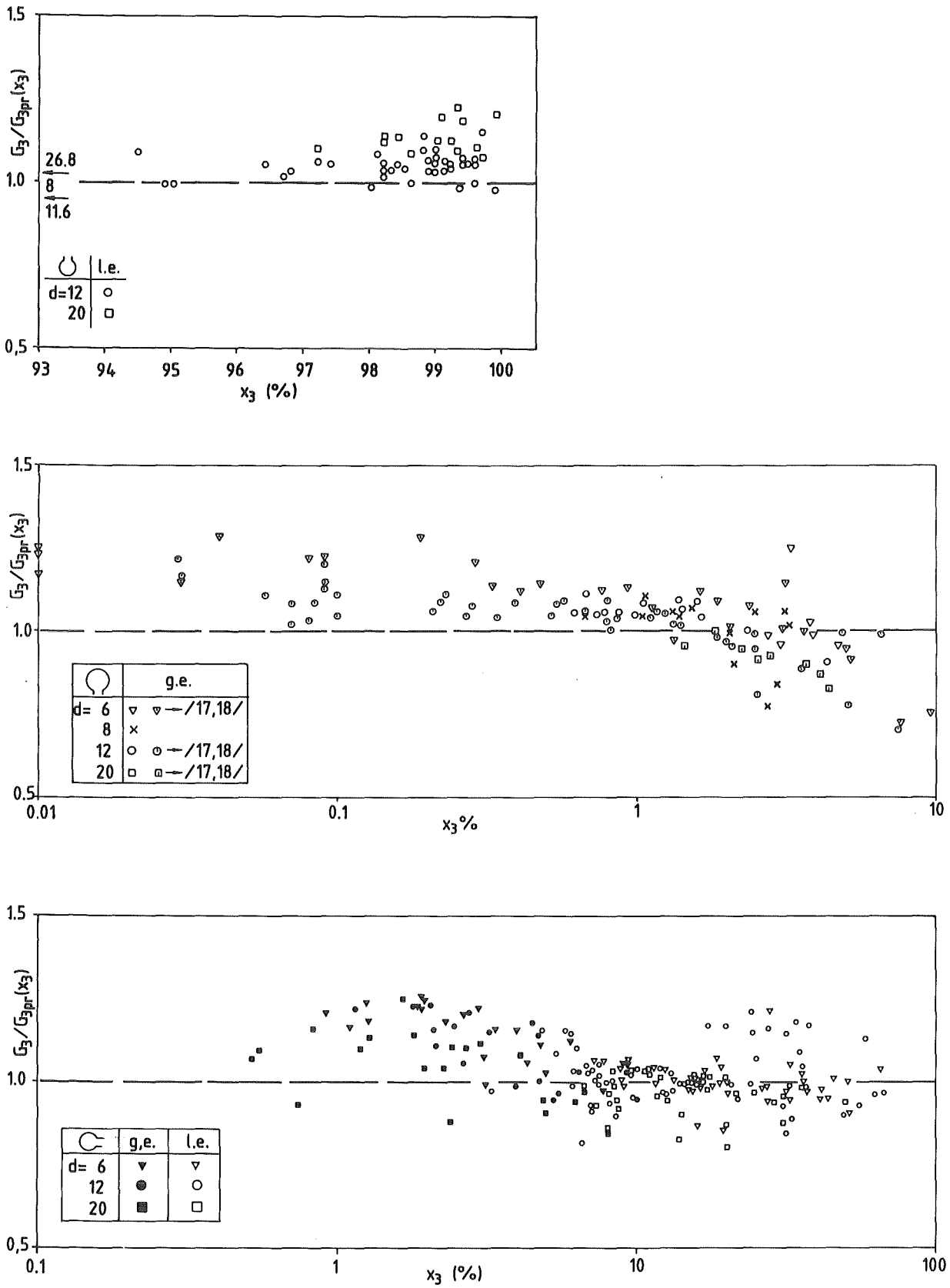

Fig. 44: Measured to predicted mass flux $G_3/G_{3pr}(x_3)$ as a function of the quality x_3 in upward, downward and horizontal branches.

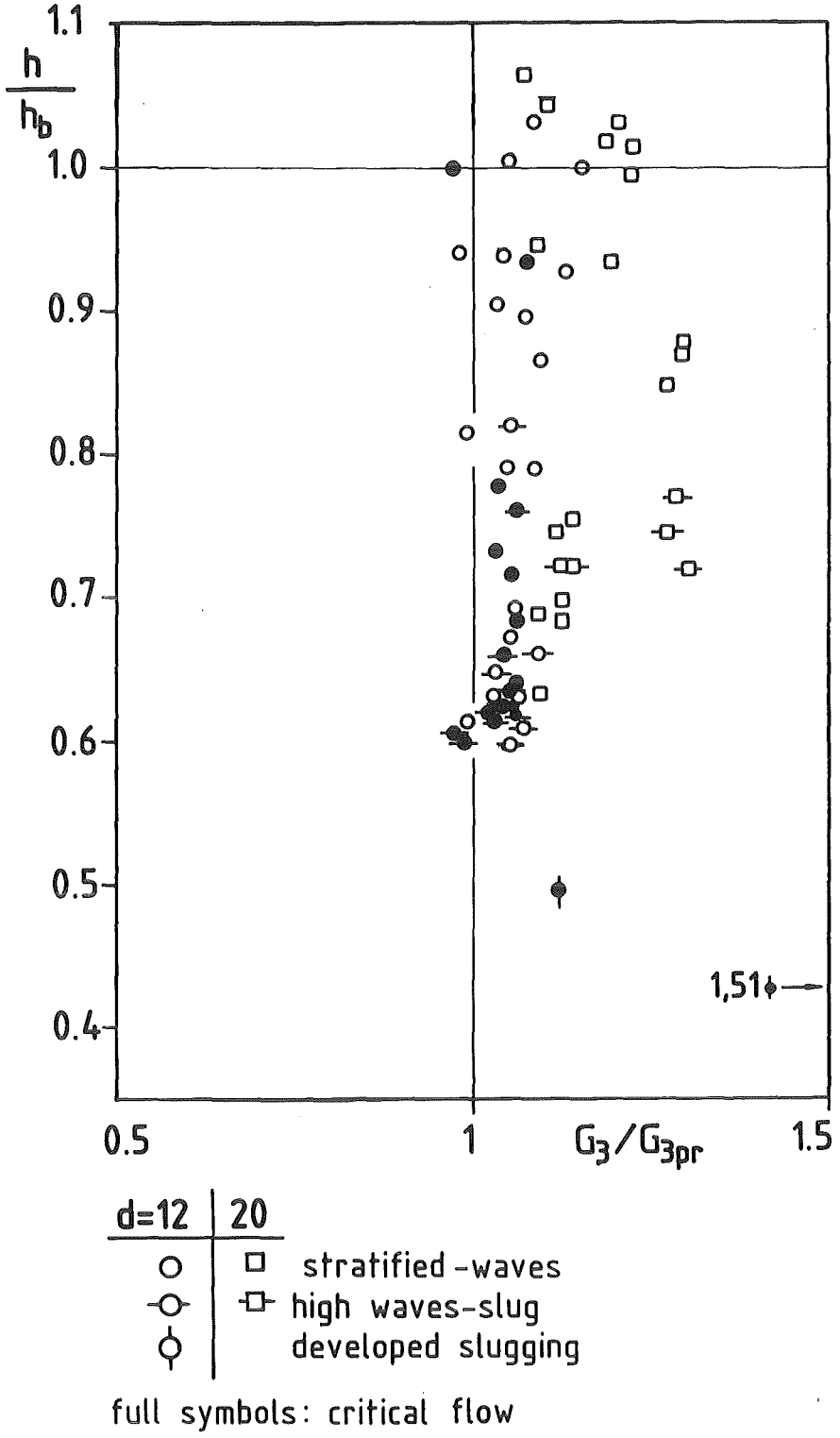

Fig. 45: Dimensionless interface level h/h_b as a function of measured to predicted mass flux G_3/G_{3pr} in upward branches.

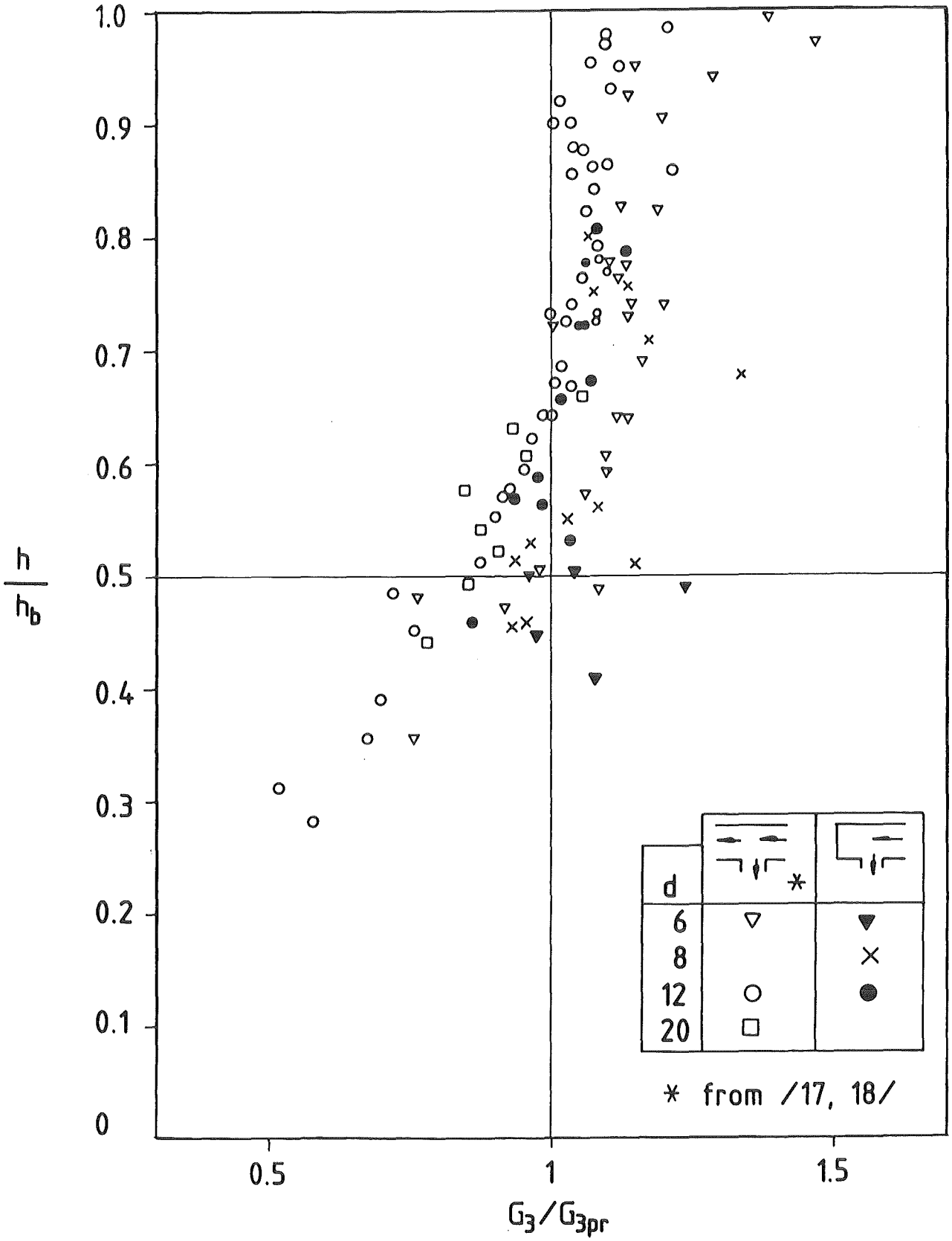

Fig. 46: Dimensionless interface level h/h_b as a function of measured to predicted mass flux G_3/G_{3pr} in downward branches.

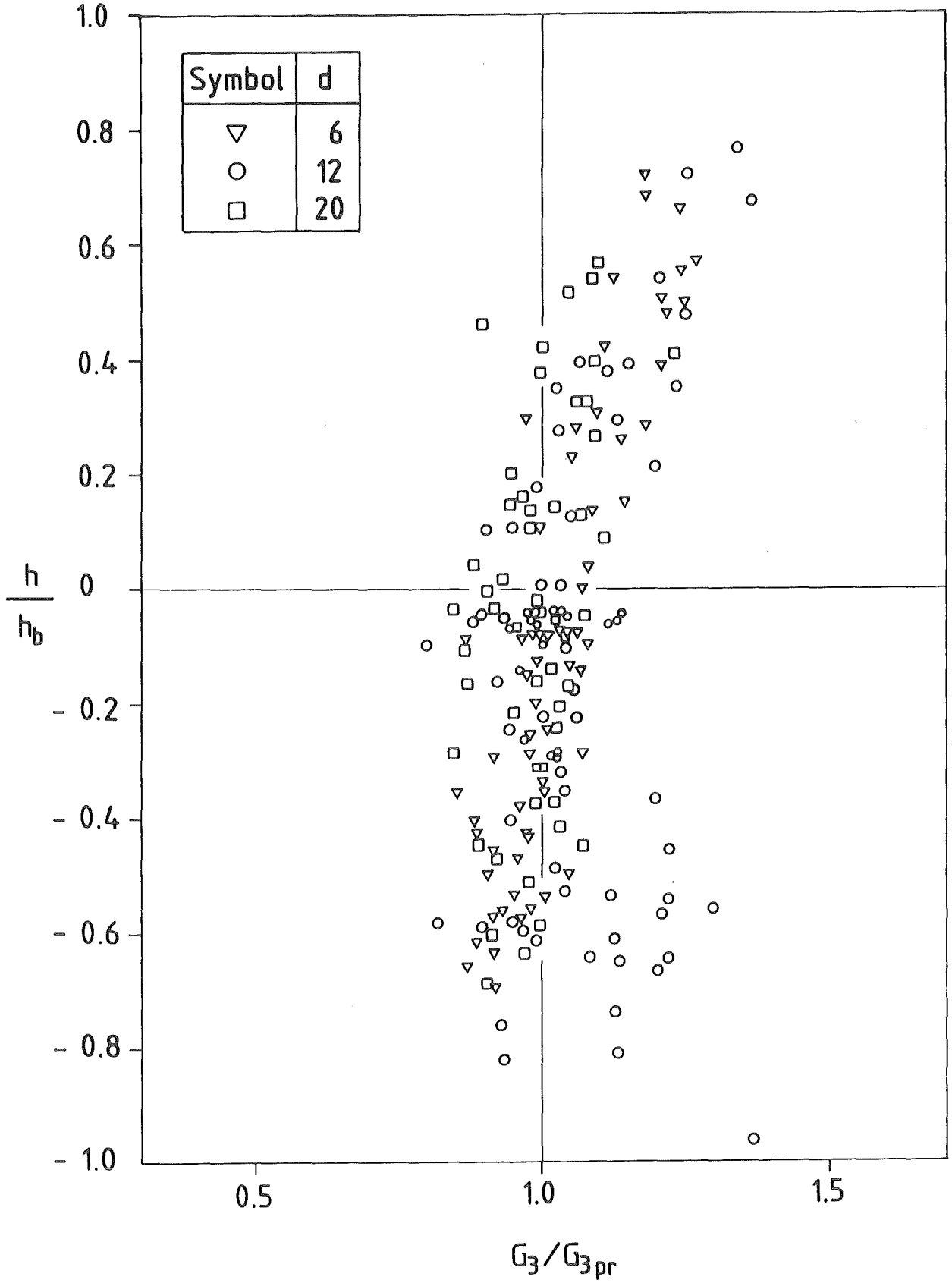

Fig. 47: Dimensionless interface level h/h_b as a function of measured to predicted mass flux G_3/G_{3pr} in horizontal branches.

7. Critical Branch Mass-Flux

7.1 The Homogeneous Equilibrium Model (HEM)

The model discussed up to now is valid for subcritical gas-liquid flow. However in a small break LOCA critical steam-water flow at high pressure occurs; therefore, in the previous correlations an appropiate model for critical two-phase flow has to be used. Such a model will depend on the break geometry and many articles have been published on this subject (compare e.g. D'Auria and Vigni, /34/). It is not the aim of this work to model in detail the critical mass flux for the special break geometry used in the present experiments but rather to explain the procedure and show typical tendencies.

For the following derivations it is assumed that during the small break LOCA:
- the interface is ideally stratified;
- there is no effect of the flashing, produced by the pressure drop in the vicinity of the break on the flow field near the horizontal interface;
- there are no bubbles in the liquid produced by the decrease of the system pressure or by heat transfer from the pipe walls.

On these hypotheses the very simple Homogeneous Equilibrium Model (HEM), /35/, will be applied which gives satisfactory results for long pipes with a large ratio l/d (compare Wallis /36/).

The basic assumptions of the HEM (for details see Appendix A3) are:

- Homogeneity: both phase have the same velocity and their channel averaged properties give the thermodynamical properties of the mixture.
- Thermodynamical equilibrium: liquid and vapor have the same pressure and temperature.
- Isentropic flow: neither heat nor work are interchanged with the exterior.

The HEM provides a thermodynamic connection of the flow properties upstream of the break and in the break cross section. Weigand et al. /37/, for instance, have used the HEM to develop a computational model for analyzing two-phase jets, and they give critical flow charts relating the break mass flux and thermodynamic properties to the upstream stagnation conditions. In particular, Figure 48 (from /37/) gives the HEM critical mass-flux in the break cross section as a function of the stagnation quality and stagnation tempera-

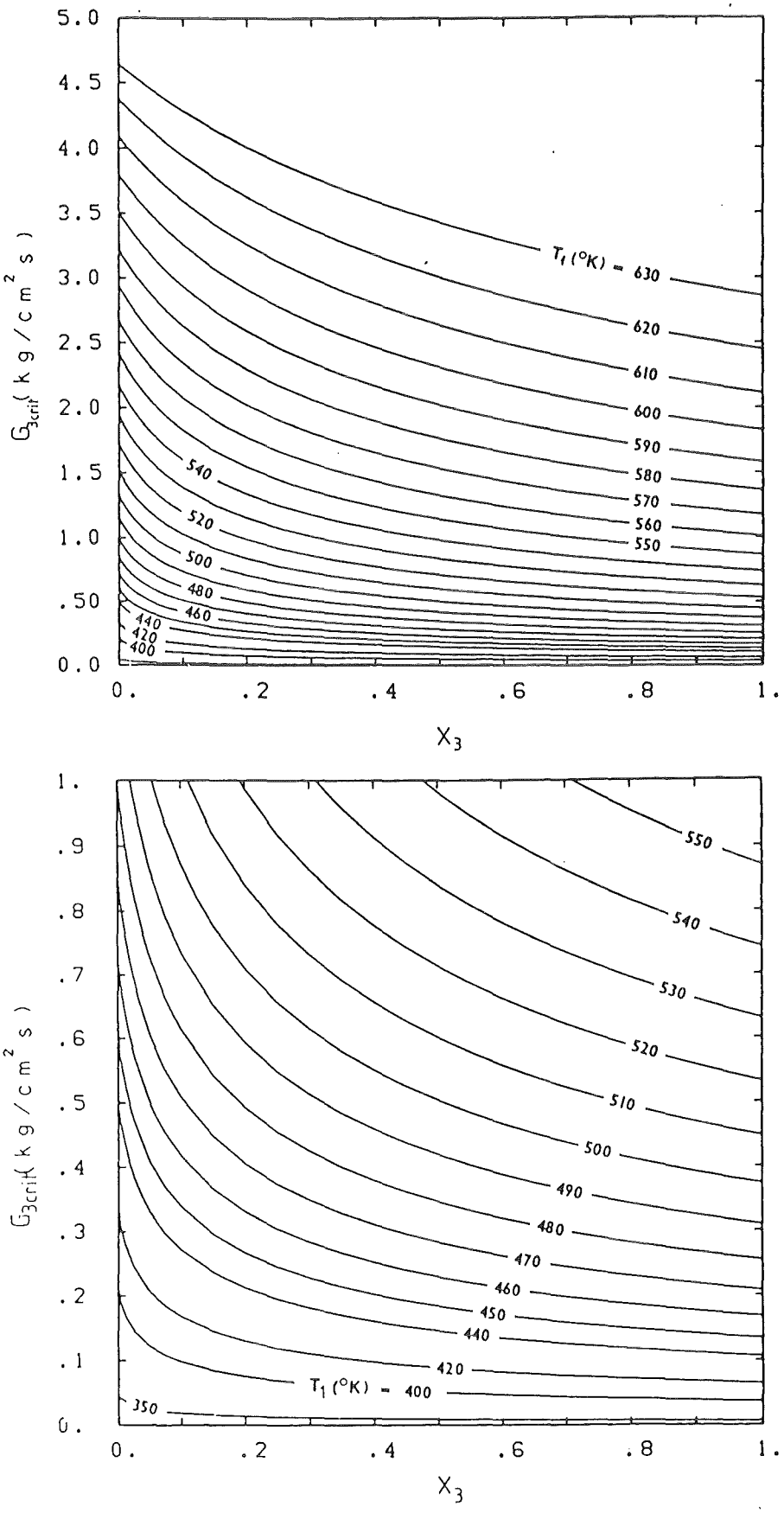

Fig. 48: HEM critical mass flux as a function of stagnation quality and temperature.

ture of a saturated mixture. The information provided by these curves will be used in the next section to predict the critical mass flux in horizontal branches.

7.2 Quality and Critical Mass Flux in Horizontal Branches

The model proposed for x_o in Section 6.2.3.1 is assumed to be independent of the flow behavior downstream of the branch entrance; therefore, it can be applied also to critical branch flows. However, the normalization factor h_b has to be calculated with the critical value of W_{3b} given by the HEM curve corresponding to the system pressure.

For constant P_1 the correlation (5) gives:

$$h_{b.g.e.} = \frac{K_{ge}\, W_{3\ell\,crit}^{0.4}}{\left[g\, \rho_\ell\, (\rho_\ell - \rho_g)\right]^{0.2}} \tag{56}$$

$$h_{b.\ell.e.} = \frac{K_{\ell e}\, W_{3g\,crit}^{0.4}}{\left[g\, \rho_g\, (\rho_\ell - \rho_g)\right]^{0.2}} \tag{57}$$

Equations (56) and (57) were used to calculate h_b for arbitrary values of $h > 0$ and $h < 0$, respectively. The correlation (46) was used to predict the corresponding quality.

With this value of x_3 interpreted as the stagnation quality again the HEM curve for P_1 was used to determine the corresponding critical branch mass flux.

7.3 Application of the Model

The procedure presented above was applied to predict the branch quality and mass-flux, in case of a LOCA produced by a side break in a horizontal coolant pipe of a standard reactor (I.D. 750 mm). The branch diameter was assumed to be 49 mm to simulate a break with a ratio of break to main pipe cross sectional area of 0.4 %.

Calculations based on system pressures of 5 and 10 MPa were made taking into account the values in the table below:

Parameters	P_1=5 MPa	P_1=10 MPa	References
Tsat ^oK	537	584.15	steam-water
$\rho_{g\ sat}$ kg m^{-3}	25.40	55.5	thermodynam.
$\rho_{l\ sat}$ kg m^{-3}	778	688	properties
$G_{3g\ crit}$ 10^{-4} kg $m^{-3}s^{-1}$	0.714	1.45	HEM (Fig. 48)
$G_{3l\ crit}$ 10^{-4} kg $m^{-3}s^{-1}$	2.067	3.35	HEM (Fig. 48)
h_{bge} m	0.144	0.185	Eq. 56
h_{ble} m	0.172	0.202	Eq. 57

Table 5: Parameters used to predict the quality in branches with critical mass flux.

The results were plotted as a function of h_l/D (Fig. 49), where $h_l = D/2 + h$ is the liquid level measured from the bottom of the main pipe.

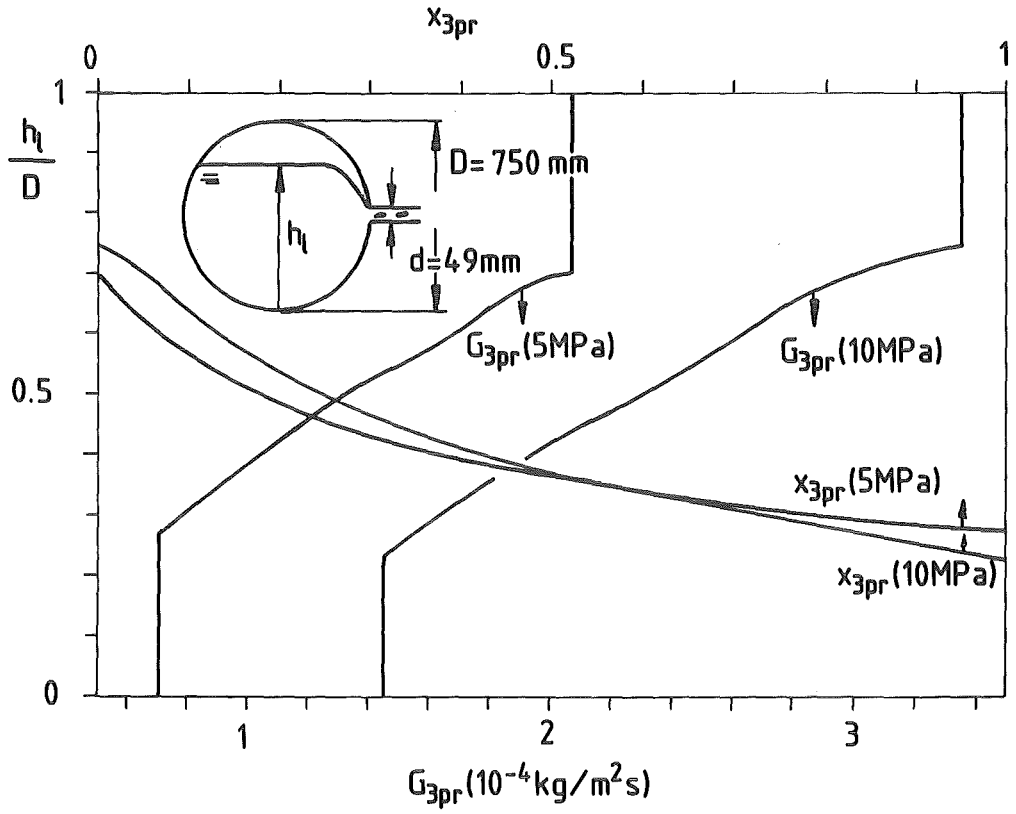

Fig. 49: Dependency of predicted branch quality x_{3pr} and critical mass flux G_{3pr} on the dimensionless liquid level $h_{l/D}$.

Starting at $h_1/D = 1$ and for decreasing values of the liquid level in the main pipe, the predicted branch quality and mass flux are constant until the point is reached at which the vapor filling the pipe portion above the interface, begins to be entrained in the branch. Below this point, the branch flow is described by x_{3pr} ranging from 0 to 1 and the corresponding G_{3pr} decreasing to its minimal value where no longer liquid entrainment occurs. For smaller values of h_1, only vapor flows through the branch, therefore, x_{3pr} = 1 and G_{3pr} = constant. As expected, a higher pressure extends the range of h_1/D for which steam or water entrainment occurs.

7.4 Comparison with other Models

Two other models for the branch quality which will be combined with the HEM will be considered below:

a) the model used in the RELAP4 computer code /38/, originally developed for large break LOCA with the assumption made that the branch inlet void fraction α_3 is equal to the upstream void fraction α_1:

$$\alpha_3 = \alpha_1 \tag{58}$$

b) the model used in the RELAP5 computer code /39/, which was specially developed to calculate the mass discharge from horizontal pipes with stratified flow through side breaks.

In RELAP5 (see details in Appendix A4) the limit gas velocity v_{gL} in the horizontal pipe with diameter D and liquid level h_1, is defined as:

$$v_{gL} = \frac{1}{4\sqrt{2}}\left(1-\cos\theta\right)\left[D g \frac{\rho_\ell - \rho_g}{\rho_g} \frac{2\theta - \sin 2\theta}{\sin\theta}\right] \tag{59}$$

where $\theta = \cos^{-1}(2\,h_1/D - 1)$. The void fraction α_3, at the inlet of a horizontal branch of diameter d, is defined as follows: for the interface above and below the branch entrance, respectively:

$$\alpha_3 = \alpha_1 \left(\frac{v_{1g}}{v_{gL}}\right)^{0.5} \qquad \text{for} \quad h_\ell > \frac{D+d}{2} \tag{60}$$

$$\alpha_3 = 1 - (1-\alpha_1)\left(\frac{v_{1g}}{v_{gL}}\right)^{0.5} \qquad \text{for} \quad h_\ell < \frac{D-d}{2} \tag{61}$$

When the liquid level lies within the outlet area, i.e., when $(D-d)/2 < h_1 < (d + D)/2$, α_3 is obtained by interpolation of the two void fractions computed at the boundaries.

To predict the branch quality, the correlation corresponding to homogeneous branch mass-flow was used:

$$x_{3pr} = \left[1 + \left(\frac{1}{\alpha_{3pr}} - 1 \right) \frac{\rho_\ell}{\rho_g} \right] \tag{62}$$

where α_{3pr} is the value given by RELAP4 (Eq. (58)) or RELAP5 using Eqs. (60-61), with the value $v_{1g} = 1$ m/s.

Results for branch quality and mass flux given by the different models are compared in Figures 50 and 51.

Figure 50 shows that the discrepancy between the predicted qualities depends on the liquid level. For h_1/D below the value corresponding to b.g.e., the new qualities are greater than those given by RELAP4 and RELAP5, the maximum difference representing one order of magnitude.

The corresponding values for G_{3pr} are compared in Figure 51 For a wide range of h_1/D the mass fluxes calculated with the new model are smaller than the values given by RELAP4 and RELAP5.

The constant values of x_{3pr} and G_{3pr} above and below the levels corresponding to b.g.e. and b.l.e., respectively, constitute a difference introduced by the model proposed in the present investigation.

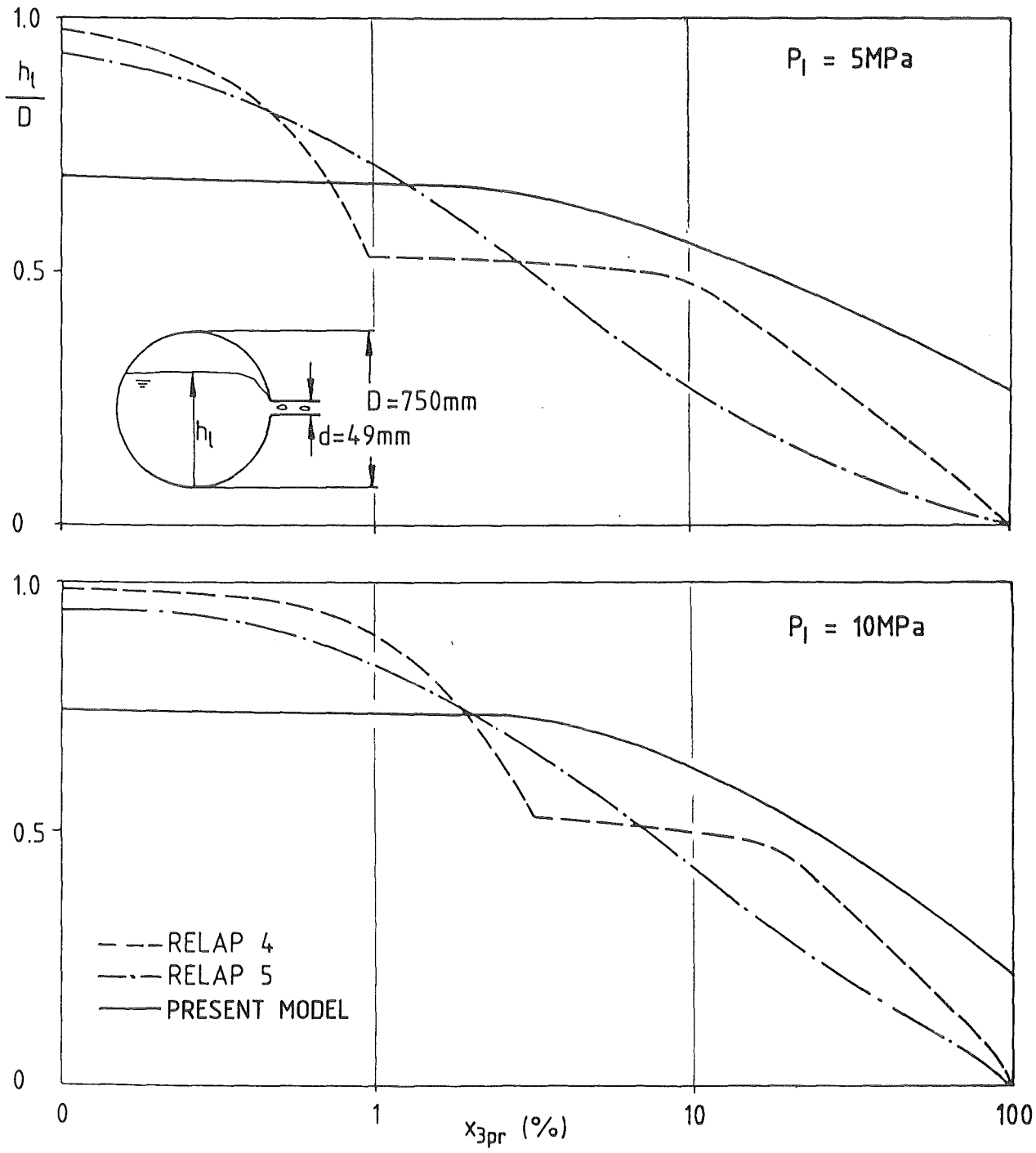

Fig. 50: Comparison of the different models to predict the quality for critical branch flow and varying liquid level in the main pipe.

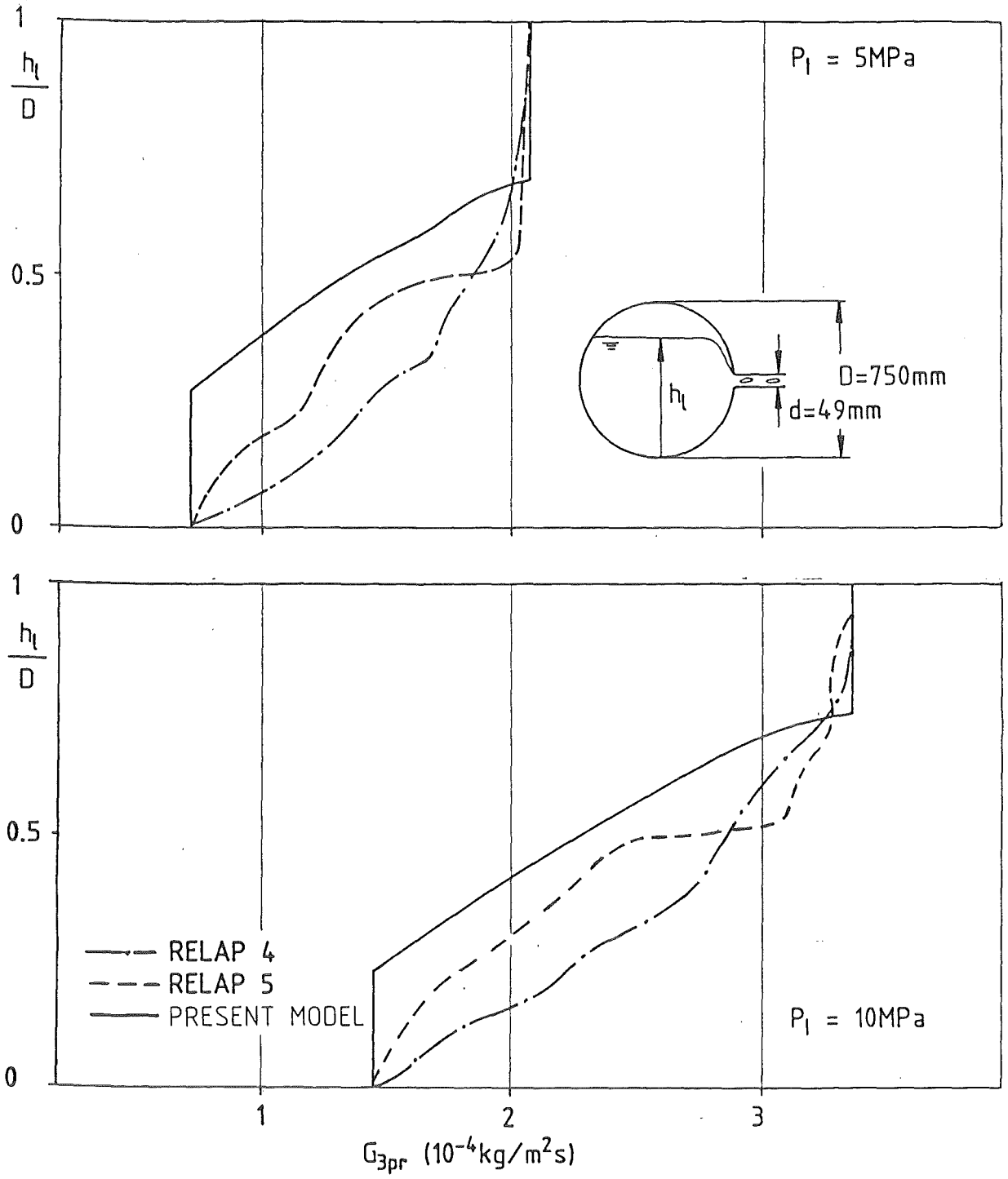

Fig. 51: Comparison of the different models to predict the critical branch mass flux for varying liquid levels in the main pipe.

Summary

The mass flow rate and quality through small branches at the bottom, the top or the side of a horizontal pipe with stratified flow was investigated.

The problem is of importance for the study of loss of coolant accidents (LOCA) in nuclear reactors. Limited knowledge of this subject was available from the literature: the publications concentrate on gas and liquid withdrawal from large reservoirs and only correlations for the beginning of entrainment were given.

In the present investigation conditions of interest for nuclear reactors were established by:
- flow geometries without rotational symmetry,
- pipe flows downstream of the branch (superimposed velocities)

Circular branches with diameters of 6, 8, 12 or 20 mm, perpendicular to the main pipe with a diameter of 206 mm, were used. The experiments were performed with air-water flow at ambient temperature and a maximum pressure of 0.5 MPa.

The flow towards the branch was observed to be vortex or vortex-free, depending on the branch orientation and superimposed velocity. Photographs are presented to illustrate the different flow phenomena.

A general correlation was developed to determine the beginning of entrainment for the three branch orientations investigated.

During entrainment, measurements were made of the branch quality and mass flux. Results are presented as a function of a normalized distance between interface and branch entrance.

A model was developed to predict the branch quality for arbitrary fluid systems.

The results were extended to steam-water flow at high pressure with horizontal critical branch mass flux and compared with other models.

The experiments presented in this report have improved the understanding of the flow process originating in small breaks in a horizontal pipe with stratified flow. The results can also be applied to small breaks at the bottom, the top or a side of large reservoirs and, therefore, they are useful in the development of safety codes for small break LOCA.

Further experiments with similar geometries and single component fluid system will be necessary to investigate the influence of local flashing near the interface on the beginning of entrainment and on the branch quality and mass flux.

Acknowledgements

The author wants to express her gratitude to Dr.-Ing. J. Reimann for his numerous discussions, useful suggestions and valuable assistance during the preparation of this work. The author is also grateful to Prof. Dr.-Ing. U. Müller for his advice and stimulation.

9. Literature

/1/ P.B. Walley and B.J. Azzopardi, "Two-Phase Flow in a T-Junction", AERE-R 9699, 1980.

/2/ J.A.R. Henry, "Dividing Annular Flow in a Horizontal Tee", J. Multiphase Flow, Vol. 7, pp 343-355, 1981.

/3/ T.J. Honan and R.T. Lahey, jr., "The Measurement of Phase Separation in Wyes and Tees", Nuclear Engineering and Design, Vol. 64, No. 1, 1981.

/4/ K. Zetzmann, "Phasenseparation und Druckabfall in zweiphasig durchströmten vertikalen Rohrabzweigen, Diss. Universität Hannover, 1982.

/5/ N. Saba and R.T. Lahey, "Phase Separation Phenomena in Branching Conduits", NUREG/CR-2590, 1982.

/6/ J. Reimann, H.J. Brinkmann, A. Demski, H. John, L. Pawlak, W. Seeger, C. Smoglie, E. Wanner, E. Weinbrecht, "Gemeinsamer Versuchsstand zum Testen und Kalibrieren verschiedener Zweiphasen-Massenstrom-Meßverfahren", PNS Jahresbericht 1982, KfK 3350, 1983, pp. 4100-94.

/7/ J. Reimann, H.J. Brinkmann, G. Eisele, H. John, L. Pawlak, W. Seeger, C. Smoglie, E. Wanner, E. Weinbrecht; IRB, "Gemeinsamer Versuchsstand zum Testen und Kalibrieren verschiedener Zweiphasenmassenstrom-Meßverfahren", PNS Jahresbericht 1983, KfK 3450, 1984, pp. 4100-131.

/8/ W. Seeger, "Untersuchungen zum Druckabfall und zur Massenstromumverteilung von Zweiphasenströmungen in rechtwinkligen Rohrverzweigungen", Dissertation Universität Karlsruhe, 1984.

/9/ L. Dagget and G. Keulegan, "Similitude in Free Surface Vortex Formation", J. Hydr. Div. ASCE, Vol. 100, 1506, 1974.

/10/ B. Lubin and M. Hurwitz, "Vapor Pull-Through at a Tank Drain with and without Dielectrophoretic Buffling", Proc. Conf. Long Term Cryopropellant Storage in Space, NASA Marshall Space Center, Huntsville, Ala., p. 173., 1966.

/11/ H. Rouse, J. Davidian, J.E. Glover and D.W. Appel, "Development of the Non-Circulatory Waterspont", J. Hydraulics Division, HY4, August 1956, Paper 1038.

/12/ H. Craya, "Theoretical Research on the Flow of Non-Homogeneous Fluids", La Houille Blanche, pg. 44-55, Jan.-Feb. 1949

/13/ P. Gariel, "Experimental Research on the Flow of Non-Homogeneous Fluids", La Houille Blanche, pg. 56-64, Jan.-Feb. 1949

/14/ N. Zuber, "Problems in Modeling of Small Break LOCA", NUREG-0724, 1981

/15/ G.R. Houdayer, J.M. Miraucourt, J.C. Micaelli, "Description of Volumes in Cathare Code", European Two Phase Flow Group Meeting, Zürich, 14-17th June, 1983

/16/ C.J. Crowley and P.H. Rothe, "Flow visualization and Break Mass Flow Measurements in Small Break Separate Effects Experiments", ANS Specialist Meeting on Small Break Loss of Coolant Accident Analyses in LWR's, Monterey, California, Aug. 25-27, 1981.

/17/ J. Reimann, M. Khan, "Flow Through a Small Pipe at the Bottom of a Large Pipe with Stratified Flow"; Annual Meeting of the European Two-Phase Flow Group, Paris la Defense, June 2-4, 1982.

/18/ J. Reimann, M. Khan, "Flow Through a Small Pipe at the Bottom of a Large Pipe with Stratified Flow"; Second International Topical Meeting on Nuclear Reactor Thermal-Hydraulics, Santa Barbara, California, January 11-14, 1983.

/19/ H. John, J. Reimann, "Gemeinsamer Versuchsstand zum Testen und Kalibrieren verschiedener Zweiphasen-Massenstrom-Meßverfahren", KfK 2731 B, Februar 1979.

/20/ J. Reimann, H. John, H.J. Brinkmann, A. Demski, L. Pawlak, W. Seeger, E. Wanner, R. Weinbrecht, "Gemeinsamer Versuchsstand zum Testen und Kalibrieren verschiedener Zweiphasen-Massenstrom-Meßverfahren", PNS 4137, JB 1981, KfK 3250, 1982, pp. 4100-186.

/21/ J. Reimann, C. Smoglie, "Flow through a small pipe at the top of a large pipe with stratified flow"; Annual Meeting of the European Two-Phase Flow Group, Zürich, Switzerland, June, 14-16, 1983.

/22/ J. Lighthill, "Waves in Fluids", Cambridge University Press 1978.

/23/ H. Lamb, "Hydrodynamics", Cambridge University Press 1975.

/24/ Y. Taitel and A.E. Dukler, "A Model for Predicting Flow Regime Transitions in Horizontal and Near Horizontal Gas-Liquid Flow", AIChE Journal, Vol. 22, No. 1, Jan. 1976.

/25/ Y. Taitel and A.E. Dukler, "Transient Gas-Liquid Flow in Horizontal Pipes: Modeling the Flow Pattern Transitions", AIChE Journal, Vol. 24, No. 5, Sept. 1978.

/26/ G.B. Wallis and J.E. Dobson, "The Onset of Slugging in Horizontal Stratified Air-Water Flow", Int. J. Multiphase Flow, Vol. 1, pp. 173-193, 1973

/27/ Wen-Hsiung Li, Sau-Hai Lam, "Principles of Fluid Mechanics", Addison-Wesely Publishing Company, 1964.

/28/ C. Smoglie, J. Reimann, "Two-Phase Flow Through a Small Horizontal Branch in a Pipe with Stratified Flow", Jahrestagung Kerntechnik '84, Frankfurt 22-24 Mai 1984.

/29/ J. Reimann, Not published data.

/30/ J. Weisbach, "Die Experimentalhydraulik", J.S. Engelhrdt, Freiburg 1855.

/31/ T.B. Drew, E.C. Koo and W.H. McAdams, "The Friction Factor in Smooth Wall Turbulent Flow", Trans., AIChE 28, 56 (1932).

/32/ V.L. Streeter, "Handbook of Fluid Dynamics", Chapter 3, McGraw-Hill Book Co. Inc., 1961.

/33/ VDI 2040, "Berechnungsgrundlagen für die Durchflußmessung von Drosselgeräten", VDI-Verlag, Düsseldorf, 1971.

/34/ F. D'Auria, P. Vigni, "Two Phase Critical Flow Models", CSNI Report No. 49, 1980.

/35/ F.J. Moody, "Maximum Flow Rate of a Single Component, Two-Phase Mixture", Transactions of the ASME, JHT, 1965, 87, pp. 134-142.

/36/ G.B. Wallis, "Critical Two Phase Flow", Int. J. Multiphase Flow, Vol. 6, pp. 97-112, 1980.

/37/ G.G. Weigand, S.L. Thompson, D. Tomasko, "Two Phase Jet Loads", NUREG/CR-2913, SAND 82-1935, R4, Jan. 1983.

/38/ K.R. Katsma et al., "User's Manual for RELAP4/MOD.5", INEL-Report, ANCR-NUREG-1335, Sept. 76.

/39/ V.H. Ransom, R.J. Wagner, J.A. Trapp, K.E. Carlson, D.M. Kiser, H.H. Kuo, H. Chow, R.A. Nelson, S.W. James, "RELAP5/MOD1 Code Manual Vol.1: System Models and Numerical Methods", NUREG/CR-1826 EGG-2070 DRAFT Revision 1, March 1981.

Appendix

A1 Method used to Calculate Propagated Errors

The error bars appearing in a number of results presented in this report, were determined by estimating the relative error of the measured parameters and the corresponding propagated error of the calculated variables.

The errors in the measured parameters mostly depend on the flow configuration and range of operation of the instruments, therefore the accuracy of the measurements was estimated for each typical experiment.

The relative error in the calculated variables was determined according to the theory of error propagation:

- The relative error δM of a magnitude M measured with an absolute error ΔM is:

$$\delta M = \frac{\Delta M}{M} \tag{1.1}$$

- The relative error of a function $F(M_i)$ of n variables M_i measured with absolute errors ΔM_i, is:

$$\delta F \equiv \frac{\Delta F}{F} = \frac{1}{F} \sum_{i=1}^{n} \frac{\partial F}{\partial M_i} \Delta M_i \tag{1.2}$$

Equations (1.1) and (1.2) were used with the following conditions:

- No error was asigned to D, d, A_1, A_3, g, ε, ρ_1, K, ζ, c_a, c_g, and c_1.
- The relative error in A_g and A_1 was determined considering the absolute error in h_g and h_1 respectively and using a table for areas of circular sectors.

This procedure gives the formulas listed below:

$$\rho_g = c_a \frac{P_1}{T_1}$$

$$\delta\rho_g = \delta P_1 + \delta T_1$$

$$\delta(\rho_1 - \rho_g) = \frac{\rho_g}{\rho_e - \rho_g} \delta\rho_g$$

$$W_{(1,2,3)g} = c_g(P_o \Delta P_o T_o)^{0.5}$$

$$\delta W_{(1,2,3)g} = 0.5\ (\delta P_o + \delta \Delta P_o + \delta T_o)$$

$$W_{11} = c_1\ (\rho_1 \Delta P_o)^{0.5}$$

$$\delta W_{11} = 0.5\ \delta \Delta P_o$$

$$W_{3g} = W_{1g} - W_{2g}$$

$$\delta W_{3g} = \frac{1}{W_{3g}}\ (W_{1g}\ \delta W_{1g} - W_{2g}\ \delta W_{2g})$$

W_{31} = weight of water/time

$$\delta W_{31} = \delta\ \text{weight} + \delta\ \text{time}$$

$$v_{1g} = \frac{W_{1g}}{\rho_g A_g}$$

$$\delta v_{1g} = \delta W_{1g} + \delta \rho_g + \delta A_g$$

$$h_b = [K(\zeta \varepsilon A_3)^{0.4}/g^{0.2}]\ (\Delta P_{1-34}/\rho_1 - \rho_g)^{0.2}$$

$$\delta h_b = 0.2\ [\ \delta \Delta P_{1-34} + \delta(\rho_1 - \rho_g)]$$

$$x_3 = \frac{1}{1+W_{31}/W_{3g}}$$

$$\delta x_3 = (1-x_3)(\delta W_{31} + \delta W_{3g})$$

$$G_3 = (W_{3g} + W_{31})/A_3$$

$$\delta G_3 = x_3\ \delta W_{3g} + (1-x_3)\ \delta W_{31}$$

$$G_{3b} = \zeta \varepsilon (\rho_b \Delta P_{1-34})^{0.5}$$

$$\delta G_{3b} = 0.5\ (\delta \rho_b + \delta \Delta P_{1-34})$$

The estimated errors in the measurements and their contribution to the propagated error in the results are illustrated below with two numerical examples.

Example 1: Beginning of gas entrainment in downward branches: strong vorticity.
Measured parameters:

$P_1 = (4.1 \pm 0.1)$ bar
$T_1 = (290 \pm 1.5)$ K
$h_b = (33 \pm 1.5)$ mm
weight of water = (54.5 ± 0.1) kg
time = (427 ± 3) sec

Plotted variables: $K_{ge} = h_b\ [g\rho_1(\rho_1-\rho_g)]^{0.2}/W_{31}{}^{0.4}$; h_b/d

Propagated errors:

$$\delta K_{ge} = \delta h_b + 0.2\ \delta(\rho_1-\rho_g) + 0.4\ \delta W_{31}$$

$$= \delta h_b + 0.2\ \frac{\rho_g}{\rho_l-\rho_g}\ (\delta P_1 + \delta T_1) + 0.4\ (\delta \text{weight} + \delta \text{time})$$

$$= \frac{1.5}{33} + 0.2\ \frac{4.9}{995.1}\ (\frac{0.1}{4.1} + \frac{1.5}{290}) + 0.4\ (\frac{0.1}{54.5} + \frac{3}{427})$$

$$\delta K_{ge} = 0.045 + 0.00003 + 0.0035 \simeq 4.9\ \%$$

$$\delta(h_b/d) = \delta h_b = 0.045 = 4.5\ \%$$

Similar results are obtained for the beginning of entrainment in other geometries. Therefore the relative error in K is practically given by the relative error in the liquid level.

Example 2: Liquid entrainment in upward branches: wavy interface.
Maximal δw_{31} due to water evaporation: 20 %
Measured parameters:

$P_{o1} = (14.3 \pm 0.1)$ bar
$T_{o1} = (289 \pm 1.5)$ K
$\Delta P_{o1} = (60 \pm 3)$ mmHg
$P_1 = (4.20 \pm 0.05)$bar
$T_1 = (289 \pm 1.5)$ °C
$\Delta P_{1-34} = (0.12 \pm 0.01)$ bar
$h = (61 \pm 2)$ mm

Plotted variables:

$$\frac{h}{h_b} = h/[K(\zeta\varepsilon A_3)^{0.4}/g^{0.2}](\Delta P_{1-34}/(\rho_1-\rho_g))^{0.2}$$

$$x_3 = 1/(1 + W_{31}/W_{3g}) \simeq 0.991$$

$$\frac{G_3}{G_{3b}} = (W_{3g} + W_{31})/A_3\zeta\varepsilon(\rho_b \Delta P_{1-34})^{0.5}$$

Propagated errors:

$$\delta\frac{h}{h_b} = \delta h + 0.2\ [\delta\Delta P_{1-34} + \delta(\rho_1 - \rho_g)]$$

$$= \delta h + 0.2\ [\delta\Delta P_{1-34} + \frac{\rho_g}{\rho_l-\rho_g}(\delta P_1 + \delta T_1)]$$

$$= \frac{2}{61} + 0.2\ [\frac{0.01}{0.12} + \frac{5.1}{994.9}(\frac{0.05}{4.20} + \frac{1.5}{289})]$$

$$\delta\frac{h}{h_b} = 0.0328 + 0.0168 \simeq 5\ \%$$

$$\delta x_3 = (1-x_3)(\delta W_{31} + \delta W_{3g})$$

$$= (1-0.991)[0.20 + 0.5\ (\delta P_{o1} + \delta\Delta P_{o1} + \delta T_{o1})]$$

$$= 0.009\ [0.20 + \frac{3}{350} + 0.5\ (\frac{0.1}{14.3} + \frac{2}{60} + \frac{1.5}{289})]$$

$$\delta x_3 = 0.002 = 0.2\ \%$$

$$\delta\frac{G_3}{G_{3b}} = x_3\,\delta W_{3g} + (1-x_3)\,\delta W_{31} + 0.5\ (\delta\rho_g + \delta\Delta P_{1-34})$$

$$= 0.991\text{x}0.5\ (\delta P_{o1} + \delta\Delta P_{o1} + \delta T_{o1}) + 0.009\text{x}0.2 + 0.5(\delta P_1 + \delta T_1 + \delta\Delta P_{1-34})$$

$$= 0.5\ (\frac{0.1}{14.3} + \frac{2}{60} + \frac{1.5}{289} + 0.009\text{x}0.2 + 0.5\ (\frac{0.05}{4.20} + \frac{1.5}{289} + \frac{0.01}{0.12}$$

$$\delta\frac{G_3}{G_{3b}} = 0.022 + 0.0018 + 0.05 \quad 7.4\ \%$$

From these results the following conclusions are valid for general entrainment processes:

- The relative error in h/h_b is dominated by the relativ error in h.
- The relative error in x_3 increases for decreasing qualities and, for upward branches, is dominated by the error in W_{31} due to liquid evaporation.
- The main contribution to the relative error in G_3/G_{3b} are the errors in ΔP_{1-34} and W_{3g} or W_{31} for high or low qualities, respectively.

A2 Theoretical Research on the Flow of Nonhomogeneous Fluids (A. Craya /12/)

Figure 2.1 defines the parameters used by Craya to determine the incipient liquid entrainment through a side orifice above the horizontal interface between two incompressible fluids of different densities.

Fig. 2.1

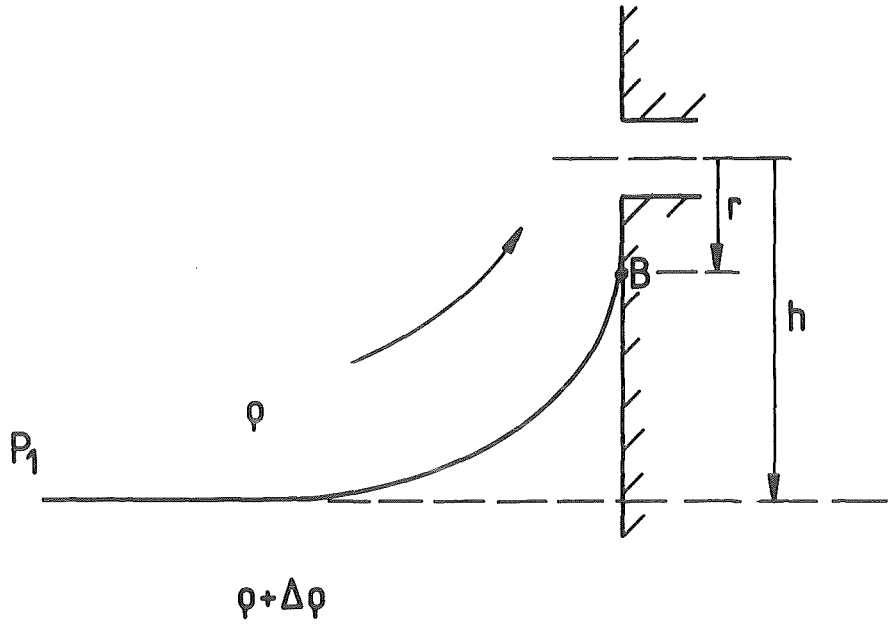

The heavier fluid, at rest, satisfies the hydrostatic condition:

$$P_B + g(\rho+\Delta\rho)(h-r) = P_1 \qquad (2.1)$$

where r is the distance from the orifice axis to the top B of the deflected interface. The lighter fluid, entering the orifice with phase velocity V, satisfies the Bernouilli equation:

$$P_B + 1/2\ \rho V^2 + g\rho(h-r) = P_1 \qquad (2.2)$$

From Eqs. (2.1) and (2.2) the condition of equilibrium at B is:

$$\frac{V^2}{2} = \frac{\Delta\rho}{\rho}\, g\ (h-r) \qquad (2.3)$$

If the velocity $\vec{V}$ verifies the condition for a two dimensional sink of strength q:

$$V = \frac{q}{\pi r} \qquad (2.4)$$

Eq. (2.3) becomes

$$\frac{V^2}{2} = \frac{\Delta\rho}{\rho} g \left(h-r\right) = \frac{q^2}{2\pi^2 r^2} \tag{2.5}$$

From this expression the term $V^2/2$ can be plotted as a function of r with two different curves: a straight line and a parabola, as shown in Fig. 2.2.

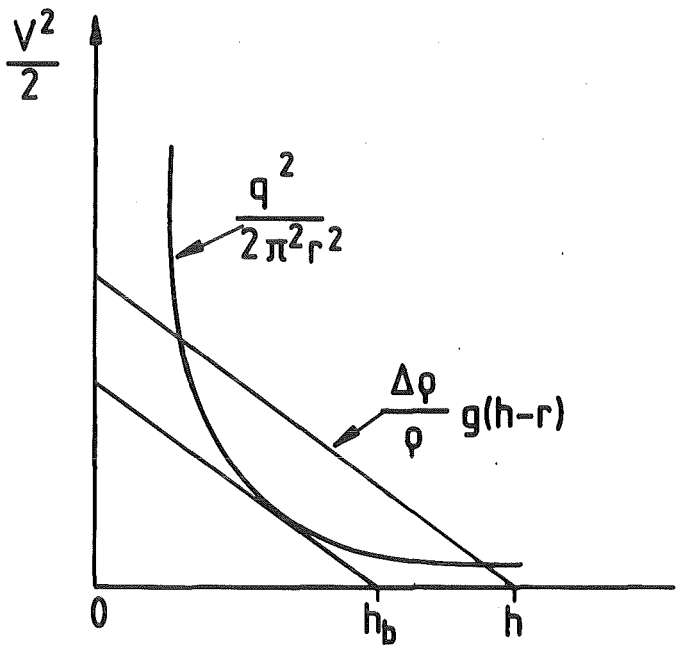

Fig. 2.2

The condition for the beginning of entrainment is obtained when Eq. (2.5) has a double root, i.e., for $r = 2h_b/3$ which, replaced in (2.5), gives:

$$\frac{\Delta\rho}{\rho} = g\left(h_b - \frac{2}{3}h_b\right) = q^2/2\pi^2\left(2h_b/3\right)^2 \tag{2.6}$$

or

$$\frac{\Delta\rho}{\rho_b} g \frac{h_b^3}{q^2} = 27/8\pi^2 \tag{2.7}$$

Craya extends this result to a three dimensional punctual sink just writing:

$$\frac{\Delta\rho}{\rho_b} g \frac{h_b^5}{q^2} = \text{constant} \tag{2.8}$$

and obtains finally the value 0.154 for the constant.

A3 The Homogeneous Equlibrium Model (HEM) (F.J. Moody /35/)

The theory known as HEM (Homogeneous Equilibrium Model) is the most simple equilibrium model that may be formulated in the analysis of two phase flow (compare D'Auria et al. /34/). It has been developed initially to analyze situations in which a fluid contained in a pressure vessel outflows through a pipe the diameter of which is much smaller than the vessel diameter.

The basic assumptions of the HEM are:

- Homogeneity: The mixture is considered as a single component fluid with channel averaged thermodynamical properties and both phases having the same velocity.
- Thermodynamical equilibrium: The pressure and temperature of liquid and vapor are equal and take values corresponding to the Mollier diagram saturation curve. However, changes of the quality are allowed along the flow path, which is in contrast with the thermodynamical hypothesis, because condensation and evaporation depend on differences of temperature and/or pressure through the phases. Implicitly, the changes in quality are supposed to take place at infinite velocity.
- Isentropic flow: Neither heat nor work is interchanged with the exterior.

For stationary flow, the balance equations are:

- continuity equation:

$$\rho_m \, V \, A = \text{const.} \tag{3.1}$$

- energy equation:

$$1/2 \, \rho_m \, V^2 + h = h_o \tag{3.2}$$

- state equations:

$$h = h_1 + x \, h_{1g} \tag{3.3}$$

$$v_m = v_1 + x \, v_{1g} \tag{3.4}$$

$$s = s_1 + x \, s_{1g} \tag{3.5}$$

- isentropic conditions:

$$ds = 0 \tag{3.6}$$

By combining the equations above the following expression is obtained for the mass flux:

$$G = \frac{2\left[h_o - h_\ell - \frac{s_o - s}{s_{\ell g}} \, h_{\ell g}\right]^{0.5}}{v_\ell + \frac{s_o - s_\ell}{s_{\ell g}} \, v_{\ell g}} \tag{3.7}$$

After giving the reservoir conditions the mass flux given by Eq. (3.7) depends only upon the thermodynamic state of the fluid. Consequently, the maximum mass flux (critical flow) must also depend only on the thermodynamic state of the fluid.

Choking is defined as the state in the fluid where changes in the downstream properties do not alter the mass flow rate or any properties upstream of the break. The critical mass flux G_{crit} occurs at the point where the flow reaches the sonic velocity:

$$V/c = 1 \tag{3.8}$$

To determine G_{crit} the downstream pressure is decreased until the mass flux reachs its maximal value.

A4 RELAP5 Model for Horizontal Branch Quality (from Ransom et al. /39/)

This model assumes stratified flow in a horizontal main pipe of diameter D (void fraction α_1) and choked flow in a horizontal branch of diameter d (void fraction α_3). To define α_3 as a function of α_1 the RELAP5 code uses the criterion for transition from stratified horizontal flow regime in a round pipe as given by Taitel and Dukler /24, 25/:

$$v_g > (1-h_1/D)\ [g\,(\rho_\ell-\rho_g)/\rho_g A'_\ell]^{0.5} \qquad (4.1)$$

where the symbols are those defined in Section 4.4. The right hand side of Eq. (4.1) is called the limit gas velocity v_{gL}.

The central angle $\Theta = \cos^{-1}(2h_1/D - 1)$, defined in Fig. 4.1

Fig. 4.1

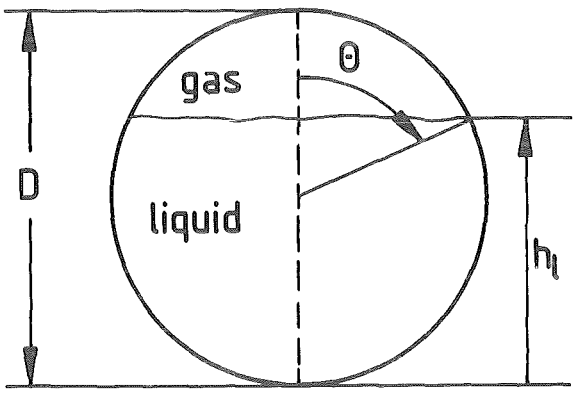

is used to rewrite h_1, A'_1 and α_1 as follows:

$$h_1 = D/2\ (1 + \cos\Theta) \qquad (4.2)$$

$$A'_1 = D \sin\Theta \qquad (4.3)$$

$$a_1 = (2\Theta - \sin 2\Theta)/2\pi \qquad (4.4)$$

where Θ is expressed in radians.

With $A_g = \alpha_1 \pi D^2/4$ and the expressions given by Eqs. (4.2), (4.3) and (4.4), the limit gas velocity (Eq. (4.1)) becomes:

$$v_{gL} = \frac{1}{4\sqrt{2}}\,(1-\cos\Theta)\left[D g\,\frac{\rho_\ell-\rho_g}{\rho_g}\,\frac{2\Theta-\sin 2\Theta}{\sin\Theta}\right]^{0.5} \qquad (4.5)$$

The RELAP5 code defines α_3 for the interface above and below the branch entrance, respectively, as follows:

$$\alpha_3 = \alpha_1 \left(v_{ig} / v_{gL} \right)^{0.5} \qquad \text{for } h_1 > (D+d)/2 \tag{4.6}$$

$$\alpha_3 = 1 - (1-\alpha_1) \left(v_{ig} / v_{gL} \right)^{0.5} \qquad \text{for } h_1 < (D-d)/2 \tag{4.7}$$

For liquid levels within the outlet area, i.e., for $(D-d)/2 < h_1 < (D+d)/2$, α_3 is obtained by interpolation of the two void fractions computed at the boundaries.

A5 TABLES OF EXPERIMENTAL DATA

Table 5.1: Transition from stratified to slug flow in the horizontal main pipe (upward branches)

d m	T_l K	P_l MPa	h_g m	W_{lg} kg/s	W_{3g} kg/s
0.012	298	0.490	0.031	0.056	0
	293		0.046	0.085	
			0.051		
	295		0.054	0.123	> 0
		0.390	0.053	0.107	
		0.490	0.051	0.122	
		0.410	0.046	0.100	
	289	0.430		0.090	0
	290	0.379	0.044		
		0.406	0.042		
		0.399	0.044		> 0
		0.345	0.042		
	281	0.474	0.046	0.112	0
		0.472		0.122	> 0
		0.288	0.041	0.052	0
		0.338	0.044	0.081	
0.020	285	0.395	0.072	0.174	> 0
		0.323			
		0.382		0.171	0
		0.309			> 0
		0.293		0.161	0

d m	T_l K	P_l MPa	h_g m	W_{lg} kg/s	W_{3g} kg/s
0.020	285	0.272	0.072	0.161	> 0
		0.250		0.143	0
		0.238			> 0
	288	0.500	0.076	0.278	0
		0.498	0.064	0.181	
		0.475			> 0
		0.408		0.154	
		0.482	0.063	0.166	
	290	0.358	0.046	0.091	
		0.341	0.044	0.082	0
		0.322			> 0
	282	0.423	0.048	0.115	0
		0.366	0.042	0.098	
		0.394	0.042		> 0
	291	0.373	0.060	0.140	0
		0.235	0.052	0.083	
		0.404	0.056	0.125	
		0.421	0.057	0.142	
		0.447	0.061	0.187	
		0.393	0.065	0.172	
		0.460	0.066	0.208	

Table 5.2: Beginning of gas entrainment in downward branches; $v_{2g} = 0$, $v_{21} = 0$.

d m	T_1 K	P_1 MPa	h_b m	W_{3b} kg/s
0.006	291	0.412	0.055	0.281
		0.417	0.060	0.367
		0.415	0.066	0.454
		0.414	0.068	0.473
		0.412	0.030	0.128
		0.419	0.040	0.182
			0.056	0.315
			0.060	0.381
		0.409	0.045	0.236
0.008	290	0.414	0.047	0.221
		0.412	0.041	0.280
		0.399	0.057	0.265
		0.399	0.061	0.519
	295	0.478	0.054	0.351
		0.381	0.040	0.202
		0.406	0.064	0.465
		0.370	0.073	0.632
		0.337	0.077	0.733
	294	0.474	0.045	0.257
		0.423	0.041	0.113
		0.433	0.046	0.283

d m	T_1 K	P_1 MPa	h_b m	W_{3b} kg/s
0.008	294	0.435	0.063	0.383
		0.441		0.444
		0.434		0.524
		0.433	0.074	0.697
		0.421	0.034	0.128
		0.433	0.025	0.073
		0.404	0.070	0.657
0.012	296	0.438	0.058	0.428
		0.420	0.070	0.623
		0.443	0.075	0.721
		0.463	0.080	0.975
		0.423	0.085	1.391
		0.482	0.083	1.020
		0.412	0.056	0.518
		0.439	0.048	0.261
		0.431	0.061	0.446
		0.438	0.070	0.631
	291	0.490	0.050	0.366
		0.414	0.046	0.288
			0.033	0.128

Table 5.3: Beginning of liquid entrainment in upward branches; $v_{2g} = 0$, $v_{21} = 0$

d m	T_1 K	P_1 MPa	h_b m	W_{3b} 10^{-3}kg/s
0.006	285	0.463	0.034	9.9
		0.448	0.041	13.2
		0.463	0.043	15.8
		0.462	0.049	19.7
		0.472	0.026	7.1
		0.461	0.030	8.15
		0.485	0.032	9.0
		0.484	0.038	11.7
		0.470	0.044	15.7
	286	0.343	0.030	6.8
		0.462	0.032	9.0
		0.507	0.035	10.0
		0.455	0.038	10.5
		0.343	0.042	11.3
		0.417	0.045	14.3
0.012	298	0.320	0.068	46.0
		0.340	0.061	55.7
	288	0.510	0.081	114.4
	293	0.380	0.083	85.2
	295	0.510	0.086	130.9
		0.380	0.074	71.1
		0.350	0.064	52.0
			0.054	33.9
	292	0.500	0.061	40.8
		0.490	0.057	33.1
			0.054	24.1
		0.470	0.052	19.0
		0.500	0.048	29.3
		0.480	0.045	23.8
		0.430	0.048	17.4
		0.370	0.037	11.7
		0.287	0.031	10.4
		0.490	0.079	109.2

d m	T_1 K	P_1 MPa	h_b m	W_{3b} 10^{-3}kg/s
0.012	292	0.520	0.081	118.9
		0.420		95.9
	290	0.208	0.054	40.6
		0.482	0.066	39.4
		0.434	0.076	87.0
		0.479		104.8
	291	0.385	0.072	92.7
		0.407	0.073	
		0.471	0.074	85.6
		0.390	0.062	92.7
		0.324		74.5
		0.508	0.066	59.8
		0.431		97.7
		0.219	0.046	48.2
		0.487	0.050	32.7
				43.0
		0.479	0.069	75.0
		9.345	0.072	73.5
		0.469	0.073	93.0
		0.478	0.079	109.6
0.020	288	0.490	0.064	181.0
		0.450		154.0
		0.350		128.0
		0.300		116.0
		0.250		97.0
		0.490	0.066	29.0
		0.430		62.0
		0.300		42.0
		0.490	0.067	105.0
	292	0.510	0.072	174.0
		0.380		171.0
		0.290		161.0
		0.250		143.0
		0.220		127.0

Table 5.3: (2nd page)

d m	T_1 K	P_1 MPa	h_b m	W_{3b} 10^{-3}kg/s
0.020	292	0.180	0.072	99
	288	0.350	0.073	82
		0.470		106
		0.490	0.076	242
		0.500		278
		0.390		106
		0.360		124
		0.410		167
	292	0.470	0.080	183
	288	0.490	0.086	278
	292	0.190	0.089	99
		0.210		120
		0.230		136
		0.260		150

d m	T_1 K	P_1 MPa	h_b m	W_{3b} 10^{-3}kg/s
0.020	288	0.470	0.095	297
				322
	293	0.466	0.060	38
		0.514	0.061	71
		0.507	0.068	86
	292	0.475		57
		0.388	0.071	81
		0.489	0.072	102
		0.516		100
		0.393		71
	293	0.504	0.075	118
	292	0.383	0.077	103
	293	0.485	0.079	154
		0.292		87

Table 5.4: Beginning of liquid entrainment in horizontal branches; $v_{2g} = 0$, $v_{21} = 0$.

d m	T_1 K	P_1 MPa	h_b m	W_{3b} 10^{-3}kg/s
0.006	287	0.477	0.008	3.8
		0.376	0.010	5.1
		0.421	0.012	8.8
		0.419	0.013	12.7
		0.364	0.015	16.0
		0.414	0.016	22.2
		0.443	0.014	15.1
		0.453	0.011	7.8
	289	0.261	0.013	5.3
		0.407	0.010	7.1
		0.464	0.009	6.6
		0.391	0.016	20.7
		0.335	0.014	17.0
	290	0.376	0.011	11.3
		0.361	0.016	19
		0.403	0.020	21.8
		0.288	0.014	11.9
		0.370	0.009	6.2
		0.343	0.013	13.2
0.012	281	0.441	0.022	41.5
		0.375	0.025	51.4
		0.410	0.030	77.7
	280	0.463	0.033	96.7
		0.465	0.030	81.1
		0.448	0.032	88.7
		0.472	0.034	104.8
		0.446	0.027	62.3
		0.468	0.028	71.9
		0.420	0.029	75.1
		0.470	0.033	103.4
	281	0.483	0.026	61.8
		0.423	0.029	70.0
		0.434	0.017	25.0
		0.470	0.018	27.5

d m	T_1 K	P_1 MPa	h_b m	W_{3b} kg/s
0.012	281	0.415	0.019	29.0
		0.431	0.020	34.0
		0.419	0.021	37.1
		0.420	0.022	42.3
		0.407	0.023	48.8
		0.423	0.022	44.3
	279	0.438	0.030	88.1
	281	0.463	0.025	60.0
		0.443	0.027	65.2
		0.454	0.027	64.9
		0.461	0.028	73.3
		0.437	0.031	88.2
		0.464	0.032	95.7
		0.455	0.033	104.2
		0.422	0.023	45.4
	283	0.367	0.019	27.3
	282	0.270	0.028	56.4
		0.276	0.026	48.1
		0.279	0.024	41.0
	283	0.352	0.020	32.9
		0.372	0.023	42.5
		0.335		42.9
		0.276	0.025	46.7
		0.354	0.023	43.1
		0.328	0.026	54.3
		0.320	0.030	57.8
		0.295	0.031	62.6
		0.293		66.9
		0.307		72.2
0.020	286	0.313	0.015	12.1
		0.235	0.016	12.5
		0.265	0.018	18.7
		0.213	0.020	24.2
		0.313	0.019	29.2

Table. 5.4: 2nd page

d m	T_1 K	P_1 MPa	h_b m	W_{3b} kg/s
0.020	286	0.294	0.023	38.3
		0.394		48.9
		0.365	0.024	50.9
		0.321	0.026	55.4
		0.317	0.029	69.1
		0.325	0.031	78.0
		0.255	0.034	77.1
	292	0.353		94.0
		0.402	0.038	119.2
		0.389	0.043	148.6
		0.402	0.051	203.5
	293	0.330	0.029	71.2
		0.336	0.026	55.0
	295	0.441	0.055	256.8
		0.419	0.052	235.0

d m	T_1 K	P_1 MPa	h_b m	W_{3b} 10^{-3}kg/s
0.020	293	0.317	0.027	60.3
		0.336	0.018	24.3
		0.394	0.027	58.2
		0.389	0.026	58.2
		0.420	0.027	69.5
		0.449	0.028	76.1
		0.449	0.028	76.1
	290	0.350	0.027	65.4
		0.350	0.027	66.1
		0.340	0.029	59.1
		0.357	0.027	
		0.385	0.024	42.3
		0.365	0.024	41.8
	295	0.374	0.026	46.7

Table 5.5: Beginning of gas entrainment in horizontal branches; $v_{2g} = 0$, $v_{21} = 0$

d m	T_1 K	P_1 MPa	h_b m	W_{3b} kg/s
0.006	288	0.423	0.020	0.352
		0.365	0.023	0.407
		0.333	0.022	0.366
		0.480	0.025	0.481
		0.394	0.021	0.424
		0.406		0.340
		0.411	0.020	0.295
	292	0.304	0.021	0.406
		0.307		0.344
		0.365	0.023	0.451
		0.298	0.021	0.348
		0.252	0.019	0.255
		0.358	0.020	0.299
		0.420	0.019	0.271
		0.395	0.017	0.194
		0.285	0.021	0.381
		0.318	0.022	0.402
	293	0.423	0.017	0.183
		0.298	0.016	0.247
		0.340	0.019	0.310
		0.449	0.017	0.188
	294	0.365	0.013	0.121
		0.482	0.018	0.330
		0.382	0.020	
	289	0.482	0.013	0.126
	290	0.443	0.018	0.225
0.012	281	0.433	0.022	0.483
	282	0.414		0.794
		0.438	0.024	0.624
		0.408	0.025	0.698
	285	0.315	0.021	0.414
		0.316		0.369

d m	T_1 K	P_1 MPa	h_b m	W_{3b} kg/s
0.012	285	0.294	0.023	0.618
		0.316		0.594
		0.309	0.020	0.415
		0.274		0.472
	288	0.409	0.025	0.603
		0.406	0.028	0.797
	296	0.358	0.024	0.568
		0.360	0.026	0.713
		0.363	0.031	1.064
		0.360	0.032	1.275
		0.370	0.036	1.843
	283	0.317	0.019	0.349
		0.316	0.021	0.457
		0.315	0.024	0.640
		0.384	0.025	0.816
		0.385	0.028	1.027
		0.383	0.029	1.252
	287	0.374	0.031	0.913
		0.375	0.035	1.288
		0.394	0.036	1.526
		0.356	0.033	1.026
0.020	286	0.418	0.016	0.166
		0.405	0.022	0.501
		0.465		0.560
		0.422		0.425
		0.327	0.021	0.398
		0.306	0.026	0.716
		0.327		0.701
		0.419	0.025	0.622
		0.477	0.026	0.633
	292	0.376	0.019	0.266
		0.412	0.020	0.373

Table 5.5: (2nd page)

d m	T_1 K	P_1 MPa	h_b m	W_{3b} kg/s
		0.311	0.022	0.571
		0.325	0.026	0.635
0.020	294	0.306	0.024	0.472
	296	0.384	0.033	1.396
		0.394	0.034	1.779
		0.404	0.051	3.809
	293	0.338	0.026	0.699
		0.453	0.028	0.661
	292	0.318	0.029	0.836
		0.314	0.023	0.639

d m	T_1 K	P_1 MPa	h_b m	W_{3b} kg/s
		0.368	0.022	0.489
		0.309	0.030	1.063
0.020	292	0.387	0.024	0.479
		0.394	0.022	0.496
		0.414	0.023	0.539
		0.407	0.025	0.545
		0.406	0.023	0.475
		0.404	0.026	0.711
	290	0.386	0.030	0.811
	294	0.445	0.022	0.463

Table 5.6: Beginning of liquid entrainment in upward branches; $v_{2g} > 0$, $v_{21} = 0$

d m	T_1 K	P_1 MPa	h_b m	W_{3b} 10^{-3}	W_{2g} kg/s
0.012	295	0.410	0.054	88.7	11.6
		0.481		100.8	22.0
		0.440		83.5	17.7
				81.8	14.1
		0.412		69.4	15.7
		0.395		56.6	12.1
		0.368		38.9	13.6
	289	0.452	0.049	90.3	11.7
	290	0.470	0.056	48.0	3.2
	291	0.482	0.058	75.1	11.6
		0.346		53.4	6.4
		0.412	0.066	89.2	8.5
		0.213	0.046	43.8	4.5
		0.438	0.054	73.0	11.6
	286	0.458	0.068		20.6
		0.463	0.044	26.1	21.5

d m	T_1 K	P_1 MPa	h_b m	W_{3b} 10^{-3}	W_{2g} kg/s
0.012	280	0.298	0.044	36.2	21.6
		0.405	0.046	38.6	18.1
		0.460		39.8	15.7
		0.288		35.8	19.6
		0.386	0.047	60.7	30.8
		0.363		59.3	32.1
		0.353	0.046	58.3	33.2
		0.385		66.7	
		0.415	0.048	73.0	35.8
		0.394	0.061	70.6	36.3
		0.353		58.9	35.7
		0.403	0.051	70.4	36.3
	281	0.340		60.9	27.0
		0.320	0.057	48.7	25.4
0.020	279	0.404	0.049	102.2	17.7
		0.394	0.060	94.4	37.2

Table 5.7: Beginning of liquid entrainment in upward branches; $v_{2g} = 0$, $v_{21} > 0$

d m	T_1 K	P_1 MPa	h_b m	W_{3b} 10^{-3}kg/s	W_{21} kg/s
0.012	281	0.372	0.071	92.0	2.12
			0.073		
		0.459	0.071		2.06
		0.451	0.076		
		0.401	0.070	77.8	
			0.081		
			0.071		2.08
		0.396	0.073		
		0.364		69.6	0.75

d m	T_1 K	P_1 MPa	h_b m	W_{3b} 10^{-3}kg/s	W_{21} kg/s
0.020	280	0.327	0.078	85.0	2.07
			0.076		
		0.410	0.079	131.0	2.16
		0.412		108.8	2.15
	279	0.347	0.072	84.1	0.88
		0.404	0.049	102.2	2.05
		0.424	0.074	114.9	1.99
		0.366	0.073	98.1	2.05
		0.394	0.060	94.4	2.07

Table 5.8: Beginning of liquid entrainment in horizontal branches, $v_{2g} > 0$; $v_{21} = 0$

d m	T_1 K	P_1 MPa	h_b m	W_{3b} 10^{-3} kg/s	W_2 kg/s
0.012	282	0.263	0.022	31.1	39.9
	285	0.313	0.014	12.4	23.3
		0.333	0.017	17.5	25.3
		0.324		16.7	31.0
		0.365	0.018	19.7	35.5
		0.370		22.4	43.8
		0.344	0.019	24.4	43.5
		0.322	0.021	28.6	46.2
		0.304	0.022	32.2	43.6
		0.272	0.023	32.0	39.1
	296	0.353	0.031	52.6	118.0
		0.468	0.022	18.7	137.0
		0.413	0.012	13.7	142.0
		0.441	0.023	17.1	152.0
		0.472	0.024	20.0	171.0
		0.389	0.019	10.0	140.0
	297	0.428	0.033	58.2	87.9
		0.463	0.024	18.8	189.0
		0.363	0.023	14.6	144.0
		0.383		13.6	156.0
		0.306	0.026	25.2	69.4
		0.417	0.030	43.8	103.8

d m	T_1 K	P_1 MPa	h_b m	W_{3b} 10^{-3} kg/s	W_2 kg/s
0.012	297	0.338	0.029	57.4	86.5
		0.418	0.024	34.4	105.3
		0.380		34.0	115.5
		0.379	0.016	15.3	106.7
		0.315	0.015	12.3	89.2
		0.304	0.016	12.4	71.9
	298	0.412	0.028	69.2	100
0.020	293	0.317	0.027	60.3	23.4
		0.305	0.024	31.4	47.6
		0.389	0.019	18.5	61.1
		0.336	0.018	24.3	52.7
		0.296	0.026	41.9	36.1
	294	0.314	0.041	95.4	66.9
		0.390	0.036	67.7	84.6
		0.430	0.032	41.0	107.8
		0.424	0.027	25.7	112.7
		0.463	0.024	17.3	132.7
		0.443	0.019	13.1	145.2
	295	0.453		15.0	173.1
		0.397	0.027	23.0	151.1
		0.389		25.0	149.0
		0.355	0.030	27.4	118.6

Table 5.9: Beginning of liquid entrainment in horizontal branches, $v_{2g} = 0$, $v_{21} > 0$

d m	T_1 K	P_1 MPa	h_b m	W_{3b} 10^{-3}kg/s	W_{21}
0.012	283	0.303	0.017	17.9	0.663
		0.367	0.019	27.3	0.814
	285	0.352	0.021	32.9	1.147
		0.372	0.023	42.5	1.118
		0.320	0.030	57.8	1.665
		0.295	0.031	62.6	1.825
		0.293		66.9	1.890
	295	0.396	0.026	47.1	5.00
		0.445		46.4	5.38
		0.345		33.5	6.33
	296	0.389	0.019	25.2	5.91
		0.419	0.021	23.3	6.37
		0.433	0.019	19.6	6.29
		0.394	0.024	25.5	6.75
		0.330	0.021	28.1	7.35
		0.335		28.2	7.80
			0.023	24.3	8.17
		0.306	0.024	36.1	8.44
	297	0.485	0.028	59.5	3.30
0.020	293	0.345	0.027	42.8	3.08
		0.394		58.2	2.92

d m	T_1 K	P_1 MPa	h_b m	W_{3b} 10^{-3}kg/s	W_{21} kg/s
0.020	293	0.420	0.027	69.5	2.85
		0.449	0.028	76.1	2.72
					2.46
	294	0.409	0.037	75.0	3.18
		0.433	0.035	87.8	3.07
		0.443	0.033	64.9	2.98
		0.442	0.042	110.9	3.24
	290	0.350	0.027	65.4	1.86
				66.1	
		0.340	0.029	59.1	2.44
		0.357	0.027		2.29
		0.385	0.024	42.3	2.61
		0.365		41.8	3.18
		0.467	0.028		4.31
		0.350	0.026		4.90
	295	0.414		46.2	7.31
		0.374		46.7	6.75
		0.406	0.029	35.9	6.45
	294	0.338	0.030	47.6	7.96
		0.365	0.028		8.72
		0.459	0.026	26.7	9.08

Table 5.10: Beginning of gas entrainment in horizontal branches; $v_{2g} > 0$, $v_{2l} = 0$

d m	T_l K	P_l MPa	h_b m	W_{3b} kg/s	W_{2g} 10^{-3}kg/s
0.012	289	0.402	0.025	0.467	79.8
		0.404	0.023	0.337	79.9
		0.385	0.025	0.413	76.8
		0.373	0.026	0.444	71.1
		0.318	0.023	0.408	60.6
		0.289	0.022	0.287	54.0
		0.384		0.338	75.0
		0.235		0.350	63.1
	296	0.335	0.021	0.403	89.6
		0.368	0.016	0.222	99.3
		0.466		0.223	108
0.020	292	0.367	0.018	0.249	39.2

d m	T_l K	P_l MPa	h_b m	W_{3b} kg/s	W_{2g} 10^{-3}kg/s
0.020	292	0.407	0.019	0.296	49.8
		0.372		0.301	48.9
		0.387	0.022	0.382	58.2
			0.024	0.479	64.7
		0.394	0.022	0.496	69.8
		0.414	0.023	0.539	72.6
		0.407	0.025	0.545	76.7
		0.406	0.023	0.475	76.3
		0.404	0.026	0.711	
	294	0.463	0.023	0.439	91.0
		0.445	0.022	0463	88.7

Table 5.11: Beginning of gas entrainment in horizontal branches; $v_{2g} = 0$, $v_{21} > 0$

d m	T_1 K	P_1 MPa	h_b m	W_{3b} kg/s	W_{21} kg/s
0.012	287	0.281	0.032	0.742	2.80
		0.384	0.036	1.050	3.02
		0.385	0.035	1.222	3.11
		0.347	0.026	0.415	4.59
	295	0.288	0.032	0.858	4.77
		0.288	0.031	0.800	7.46
		0.365	0.020	0.205	7.00
		0.377		0.194	5.63
		0.355	0.018	0.180	8.52
		0.365	0.019	0.200	7.51
		0.355	0.026	0.493	9.50
		0.394	0.025	0.232	10.92
0.020	293	0.343	0.019	0.240	2.54

d m	T_1 K	P_1 MPa	h_b m	W_{3b} kg/s	W_{21} kg/s
0.020	297	0.343	0.023	0.431	2.64
		0.338	0.026	0.699	2.69
			0.028	0.661	3.87
	292	0.318	0.029	0.836	2.95
		0.314	0.023	0.639	3.49
		0.318	0.026	0.408	4.18
		0.320	0.025	0.394	4.99
	290	0.386	0.030	0.811	3.94
		0.382	0.029	0.625	3.91
		0.387	0.025	0.408	3.69
		0.372	0.034	0.786	5.50
		0.374	0.029	0.527	6.51

Table 5.12: Gas entrainment in downward branches.

d m	T_1 K	P_1 MPa	ΔP_{1-34} MPa	h m	W_{3g} 10^{-3}kg/s	W_{31} kg/s
0.006	287	0.364	0.225	0.017	6.00	0.175
		0.384	0.240	0.020	5.83	0.210
		0.546	0.340	0.016	6.36	0.203
		0.467	0.250	0.015	7.20	0.145
		0.517	0.310	0.017	5.71	0.201
		0.445	0.260	0.014	6.31	0.157
		0.520	0.145	0.018	5.76	0.144
0.008	295	0.482	0.199	0.039	4.66	0.434
		0.492	0.122	0.020	5.98	0.284
		0.521	0.119	0.017	8.66	0.262
		0.531	0.066	0.026	4.06	0.260
		0.480	0.200	0.023	8.87	0.348
		0.536	0.135	0.020	6.33	0.222
		0.460	0.190	0.023	5.28	0.398
	294	0.463	0.255	0.045	3.64	0.534
		0.541	0.250	0.038	6.56	0.474
		0.482	0.060	0.021	6.33	0.195

d m	T_1 K	P_1 MPa	ΔP_{1-34} MPa	h m	W_{3g} 10^{-3}kg/s	W_{31} kg/s
0.008	294	0.521	0.122	0.017	6.81	0.225
		0.493	0.220	0.022	7.05	0.326
		0.482	0.235	0.040	5.21	0.491
0.012	296		0.024	0.030	5.63	0.333
		0.443	0.120	0.052	6.34	0.854
		0.502	0.130	0.055	6.04	0.970
	291	0.287	0.125	0.026	9.48	0.592
		0.322	0.135	0.030	9.32	0.693
		0.370	0.165	0.041	9.04	0.855
		0.389	0.175	0.033	11.38	0.806
		0.365	0.150	0.051	6.80	0.877
		0.394	0.165	0.057	6.57	0.966
		0.417	0.175	0.048	9.09	0.906
		0.443	0.190	0.054	8.78	1.00
		0.456	0.180	0.016	8.69	1.90
		0.472	0.035	0.023	8.42	0.349

Table 5.13: Liquid entrainment in upward branches

d m	T_1 K	P_1 MPa	ΔP_{1-34} MPa	h m	W_{3g} 10^{-3}kg/s	W_{31} 10^{-3}kg/s
0.012	290	0.403	0.130	0.064	78.8	0.53
		0.422	0.038	0.049	51.2	0.51
		0.433	0.060	0.056	62.3	0.52
		0.435	0.070	0.062	74.5	0.20
		0.462	0.113		92.7	1.10
		0.367	0.172	0.055	85.7	1.45
		0.435	0.160	0.066	97.7	0.95
		0.315	0.124	0.046	71.6	0.39
		0.360	0.169	0.048	84.6	0.81
		0.376	0.138	0.054		1.65
	289	0.302	0.059	0.048	48.3	0.18
		0.477	0.032			0.41
	285	0.453	0.133	0.069	91.3	0.38
		0.418	0.196	0.073	93.1	0.03
		0.432	0.088	0.043	73.6	2.68
	280	0.463	0.128	0.059	94.4	0.97
		0.379	0.178	0.044	86.4	1.16
		0.397	0.137	0.043	86.1	0.88
		0.416	0.195	0.053	96.1	1.75
		0.404	0.154	0.055	89.1	1.32
		0.333	0.119	0.042	71.0	1.18
		0.406	0.152		89.4	1.41
		0.376	0.140		82.8	2.36
		0.423	0.199	0.036	67.6	1.84
		0.394	0.185	0.032	46.2	3.52
		0.294	0.131	0.041	63.8	3.40
		0.399	0.187	0.044	93.4	3.08
		0.414	0.195	0.046	95.0	1.30
		0.345		0.042	67.1	3.91
		0.364	0.171	0.073	85.6	0.08
		0.340	0.160	0.042	76.3	1.54
		0.308	0.146	0.041	68.4	3.60
0.012	281	0.474	0.194	0.046	112.2	1.37
		0.472	0.222		114.5	1.05
		0.458	0.215	0.049	110.1	0.91
		0.512	0.240	0.054	122.5	2.02
		0.463	0.218	0.056	112.1	0.44
		0.487	0.228	0.061	117.1	0.54
		0.228	0.096	0.041	51.6	0.95
		0.338	0.159	0.044	80.8	2.13
		0.469	0.220	0.046	112.2	1.98
0.020	292	0.482	0.024	0.071	122.6	0.89
		0.492	0.015	0.072	99.3	0.38
		0.335	0.012	0.070	71.2	0.17
	293	0.433	0.007	0.060	70.7	0.14
		0.413	0.011	0.061	85.6	0.73
		0.492	0.009	0.062		0.56
		0.340	0.014	0.069		0.47
		0.440	0.020	0.075	117.9	0.07
	280	0.481	0.052	0.076	206.9	0.51
		0.511	0.064	0.077	234.4	0.38
		0.343	0.015	0.047	83.1	1.50
		0.235	0.024	0.052		1.20
		0.404	0.028	0.056	125.4	1.38
		0.470	0.024	0.057		2.07
		0.447	0.044	0.061	186.7	1.14
		0.393		0.065	171.8	0.58
		0.461	0.056	0.066	207.8	1.27
		0.374	0.039	0.072	159.4	0.60
	282	0.451	0.018	0.049	102.7	2.98
		0.461	0.023	0.052	119.2	2.21
			0.026	0.057	126.9	1.50
		0.375	0.028	0.056	118.7	2.16

Table 5.14: Gas entrainment in horizontal branches

d m	T_1 K	P_1 MPa	ΔP_{1-34} MPa	h m	W_{3g} 10^{-3}kg/s	W_{31} kg/s
0.006	288	0.456	0.273	0.013	4.68	0.255
		0.443	0.076	0.005	4.85	0.092
		0.460	0.145	0.004	8.24	0.128
		0.470	0.244	0.007	8.07	0.180
		0.458	0.208	0.009	6.37	0.184
		0.413	0.226	0.007	6.90	0.166
	290	0.481	0.070	0.003	6.30	0.074
		0.466	0.127	0.006	6.50	0.130
		0.444	0.250	0.004	10.2	0.136
		0.430	0.184	0.000	10.5	0.10
		0.432	0.177	0.002	10.4	0.104
		0.485	0.155	0.012	4.15	0.211
		0.463	0.182	0.011	4.35	
		0.475	0.270	0.010	6.30	0.225
	292	0.412	0.213	0.011	4.22	0.215
		0.477	0.248	0.015	3.57	0.282
		0.439	0.143	0.014	2.11	0.229
		0.453	0.110			0.191
		0.460	0.077	0.009	3.23	0.136
	293	0.482	0.200	0.012	3.19	0.246
	294	0.372	0.091	0.006	3.51	0.111
	290	0.412	0.070		3.06	0.095
0.012	282	0.428	0.037	0.000	17.5	0.265
		0.433	0.050	0.003		0.301
		0.454	0.055	0.005		0.265
		0.465	0.067	0.010	13.1	0.486
		0.470	0.081	0.012		0.590
	280	0.379	0.035	0.006	14.5	0.312
		0.435	0.025	0.007	13.3	0.238
		0.470	0.020	0.008	12.4	0.250
		0.376	0.065	0.014	11.3	0.542

d m	T_1 K	P_1 MPa	ΔP_{1-34} MPa	h m	W_{3g} 10^{-3}kg/s	W_{31} kg/s
0.012	280	0.437	0.050	0.015	10.4	0.482
		0.476	0.033	0.017	9.57	0.442
		0.417	0.035	0.019	5.81	0.488
		0.475	0.030		7.80	0.430
	288	0.480	0.138	0.003	36.9	0.486
		0.422	0.157	0.000	42.7	0.405
	289	0.404	0.170	0.010	23.0	0.690
		0.423	0.195	0.014		0.821
		0.443	0.250	0.015		0.917
	296	0.455	0.205	0.004	26.0	0.635
0.020	286	0.464	0.001	0.003	5.85	0.082
		0.483	0.004	0.010	9.55	0.384
		0.441	0.003	0.013	6.87	0.408
	287	0.445	0.008	0.006	17.6	0.345
	292	0.426	0.018	0.011	19.1	0.692
		0.474	0.023	0.013	18.8	0.808
		0.442	0.032	0.016	19.1	0.969
		0.467	0.045	0.022	18.7	1.40
	296	0.291	0.056	0.002	35.7	0.675
		0.322	0.066	0.001	48.9	0.728
		0.369	0.097	0.007	54.4	1.23
		0.374	0.102	0.013	45.3	1.46
		0.367	0.109	0.016	39.1	1.57
		0.375	0.060	0.017	25.0	1.36
			0.414		0.020	1.01
		0.406	0.070	0.023	19.7	1.63
		0.382	0.120	0.028		2.34
	288	0.382	0.008	0.004		0.359
		0.318	0.011	0.003	22.4	0.388
		0.438	0.026	0.000	41.3	0.519

Table 5.15: Liquid entrainment in horizontal branches

d m	T_1 K	P_1 MPa	ΔP_{1-34} MPa	h m	W_{3g} 10^{-3}kg/s	W_{31} kg/s
0.006	288	0.298	0.066	0.004	7.08	0.028
		0.416	0.171	0.001	11.1	0.085
	290	0.403	0.088	0.002	9.12	0.049
		0.369	0.084	0.001	7.99	0.051
		0.383	0.102	0.003	9.36	0.052
		0.360	0.095	0.006	11.3	0.020
		0.370	0.143	0.009	14.6	0.017
		0.372	0.193	0.010	16.3	0.016
		0.443	0.230	0.004	15.1	0.069
		0.429	0.152	0.007	15.4	0.032
		0.439	0.161	0.010	18.9	0.010
	293	0.431	0.221	0.008	17.6	0.032
		0.433	0.164	0.007	16.1	0.033
	294	0.344		0.001	8.56	0.087
	289	0.379	0.115		7.75	0.078
	297	0.482	0.150	0.004	11.9	0.068
		0.480	0.202	0.006	14.9	0.063
		0.482	0.115	0.009	15.0	0.019
		0.260	0.110	0.005	7.75	0.040
	288	0.451	0.124	0.001	10.5	0.074
	290	0.430	0.184	0.000		0.105
	287	0.190	0.094	0.001	4.33	0.056
		0.180	0.090	0.004	4.40	0.054
		0.298	0.180	0.008	10.6	0.042
		0.374	0.220	0.009	14.6	0.032
		0.448	0.114		13.8	0.023
		0.487	0.093		13.7	0.018
		0.541	0.072	0.010	12.4	0.012
		0.171	0.089	0.006	5.58	0.025
		0.147	0.068	0.005	4.25	0.024
		0.203	0.117	0.008	7.60	0.021
		0.230	0.084		7.49	0.020
		0.284	0.147	0.010	12.3	0.016
	288	0.428	0.170	0.002	10.7	0.082

d m	T_1 K	P_1 MPa	ΔP_{1-34} MPa	h m	W_{3g} 10^{-3}kg/s	W_{31} kg/s
0.006	288	0.423	0.125	0.005	10.8	0.054
		0.419	0.096	0.007		0.029
		0.400	0.06	0.005	7.16	
		0.473	0.069	0.001	6.52	0.055
		0.286	0.172	0.002	7.76	0.077
		0.218	0.123		5.70	0.062
	295	0.476	0.132	0.001	9.16	0.092
	297	0.346	0.199		8.52	0.102
0.012	279	0.336	0.121	0.028	95.2	0.003
		0.384	0.188	0.030	115.0	0.002
		0.435	0.041	0.010	64.6	0.109
		0.416	0.243	0.019	67.8	0.151
		0.438	0.254		69.1	0.140
		0.486	0.120		68.2	0.121
		0.424	0.100	0.016	53.6	0.160
		0.477	0.051	0.014	45.5	0.139
		0.472	0.036	0.013	40.1	0.124
	282	0.372	0.052	0.020	49.0	0.035
		0.443	0.071	0.017	54.1	0.116
		0.428	0.094	0.018	59.2	0.109
		0.409	0.047	0.009	36.5	0.174
		0.426	0.045	0.016	46.1	0.077
		0.451	0.050	0.014	45.6	0.119
		0.436	0.045	0.011	38.8	0.157
		0.443	0.050	0.008	30.9	0.184
		0.409	0.069	0.016	50.8	0.096
	283	0.451	0.043	0.007	28.9	0.175
		0.438	0.030	0.005	23.4	0.173
		0.443	0.022	0.013	28.1	0.048
			0.029	0.011	28.6	0.090
		0.441	0.043	0.012	37.6	0.078
		0.451	0.039	0.018	41.5	0.024
		0.429	0.046	0.009	29.9	0.166
	282	0.428	0.019	0.004	17.1	0.155

Table 5.15: (2nd page)

d m	T_1 K	P_1 MPa	ΔP_{1-34} MPa	h m	W_{3g} 10^{-3}kg/s	W_{31} kg/s
0.012	282	0.434	0.019	0.002	15.0	0.167
		0.345	0.030	0.001	15.4	0.230
		0.428	0.037	0.000	17.5	0.265
	296	0.470	0.187	0.001	36.2	0.477
	295	0.492	0.079		28.6	0.305
		0.441	0.094		29.5	0.335
		0.410	0.153		35.15	0.432
		0.379	0.185		35.4	0.450
		0.323	0.113		26.4	0.359
		0.242	0.103		19.3	0.335
	289	0.218	0.018		9.58	0.149
		0.254	0.021	0.002	11.7	0.144
		0.141	0.014	0.004	7.07	0.087
		0.422	0.006		9.60	0.063
		0.546	0.007		12.8	0.073
		0.402	0.004	0.002	7.29	0.067
		0.487	0.005	0.006	11.1	0.040
		0.157	0.037	0.012	17.5	0.067
		0.159	0.054	0.014	19.6	0.043
		0.495	0.006	0.012	16.6	0.012
		0.172	0.008	0.014	17.9	0.006
		0.296	0.014		18.7	0.015
	288	0.422	0.157	0.000	42.7	0.405
0.020	287	0.441	0.007	0.010	36.5	0.145
		0.475	0.007	0.007	35.4	0.197
		0.480		0.001	26.6	0.292
		0.462	0.008	0.004	31.7	0.267
		0.492		0.015	45.4	0.102

d m	T_1 K	P_1 MPa	ΔP_{1-34} MPa	h m	W_{3g} 10^{-3}kg/s	W_{31} kg/s
0.020	292	0.323	0.050	0.023	94.0	0.164
		0.384	0.030	0.001	40.5	0.459
		0.462	0.017		39.6	0.44
	295	0.435	0.060	0.025	115.4	0.135
		0.477	0.065	0.011	81.22	0.498
		0.463	0.040	0.021	88.0	0.195
		0.384	0.070	0.017	89.1	0.358
		0.482	0.013	0.006	41.03	0.283
		0.419	0.028	0.010	62.5	0.324
		0.342	0.045	0.012	73.8	0.368
		0.325		0.018	79.9	0.239
		0.311	0.040	0.024	86.2	0.089
		0.387	0.010	0.004	28.1	0.307
		0.412	0.016	0.001	34.7	0.401
	288	0.308	0.010		23.5	0.255
		0.412	0.005		22.9	0.219
		0.451	0.004	0.003	22.5	0.166
	289	0.305	0.006	0.006	37.3	0.305
		0.327	0.029		48.9	0.397
		0.402	0.022	0.005	48.6	0.362
		0.462	0.028	0.001	48.0	0.505
		0.334	0.050	0.016	76.7	0.226
		0.463	0.026	0.015	74.8	0.188
		0.335	0.045	0.011	74.0	0.381
		0.304	0.065	0.014	81.1	0.393
		0.353	0.070	0.009	83.5	0.589
		0.409	0.090	0.001	83.3	0.877
	288	0.438	0.026	0.000	41.3	0.519